Karlsruhe Institute of Technology

Systematic studies of RF phase modulation at KARA

Master's Thesis of

Sebastian Maier

At the Department of Physics
Laboratory for Applications of Synchrotron Radiation

Reviewer:	Prof. Dr. Anke-Susanne Müller
Second reviewer:	Prof. Dr. Guido Drexlin
Advisor:	Dr. Akira Mochihashi

February 27, 2020

I declare that I have developed and written the enclosed thesis completely by myself, and have not used sources or means without declaration in the text.

KARLSRUHE, February 27, 2020

.....
(Sebastian Maier)

Accepted as master's thesis:

.....

Abstract

At the KIT storage ring KARA (KArlsruhe Research Accelerator), the beam lifetime is limited by scattering with rest gas atoms, but also affected by intra-beam Touschek scattering, which depends directly on the particle density. It has been reported in previous work, that a bunch lengthening can be achieved by a modulation of the RF acceleration voltages' phase, which causes an excitation of longitudinal oscillation modes within the stored bunches. For this thesis, a first systematic study of phase modulation (PM) close to the second harmonic of the synchrotron oscillation frequency with peak-to-peak amplitudes between 10 % and 20 % of the synchronous phase has been done, to find the optimum condition for the introduction of the phase modulation (*PM*) scheme into the acceleration operation. Thereby it has been focused explicitly on the affect of the PM on the bunch shape, the bunch length and consequently the total beam lifetime.

Kurzfassung

Die Lebensdauer des Elektronenstrahl am Karlsruhe Research Accelerator (*KARA*) Speichering, Karlsruhe Institute of Technology (*KIT*) ist hauptsächlich durch die Streuung an Restgasatomen limitiert, wobei auch die Touschek-Streuung zwischen zwei Elektronen des selben Elektronenpakets die Lebensdauer beschränkt. Dieser Effekt hängt direkt von der Elektronendichte ab. In früheren Arbeiten ist bereits herausgefunden worden, dass eine Verlängerung der Elektronenpakete durch eine Modulation der RF Beschleunigungsphase erreicht werden kann, wobei longitudinale Oszillationsmoden innerhalb der Pakete angeregt werden. Um die optimalen Bedingungen zur Einführung der Phasenmodulation (PM) in den Beschleuniger-Betrieb zu finden, ist in dieser Arbeit ist eine erste systematische Untersuchung der (PM) in der Nähe der zweiten Harmonischen der Synchrotronoszillationsfrequenz mit einer Amplitude von 10 % bis 20 % der synchronen Phase durchgeführt worden. Dabei ist ein besonderer Fokus auf dem Einfluss der Phasenmodulation auf die Paketform, die Paketlänge und folglich die Lebensdauer gelegt worden.

Contents

1. Introduction

In the experimental physics particle accelerators are in use since the 1920s with the goal of ever greater energies. At the start electrostatic fields were used to accelerated particles such as in Cockcroft-Walton [1] and Van-de-Graaff [2] accelerators, which are limited by the breakdown voltage. To reach a higher particle energy, a linear accelerator, which is based on high frequency oscillating fields was invented by G. Ising [3] and turned into practice by R. Wiederöe [4] in the second half of the 1920s. In the following decade circular accelerators like cyclotrons [5] and betatrons [4] were thought up and built, which reached an energy range of MeV.
In 1945 the concept of the so-called synchrotron were developed by E.M. McMillan [6] and built up by in Berkeley at the University of California. In contrast to the other circular accelerator types, the particle orbit in a synchrotron does not increase with the energy, so that this accelerator type can be used as a storage ring. For the then reached energy the radiated energy, which was already theoretically described by A. Liénard in 1900 [7], became relevant and was observed for the first time at the 70 MeV General Electric synchrotron in 1947 [8] and is therefore called synchrotron radiation (*SR*). After initially considering the SR as a vexation because of the caused energy loss, its unique features led to the construction of storage rings as dedicated synchrotron radiation sources, with the first being built in 1968 in Wisconsin, USA [9]. The high brilliance and the the continuous spectrum over a wide frequency range from far infra-red to hard X-rays make the SR interesting as a tool for many areas of application, e.g. medicine, pharmacy and material science. Moreover this radiation can be used for non-invasive investigations of the emitting particle beam, which is splitted into separated groups, the so called bunches.
One example is the Karlsruhe Research Accelerator (*KARA*) at the Karlsruhe Institute of Technology (*KIT*), which is operated as an accelerator test facility and synchrotron light source and where this thesis has been carried out. Not only for synchrotron light sources but for storage rings the provision of a stable beam for long-term measurements is essential. The main parameter for the determination of the beam stability is the beam lifetime, that corresponds to the particle loss rate. Even in the nowadays widely applied so-called top-up operation scheme, in which an additional beam can be injected from the pre-accelerators repeatedly to keep the beam current constant, the lifetime is of great interest. The lifetime defines the injection rate and affects thereby issues like radiation protection.
The total lifetime is mainly determined by elastic and inelastic scattering processes between the particles of the beam and the rest gas atoms in the beam pipe [10]. In modern-days accelerator facilities very low pressures are reachable so that the beam lifetime is not only limited by the rest gas scattering but also inner-bunch scattering processes. These are described by the Touschek effect and therefore determine the Touschek lifetime [11, 12]. This depends mainly on the particle density in a bunch which is why it is possible to increase the lifetime due to bunch lengthening. At the Photon Factory storage ring at High Energy Accelerator Research Organization (KEK), they performed a RF PM at a frequency of 2 times the synchrotron oscillation frequency [13, 14] observed not only a lifetime elongation but also a suppression of coupled-bunch instabilities, which was systematically investigated

in the Brazilian synchrotron light source (LNLS[1]) [15].
At KARA the energy is ramped after the injection from 500 MeV to a maximum of 2.5 GeV, why the beam lifetime is essential for long-term measurements and experiments. We included the function of phase modulation into the low-level RF (*LLRF*) system, so that the amplitude and the frequency of this modulation can be varied [16].
In this thesis a systematic investigation of the phase modulation affect on the bunch length and its longitudinal profile is done to find the optimum condition for the KARA accelerator operation. Therefore I was focused on the three relevant parameters and conditions, namely the modulation amplitude in a range of 10 % to 20 % of the synchronous phase, the modulation frequency around twice the synchrotron frequency and the beam current. The theoretical framework in Chapter 2 introduces the basics of accelerator physics and has a closer look at the single particle motion under PM at twice the synchrotron frequency. After Chapter 3 gives a short overview over the synchrotron light source KARA and the SC used for the bunch length measurements, Chapter 4 describes the execution of the PM experiments and the following data analysis. In Chapter 5 the influence of the phase modulation on the bunch shape for a modulation frequency at the $2f_s$ resonance as well as for positive and negative deviation is presented. In the following chapter the concept of the bunch parameter detuning curve is introduced, which shows the dependence of this parameter on the modulation frequency. Because KARA is no top-up accelerator, the beam current decreases with time, why the beam current dependency of the optimum condition is of great interest and is discussed in the second part of this chapter. At the end of this thesis in Chapter 7 it will be shown, how the total and especially the Touschek lifetime are affected by the bunch lengthening due to the phase modulation.

[1] Laboratório National de Luz Síncrotron

2. Theoretical framework

This chapter provides the necessary theoretical framework for this thesis. In the first part, the theoretical basics of accelerator physics and storage rings are explained. Subsequently the incoherent synchrotron radiation (*ISR*), as well as the coherence condition for the coherent synchrotron radiation (*CSR*), are described. The next section takes a closer look at the limiting factors of the beam's lifetime and therefore explains the Touschek effect and lifetime. In the last section, the possibility of bunch enlarging due to phase modulation (*PM*) is discussed with a detailed look at the single-particle motion.

2.1. Introduction to accelerator physics

This section gives a brief introduction into the working principles of particle accelerators, particularly circular accelerators. A more detailed insight can be found in textbooks like [17] or [18].

2.1.1. Acceleration of charged particles

A particle with the charge q and the velocity $\vec{v}$ that travels through an electromagnetic field experiences a longitudinal and transversal acceleration by the Lorentz force

$$\vec{F} = q \cdot \left(\vec{E} + \vec{v} \times \vec{B}\right), \tag{2.1}$$

where $\vec{E}$ is the electric and $\vec{B}$ the magnetic field. The particle's motion inside the electromagnetic field from $\vec{r}_1$ to $\vec{r}_2$ results in an energy gain of

$$\Delta E = \int_{\vec{r}_1}^{\vec{r}_2} \vec{F} \cdot \mathrm{d}\vec{r} = q \cdot \int_{\vec{r}_1}^{\vec{r}_2} \left(\vec{E} + \vec{v} \times \vec{B}\right) \cdot \mathrm{d}\vec{r}\,. \tag{2.2}$$

Because the given $\mathrm{d}\vec{r}$ is always parallel to the velocity, the term $\left(\vec{v} \times \vec{B}\right) \cdot \mathrm{d}\vec{r}$ equals to zero, therefore the energy gain does not depend on the magnetic field. Consequently, Equation (2.2) simplifies to

$$\Delta E = q \cdot \int_{\vec{r}_1}^{\vec{r}_2} \vec{E} \cdot \mathrm{d}\vec{r} = q \cdot U \tag{2.3}$$

where U is the potential difference between the points $\vec{r}_1$ and $\vec{r}_2$. In contrast to the energy gain, a deflection can be achieved either by electric or magnetic fields.
According to Equation (2.1) , deflection of a highly relativistic particle requires an electric field that is by a factor of c higher compared to the usage of a magentic field. Therefore magnets are generally used to guide the particles.
The component of the Lorentz force which is orthogonal to $\vec{v}$, generated by a constant

magnetic field, acts as a centripetal force

$$\frac{m \cdot v^2}{\rho} = q \cdot v \cdot \left|\vec{B}\right| \tag{2.4}$$

with the particle's mass m and the bending radius ρ. Hence, for relativistic particles $|\vec{v}| = v \approx c$, the radius grows linear with the particle's energy or momentum

$$\rho = \frac{p}{q \cdot B} = \frac{E}{c \cdot q \cdot B}. \tag{2.5}$$

2.1.2. Synchrotron as storage ring

One type of circular accelerators, which is also usable as a storage ring, is the so-called synchrotron, which was developed in the 1940s. Unlike in other circular accelerator types such as cyclotrons, the particle orbit in a synchrotron is constant. To keep the particles on this constant orbit, it follows from Equation (2.5), that the magnetic field has to increase synchronously with the particle's energy. Electrostatic fields were previously used for the particle acceleration, which were limited by the breakdown voltage, where spark-over occurred. These days time-dependent fields are used. In principle, only one radio frequency (*RF*) acceleration section is necessary in synchrotrons. Usually, these provide the sinusoidal voltage

$$U_{\mathrm{RF}}(t) = U_0 \cdot \sin\left(2\pi \cdot f_{\mathrm{RF}} \cdot t + \Psi_{\mathrm{s}}\right) \tag{2.6}$$

with the acceration voltage (*AV*) amplitude U_0, the RF-frequency f_{RF} and the synchronous phase Ψ_{s}. If the energy gain per turn is as high as the losses, a synchrotron can be used as a storage ring, in which the magnetic field is constant.
To regain the energy lost in every turn, the RF-voltage must have the same phase for each turn. This results in a strict relation between f_{RF} and the revolution frequency f_{rev}

$$f_{\mathrm{RF}} = h \cdot f_{\mathrm{rev}} \tag{2.7}$$

where h is an integer called harmonic number and also defines the maximum number of bunches in the ring. All particles add up to the beam charge q_{beam} and hence the beam current is defined as

$$I_{\mathrm{beam}} = q_{\mathrm{beam}} \cdot f_{\mathrm{rev}}. \tag{2.8}$$

2.2. Beam dynamics

According to Equation (2.5), each particle with a fixed momentum p travels on a path with a constant deflection radius. The synchronous particle and its orbit are defined to hold the reference momentum p_{s}. Because of the momentum spread and the divergence, additional beam guiding elements are necessary to keep the particles on stable and closed orbits. In the first part of this section, primarily based on [19], the influence of focusing quadrupole magnets on the transversal particle movement is discussed. The second part describes the longitudinal motion relative to the synchronous particle.

2.2.1. Transversal beam dynamics

In addition to the bending dipoles, quadrupole magnets are used for the transversal beam focusing. Inside these magnets, the magnetic field is linearly dependent on the distance to the geometric center [19]

$$B_{\mathrm{x}}(y) = -g \cdot y \tag{2.9}$$

$$B_{\mathrm{y}}(x) = -g \cdot x \tag{2.10}$$

with the constant gradient $g = \frac{\partial B_\mathrm{x}}{\partial y} = \frac{\partial B_\mathrm{y}}{\partial x}$. Multipoles up to the order of quadrupoles are referred to as linear beam optics.
Because of this field gradient, the deflection depends on the particle's transversal position. From the geometry of the field, it follows that in only one transversal plane, the force has a focusing effect on the particles, whereas the beam is defocused in the other one. To reach a beam focusing in both planes at least two quadrupoles are needed, where the focusing plane of the second has to be the defocusing plane of the first magnet.
So-called Hill's equations can describe the particle's transverse movement around the synchronous particle in the field of magnetic dipoles and quadrupoles [19]

$$u''(s) + K(s) \cdot u(s) = 0. \tag{2.11}$$

Here $u(s)$ is the transversal deviation in x or respectively y. $K_\mathrm{x}(s) = -k(s) + \frac{1}{\rho(s)^2}$ and $K_\mathrm{y}(s) = k(s)$ are periodic functions with the bending radius of the dipole ρ and quadrupole strength parameter $k = \frac{e}{p} \cdot g$. A solution of Hill's equation is given by

$$u(s) = \sqrt{\epsilon \cdot \beta(s)} \cdot \cos\left(\Psi(s) + \Psi_\mathrm{s}\right) \tag{2.12}$$

with the single particle emittance ϵ, the β-function and the phase Ψ. The emittance is defined as the area of an ellipse, which is enclosed by the particle's trajectory in the transversal phase space (u,u') spanned by the particles transverse position and transverse momentum. This oscillatory motion is called betatron oscillation. By

$$\Psi(s) = \int_0^s \frac{\mathrm{d}\tilde{s}}{\beta(\tilde{s})} \tag{2.13}$$

the β-function and phase are directly connected. According to Liouville's theorem [20], the area, enclosed by the ellipse in the phase space, is constantly under the influence of conservative forces, while the orientation and shape can change.
From Equation (2.12) follows directly, that for each point of the beam pipe the particle with maximum transversal deviation fulfill $\cos\left(\Psi(s) + \Psi_\mathrm{s}\right) = \pm 1$. Therefore an envelope $E(s)$, which contains all particles, is given by

$$E(s) = \pm\sqrt{\epsilon \cdot \beta(s)}. \tag{2.14}$$

In the previous considerations each particle was assumed to have the same momentum p_s. If small deviations Δp are taken into account, with Equation (2.5) the particles have different bending radii inside the dipole magnets, which leads to dispersive effects. The dispersion results in an additional correction term for the solution of Hill's equations [21]

$$u(s) = \sqrt{\epsilon \cdot \beta(s)} \cdot \cos\left(\Psi(s) + \Psi_\mathrm{s}\right) + D_\mathrm{u}(s)\frac{\Delta p}{p} \tag{2.15}$$

with the dispersion $D_\mathrm{u}(s)$, which is the transversal deviation from the reference particle's track for particles with a momentum deviation $\frac{\Delta p}{p} = 1$. The dispersion inside a dipole magnet depends on the bending radius, which is why the dispersion in the vertical plane is insignificant.
Based on this, the transversal size of a bunch, the so-called beam size $\sigma_\mathrm{u}(s)$, is defined as the the envelope of the betatron oscillation with an additional correcting dispersion term [21]

$$\sigma_\mathrm{u}(s) = \sqrt{\epsilon \cdot \beta(s) + \left(D_\mathrm{u}(s)\frac{\sigma_\mathrm{p}}{p}\right)^2} \tag{2.16}$$

with the bunch's root mean square (*RMS*) momentum spread σ_p.

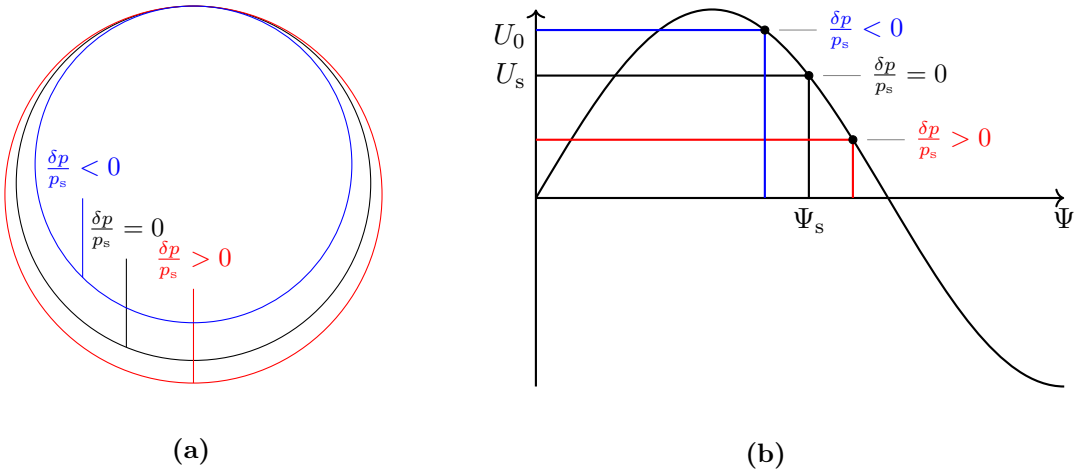

(a) (b)

Figure 2.1.: Principle of phase-focussing (a) Particles with higher momentum than the synchronous particle (black line) move on a longer path (red line). In contrast, lower momentum results in a shorter path (blue line). (b) The longer path and therefore, the delayed arrival in the accelerating structure leads to a different phase so that the particles experience a smaller acceleration voltage and vice versa, the particles with lower energy arrives earlier and gain more energy. This figure is based on [19].

X-y coupling

From a theoretical point of view the vertical dispersion vanishes in an ideal flat ring, therefore the vertical emittance would be zero. In reality a small emittance in the order of $\epsilon_y \approx 10^{-13}\,\mathrm{m}$ [22] occurs because of the recoil by emitting photons in a cone with finite opening angle, described in Section 2.2.2, into the vertical plane.
In practice the vertical emittance is dominated by coupling between the horizontal and vertical plane. Coupling can occur due to misalignment or tilts of elements e.g. bending magnets, so that a deflection into the vertical plane arises. From the natural emittance ϵ_{nat}, the horizontal and vertical emittance can be calculated [17]

$$\epsilon_x = \frac{1}{1+\kappa}\epsilon_{nat} \tag{2.17}$$

$$\epsilon_y = \frac{\kappa}{1+\kappa}\epsilon_{nat}. \tag{2.18}$$

For the Karlsruhe Research Accelerator (*KARA*) storage ring, the coupling-strength is assumed to be $\kappa \approx 1\,\%$.

2.2.2. Longitudinal beam dynamics

The accelerating RF voltage $U_{RF}(t)$ is adjusted so that the synchronous particle passes the cavity with the synchronous phase Ψ_s. This phase is chosen that the gained energy in the acceleration section compensates exactly the losses due to the synchrotron radiation and can be calculated by $\sin\Psi_s = \frac{V_0}{e \cdot U_0}$ with the energy loss through synchrotron radiation V_0, which is defined by Equation (2.24) and described later in Section 2.3.
All particles with a negative relative momentum deviation $\frac{\delta p}{p_s} < 0$ have lower energy and momentum than the synchronous particle and therefore experience a stronger deflection by the bending magnets. This results in a shorter orbit, which is illustrated in Figure 2.1a. In the ultra-relativistic case ($v = c$), the arrival time only depends on the path length, so those particles arrive earlier at the RF section and are exposed to a higher AV and gain more energy concerning the reference particle (see Figure 2.1b). Vice versa, higher energy leads to a longer path and subsequently to delayed arrival and a smaller energy gain.

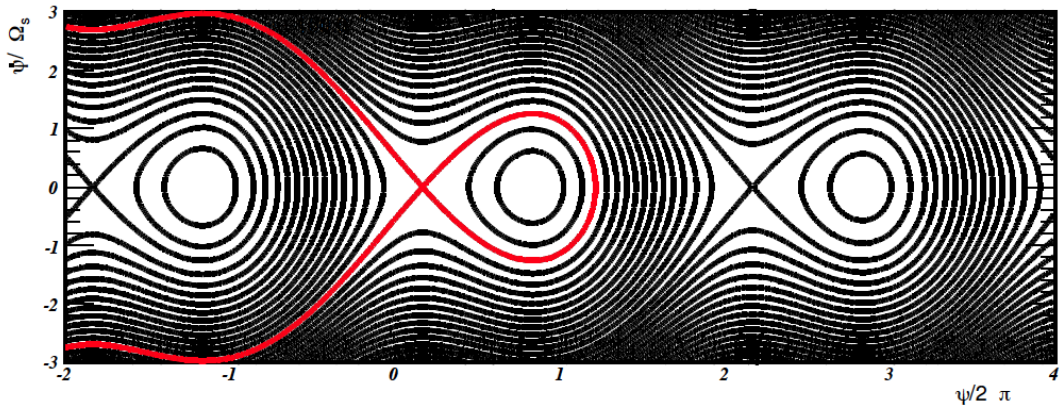

Figure 2.2.: Separatrix The separatrix (red line) separates the stable (inside) and instable (outside) particle trajectories in the longitudinal phase-space [19].

In both cases, momentum and energy get closer to that of the synchronous particle, which is the reason why this effect is called phase focusing. Over multiple turns, the particles come closer and closer to the reference orbit. When the particles reach the synchronous phase, the momentum offset is already overcompensated, which results in the so-called synchrotron oscillation. The frequency of this oscillation is given by [17]

$$f_\mathrm{s} = f_\mathrm{rev}\sqrt{\frac{h\cdot\eta_\mathrm{c}}{2\pi\cdot E}\cdot q\cdot U\cdot\cos\left(\Psi_\mathrm{s}\right)} \tag{2.19}$$

with the harmonic number h and the transition factor $\eta_\mathrm{c} = \alpha_\mathrm{c} - \frac{1}{\gamma^2} \overset{v\to c}{\to} \alpha_\mathrm{c}$, which converges to the momentum compaction factor α_c in the ultrarelativistic case. This factor depends on the magnetic lattice of the accelerator and describes the relation between the relative deviation of particle's orbit length and momentum

$$\frac{\Delta L}{L_0} = \alpha_\mathrm{c}\frac{\Delta p}{p_\mathrm{s}}. \tag{2.20}$$

The momentum-compaction-factor is also calculated by the integral of the dispersion over a whole turn [18]

$$\alpha_\mathrm{c} = \frac{1}{L_0}\oint\frac{D(s)}{\rho(s)}\mathrm{d}s \tag{2.21}$$

In first order it is only the dispersion inside the bending magnets, where ρ is finite, that makes a contribution. The RMS bunch length can be calculated by

$$\sigma_\mathrm{bunch} = \frac{c\left|\alpha_\mathrm{c}\right|}{2\pi\cdot f_\mathrm{s}}\cdot\frac{\sigma_\mathrm{p}}{p_\mathrm{s}} \tag{2.22}$$

with the machine dependent parameters α_c, the natural momentum spread $\frac{\sigma_\mathrm{p}}{p_\mathrm{s}}$ and the synchrotron frequency f_s. In Figure 2.2 possible trajectories in the longitudinal phase space are illustrated. The so-called RF-bucket is the area of all stable trajectories which is confined by the largest closed and thereby stable trajectory - the so-called separatrix shown in red. If the oscillation amplitude is larger than the length of the bucket, the particles get lost because their combination of energy and momentum is not inside the separatrix. The maximum momentum deviation, above which the particles get also lost, can be described by the height of the bucket and is called momentum acceptance (MA). This will be discussed in Section 2.4.1.

2.3. Synchrotron radiation

Each accelerated charged particle loses energy through the radiation of electromagnetic waves, based on the fundamental rules of electrodynamics [23]. The total emitted power in the relativistic case can be described with the Lorentz-invariant version of the formula for the classic case by Larmor. Since the emission for longitudinal acceleration is insignificant, only the radiation power, induced by transversal acceleration, is taken into account [19]. Because this radiation was observed the first time at a synchrotron, it is called synchrotron radiation. The formula of the radiation power for transversal acceleration was already described by Liénard at the end of the 19th century and is given by [18]

$$P_\mathrm{s} = \frac{e^2 \cdot c}{6\pi \cdot \epsilon_0} \frac{1}{(m_0 \cdot c^2)^4} \frac{E^4}{\rho^2} \tag{2.23}$$

with the dielectric constant in vacuum ϵ_0, the particle's rest mass m_0 and the energy E. Insofar as the power scales with $1/m_0^4$, only the light yield of electrons is considered at the energy range of KARA. Also, the scaling with $\frac{E^4}{R^2}$ implies that increasing/decreasing of the power can be achieved easier by a change of the beam energy rather than the bending radius.
The emitted energy for one revolution, as mentioned in Section 2.2.2, determines the stable phase and is compensated in the RF cavities. With the assumptions of a constant bending radius and power radiation, the energy loss can be determined by integrating the radiation power over the time inside the magnets [19]

$$V_0 = \oint P_\mathrm{s} \cdot \mathrm{d}t = P_\mathrm{s} \cdot t_\mathrm{b} = \frac{e^2}{3 \cdot \epsilon_0 \cdot (m_0 \cdot c^2)^4} \frac{E^4}{\rho} = \frac{C_\gamma}{\rho} E^4 \tag{2.24}$$

with Sands' radiation constant $C_\gamma = \frac{4\pi}{3} \frac{r_\mathrm{c}}{(m_0 \cdot c^2)^3} = 8.8575 \times 10^{-5} \, \frac{\mathrm{m}}{\mathrm{GeV}^3}$ and the time of flight inside the bending magnets t_b.
In the rest frame of the particle the accelerated particle's radiation has the angle distribution of a Hertzian dipole. In contrast, the angle distribution in the laboratory frame is boosted to a very small cone with an opening angle of $\tan\Theta = \frac{1}{\gamma}$ with the relativistic quantities $\gamma = \frac{1}{\sqrt{1-\beta^2}}$ and $\beta = \frac{v}{c}$. For ultra relativistic electrons with an energy of 2.5 GeV, the angle can be determined with the small-angle approximation $\tan\Theta \approx \Theta = 0.2\,\mathrm{mrad} = 0.01°$.
The pulse length Δt, during which a fixed observer sees the radiation from a single particle, gives the typical frequency of the power spectrum [18]

$$\omega_\mathrm{typ} = \frac{2\pi}{\Delta t} = \frac{3\pi \cdot c \cdot \gamma^3}{2 \cdot \rho}. \tag{2.25}$$

Because of the very short pulse length in the range of attoseconds (10^{-18} s), the synchrotron radiation emits over a wide frequency range. The radiation power per unit frequency is illustrated in Figure 2.3a and given by [18]

$$\frac{\mathrm{d}P}{\mathrm{d}\omega} = \frac{P_\mathrm{s}}{\omega_\mathrm{c}} \frac{9\sqrt{3}}{8\pi} \frac{\omega}{\omega_\mathrm{c}} \int_{\omega/\omega_\mathrm{c}}^{\infty} K_{5/3}(\xi)\,\mathrm{d}\xi \tag{2.26}$$

with the integrated modified bessel function $K_{5/3}$ and the critical frequency ω_c. This is related to ω_typ through

$$\omega_\mathrm{c} = \frac{\omega_\mathrm{typ}}{\pi} = \frac{3 \cdot c \cdot \gamma^3}{2 \cdot \rho}. \tag{2.27}$$

The critical frequency splits the spectrum in two parts of same integrated radiation power. Extending from the single particle spectrum to that of a whole bunch, with an involved

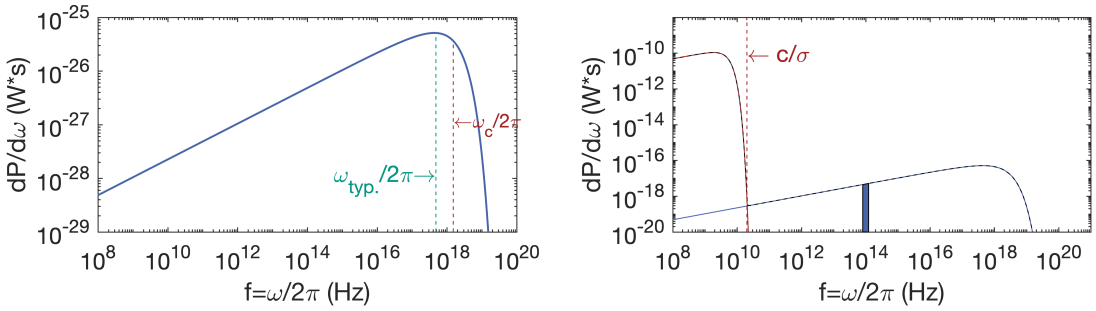

Figure 2.3.: Coherent and incoherent synchrotron radiation spectrum (a) An accelerated electron emits radiation over a wide range of frequencies. The critical frequency (red), divides the spectrum in two parts of same radiation power. (b) If the coherence condition is fulfilled in a particle bunch, the CSR power (red) exceeds the ISR power by the number of particles $N_e = 10^9$. In this, the colored area represents the frequency range of the synchrotron radiation spectrum, which is coupled out at the visible light diagnostic port (λ =390–600 nm). The spectrum in both figures is based on a Gaussian charge distribution with the bunch length σ=50 ps.

number of electrons in the order of $N_e \approx 10^9$, the bunch's incoherent synchrotron radiation spectrum is

$$\frac{\mathrm{d}P_{\mathrm{ISR}}}{\mathrm{d}\omega} = N_e \frac{\mathrm{d}P}{\mathrm{d}\omega}. \tag{2.28}$$

2.3.1. Coherent synchrotron radiation

Additional to the ISR short bunches also emit CSR. If the photons are emitted nearly in phase, which is given for bunches whose bunch length is in the order or even smaller than the radiated wavelength ($\sigma \leq \lambda$), the radiation power is amplified significantly. For a bunch length of σ=50 ps the coherence condition is fulfilled for frequencies up to $f = \frac{\omega}{2\pi} \approx 2 \times 10^{10}\,\frac{1}{\mathrm{s}}$=20 THz. The spectrum this coherent synchrotron radiation (*CSR*) is illustrated in Figure 2.3b and is given by [17]

$$\frac{\mathrm{d}P_{\mathrm{CSR}}}{\mathrm{d}\omega} = N_e \left(N_e - 1\right) \mathcal{F}(\omega) \frac{\mathrm{d}P}{\mathrm{d}\omega} \tag{2.29}$$

in which the form-factor $\mathcal{F}(\omega)$ describes the dependency of the radiation power on the charge distribution $\rho(\vec{r})$ inside the bunch via its Fourier transformation. If only a Gaussian longitudinal charge distribution of a bunch is taken into account, the form-factor itself is a Gaussian distribution [24]

$$\mathcal{F}(\omega) = \left| \int \rho\left(\vec{r}\right) \mathrm{e}^{i\vec{k}\cdot\vec{r}} \mathrm{d}\vec{r} \right|^2 = \mathrm{e}^{-\left(\frac{\sigma\cdot\omega}{c}\right)^2}. \tag{2.30}$$

The total radiation power per unit frequency is given as the sum of CSR and ISR

$$\frac{\mathrm{d}P_{\mathrm{tot.}}}{\mathrm{d}\omega} = \frac{\mathrm{d}P_{\mathrm{CSR}}}{\mathrm{d}\omega} + \frac{\mathrm{d}P_{\mathrm{ISR}}}{\mathrm{d}\omega} = N_e \left[1 + \left(N_e - 1\right) \mathcal{F}(\omega)\right] \frac{\mathrm{d}P}{\mathrm{d}\omega}. \tag{2.31}$$

Because $\mathcal{F}(\omega)$ is only not negligible if $\omega \leq \frac{2\pi\cdot c}{\sigma}$ is fulfilled, the coherent synchrotron radiation overpasses the ISR by a factor N_e, whereas for higher frequencies only the ISR provides a relevant contribution to the total radiation power, as shown in Figure 2.3b.

2.4. Beam lifetime

On their way traveling along an orbit in a storage ring, particles can get lost for different reasons beside malfunctions of the beam guiding elements, which will be neglected in the following section.
All the different loss effects sum up to the total particle loss rate $\frac{\mathrm{d}N_\mathrm{e}}{\mathrm{d}t}$. The beam lifetime τ is defined as the inverse relative particle loss rate or, equivalently, as the inverse relative current decrease rate $\frac{\mathrm{d}I_\mathrm{beam}}{\mathrm{d}t}$, which is more suitable for accelerator operation [25]

$$\frac{1}{\tau_\mathrm{tot}} = -\frac{1}{N_\mathrm{e}}\frac{\mathrm{d}N_\mathrm{e}}{\mathrm{d}t} = -\frac{1}{I_\mathrm{beam}}\frac{\mathrm{d}I_\mathrm{beam}}{\mathrm{d}t}. \tag{2.32}$$

Particle losses usually determine the total lifetime through elastic (τ_elast) and inelastic (τ_inelast) scattering with residual gas atoms. In the case of elastic scattering with nuclei or electrons, a particle gets lost if the deflection amplitude exceeds the transversal acceptance. In contrast to that, inelastic scattering results in an energy loss through an emitted photon, therefore particles with an energy loss larger than the MA get lost. The impact of quantum excitation (τ_quant) only has to be taken into account if the AV decreases drastically. The total lifetime is then given by

$$\frac{1}{\tau_\mathrm{tot}} = \frac{1}{\tau_\mathrm{elast}} + \frac{1}{\tau_\mathrm{inelast}} + \frac{1}{\tau_\mathrm{quant}} + \frac{1}{\tau_\mathrm{touschek}}. \tag{2.33}$$

The last term is called Touschek lifetime τ_touschek and is described in more detail in Section 2.4.2.

2.4.1. Momentum acceptance

The momentum acceptance (MA) defines the largest momentum deviation the particles can have while still being stored. Therefore the MA is an important quantity for the loss rate when the particle's energy changes. The value of the acceptance, which is given relative to the central momentum, is determined by the lattice MA as well as the RF MA [17, 26].
If a particle has a finite momentum offset in a region with non-vanishing dispersion, it fulfills betatron oscillation around its dispersive orbit, which, with the dispersive orbit, determines the so-called lattice MA. Because of its dispersion dependency, the lattice MA also depends on the position in the ring [25].
As mentioned in Section 2.2.2 the RF momentum acceptance is given by the height of the separatrix. Particles outside this stable region get lost, because their energy loss due to radiation can not be compensated by the energy gain inside the RF cavities. For a single RF system the RF momentum acceptance is given by [27]

$$\left(\frac{\Delta p}{p_0}\right)^2_\mathrm{RF} = \frac{2V_0}{\pi h\,|\eta_\mathrm{c}|\,E_0}\left[\sqrt{\left(\frac{eU_0}{V_0}\right)^2 - 1} - \arccos\left(\frac{V_0}{eU_0}\right)\right], \tag{2.34}$$

with the energy loss per turn V_0 and the synchronous phase $\sin\Psi_\mathrm{s} = \frac{V_0}{eU_0}$.
The smallest value of lattice and RF MA limits the total acceptance, which is why for the user operation mode at KARA only the RF acceptance on the transversal plane has to be taken into account.

2.4.2. Touschek lifetime

In case of very low pressure and therefore low scattering probability, the lifetime is not only limited by losses through collisions with rest gas atoms but also scattering between particles in a single bunch becomes relevant or even dominant for the lifetime limitation.

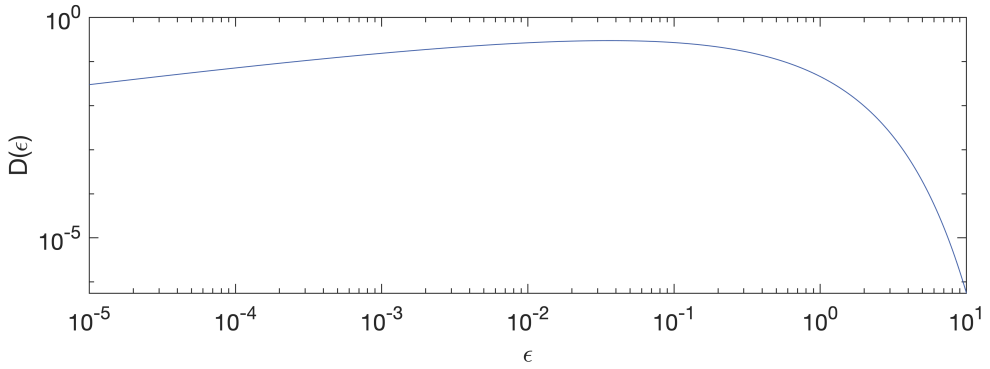

Figure 2.4.: Touschek lifetime function This numeric form factor is defined in Equation (2.38) and is necessary for the determination of the Touschek lifetime.

There are two collision processes possible, where both particles get lost. In the first, two electrons performing synchrotron oscillation, collide, and transfer longitudinal into transversal momentum. In the other collision process, electrons executing transversal betatron oscillation scatter. In this case, the transversal momentum is transferred into longitudinal momentum. The first process is insignificant because the longitudinal momentum spread is much smaller than the radial MA so that the particle can't gain enough transversal momentum to get lost. Thus only the second process can lead to a significant particle loss. This process was first mentioned and described in [12] and is therefore called the Touschek effect.
The calculation of the Touschek lifetime is described in detail in [28]

$$\frac{1}{\tau_{\text{touschek}}} = \frac{1}{N_\text{e}} \left(\frac{\mathrm{d}N_\text{e}}{\mathrm{d}t} \right)_{\text{touschek}} = \frac{\overline{v\sigma}}{N_\text{e}} \int \varrho^2 \mathrm{d}V \ , \tag{2.35}$$

with electron density ϱ, flow rate $\overline{v\sigma}$ and effective loss cross section σ, which is given by the elastic Møller scattering cross section. Under the assumption, that the momentum and position distribution of the particles is Gaussian, the Touschek lifetime is given by [17, 29]

$$\frac{1}{\tau_{\text{touschek}}} = \frac{r_\text{e}^2 \cdot c \cdot N_\text{e}}{8\pi \cdot \sigma_\text{x} \cdot \sigma_\text{y} \cdot \sigma_\text{l}} \frac{\lambda^3}{\gamma^2} \cdot D\left(\epsilon\right) \ , \tag{2.36}$$

where r_e is the classical electron radius, $\sigma_\text{x}, \sigma_\text{y}$ are the vertical and horizontal beam size, σ_l is the bunch length and λ is the MA parameter [17]

$$\frac{1}{\lambda} = \frac{\Delta p}{p} = \sqrt{\frac{2q \cdot U_0}{\pi \cdot \mathrm{h} \left|\eta_\text{c}\right| \cdot c \cdot p_0}}. \tag{2.37}$$

The function D(ϵ) is given by [17, 29]

$$D\left(\epsilon\right) = \sqrt{\epsilon} \left[-\frac{3}{2} \mathrm{e}^{-\epsilon} + \frac{\epsilon}{2} \int_\epsilon^\infty \frac{\ln u}{u} \mathrm{e}^{-u} \mathrm{d}u + \frac{1}{2} \left(3\epsilon - \epsilon \cdot \ln \epsilon + 2\right) \int_\epsilon^\infty \frac{\mathrm{e}^{-u}}{u} \mathrm{d}u \right] \tag{2.38}$$

and illustrated in Figure 2.4, with the argument

$$\epsilon = \left(\frac{\Delta p}{\gamma \sigma_\text{p}} \right)^2 \quad \sigma_\text{p} = \frac{mc\gamma\sigma_\text{x}}{\beta_\text{x}}. \tag{2.39}$$

A high particle density $N_\text{e} / \left(\sigma_\text{x} \cdot \sigma_\text{y} \cdot \sigma_\text{l}\right)$ yields a high scattering probability and from Equation (2.36) directly follows a short lifetime. One way to reduce the particle density

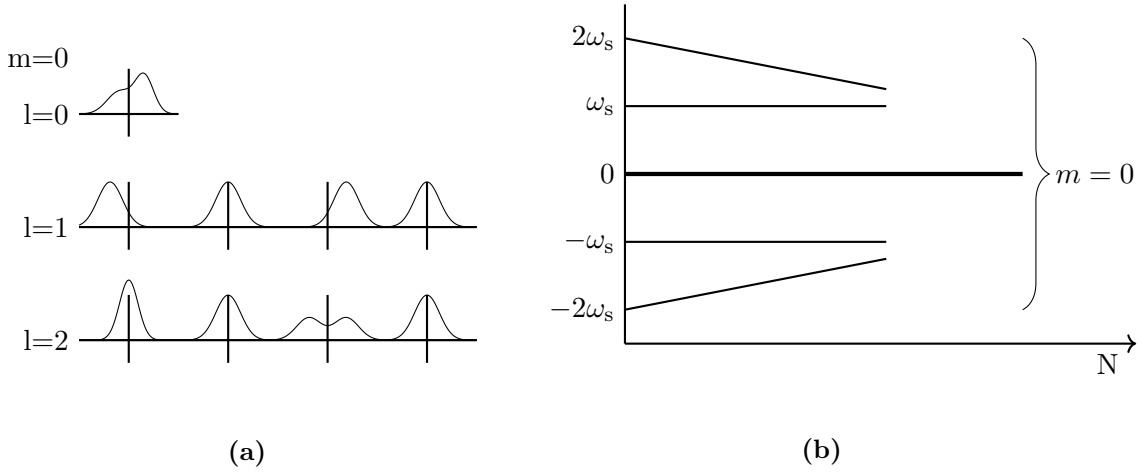

Figure 2.5.: Sketch of longitudinal oscillation modes In (a), the longitudinal bunch structure is illustrated. The first mode $l = 1$ causes a movement of the bunch in total, whereas a second mode oscillation $l = 2$ results in a single particle oscillation around the center of mass and causes a bunch lengthening and shorting. In (b) the mode frequencies are shown and given by $m\omega_\beta + l\omega_\mathrm{s}$. As the intensity N increases, the second mode frequency's absolute value shifts down. In both figures there is no transversal oscillation $m = 0$ (based on [31]).

without reducing the number of electrons is by increasing the bunch length. But it has to be kept in mind, that a lengthening of the bunch not only increases the beam lifetime but also can disturb the time structure of the bunch and the synchrotron radiation [30].

2.5. Phase-modulation

Because, as mentioned in the previous section, the Touschek effect can become relevant for the total beam lifetime, an enlargement of the Touschek lifetime may be of interest. The first part of this section deals with the different longitudinal and transversal oscillation modes and their intensity dependence. In the second part a detailed look at the radio frequency phase modulation (*RF-PM*) around twice the synchrotron frequency and their impact on the bunch length and therefore the Touschek lifetime is taken.

2.5.1. Longitudinal and transversal oscillation modes

Longitudinal oscillation modes yield the opportunity of external excitation for lengthening or stabilization but are also responsible for instabilities in circular accelerators. The longitudinal mode number is thereby denoted by l and the transversal one by m. Throughout this thesis, only the longitudinal motion is considered, Figure 2.5a sketches the first few modes of longitudinal oscillation. The first mode ($l = 1$) causes a movement of the center of mass and bunch in total, whereas a second mode oscillation ($l = 2$) results in lengthening and shorting without a center of mass movement. This happens because there are two stable states of oscillation with opposite phase so that a quadrupole oscillation arises [13]. The unperturbed frequency of the (m,l) mode is $m\omega_\beta + l\omega_\mathrm{s}$ at zero beam intensity with the transversal betatron frequency ω_β and longitudinal synchrotron frequency ω_s. Figure 2.5b sketches dependency of the mode frequency on the beam intensity. In contrast to the $(m = 0, l = \pm 1)$ modes, which do not shift for small and medium intensities, the absolute value of the $(m = 0, l = \pm 2)$ modes' frequencies decrease with increasing beam intensity. This shift in the synchrotron frequency can be calculated by a Taylor expansion of the Hamiltonian by the theory of potential well distortion up to the second-order of z [31]

$$\Delta\omega_\mathrm{s} \approx -\frac{\eta c^2 r_\mathrm{e}}{2\omega_\mathrm{s}\gamma L}\int_0^\infty \rho(z')W_0''(-z')\mathrm{d}z' \tag{2.40}$$

with particle density ρ and second derivative of the wake field W_0'', in which the wake field is the collective field, generated by the whole bunch.

2.5.2. Single particle dynamic under phase modulation

As described before and shown in Equation (2.36) the Touschek lifetime increases proportional to the bunch length σ_l. It is possible to manipulate the longitudinal charge density by applying a RF phase modulation to the accelerating voltage. This modulation can be described by [32]

$$U = U_0 \cdot \sin\left(\omega_\mathrm{RF} \cdot t + m(t) + \Psi_\mathrm{s}\right) \tag{2.41}$$

$$m(t) = \Psi_\mathrm{PM} \cos\left(\omega_\mathrm{PM} \cdot t\right) \tag{2.42}$$

with the amplitude of the RF voltage U_0, the modulation amplitude Ψ_PM and the the modulation frequency ω_PM.
As discussed in Section 2.5.1, the longitudinal excitation is most effective in the range of the parametric resonance stimulation, which is given if the modulation frequency is an integer multiple of the synchrotron frequency. This thesis focuses on modulation around the second harmonic, because there, a lengthening effect without other mode oscillations is expected. For this, the single particle dynamics under phase modulation should be considered closer (based on [13]) under the assumption, that the modulation frequency ω_PM is twice the synchrotron frequency ω_s (so $m(t) = \Psi_\mathrm{PM} \cos\left(2\omega_\mathrm{s} \cdot t\right)$), the modulation of the input RF is the same as the modulation of the accelerating field inside the cavities and beam-loading effects are negligible.
Let, in the following, τ be the longitudinal time deviation from the synchronous position, which is directly connected to the position deviation via the speed of light $\tau = \frac{c}{s}$. Equation (2.20) can thus be rewritten as

$$\frac{\mathrm{d}\tau}{\mathrm{d}t} = -\alpha_\mathrm{c} \frac{\Delta p}{p}. \tag{2.43}$$

Combined with

$$\frac{\mathrm{d}\frac{\Delta p}{p}}{\mathrm{d}t} = \frac{q \cdot U_0 \cos\left(\Psi_\mathrm{s} - \omega_\mathrm{RF}\tau + m(t)\right) - V_0}{T_0 \cdot E_0} - 2 \cdot \gamma_\epsilon \frac{\Delta p}{p} \tag{2.44}$$

the particle's equations of motion are defined, where $T_0 = \frac{L}{c}$ is the revolution time, $q \cdot U_0$, E_0 and V_0 are the parameters of the synchronous particle, Ψ_s is the synchronous phase and γ_ϵ is the radiation damping rate.
In the case where the phase modulation m as well as $\omega_\mathrm{RF}\tau$ is small, the cos-term in Equation (2.44) can be approximated by

$$\cos\left(\Psi_\mathrm{s} - \omega\tau + m(t)\right) = \cos\Psi_\mathrm{s} - m(t)\sin\Psi_\mathrm{s} + \left(\sin\Psi_\mathrm{s} + m(t)\cos\Psi_\mathrm{s}\right) \cdot \omega\tau. \tag{2.45}$$

Together with Equations (2.43) and (2.44) a differential equation of motion follows

$$\frac{\mathrm{d}^2\tau}{\mathrm{d}t^2} + 2\gamma_\epsilon \frac{\mathrm{d}\tau}{\mathrm{d}t} + \omega_\mathrm{s}^2 \left[1 + \epsilon\cos\left(2\omega_\mathrm{s}t\right)\right]\tau = \frac{\omega_\mathrm{s}^2 \Psi_\mathrm{PM}}{\omega}\cos\left(2\omega_\mathrm{s}t\right) \tag{2.46}$$

with a small dimensionless parameter $\epsilon = \Psi_\mathrm{PM}\cot\Psi_\mathrm{s}$.
In fact this is essentially the Mathieu differential equation [33], which describes driven oscillation by change of one parameter at twice its eigenfrequency. In this, the second term on the left-hand side occurs because of the dumping due the synchrotron radiation. The right-hand side characterizes the driving force, which is negligible for a driving frequency far from its eigenfrequency, so that in this case ($2\omega_\mathrm{s} >> \omega_\mathrm{s}$) the equation of motion is

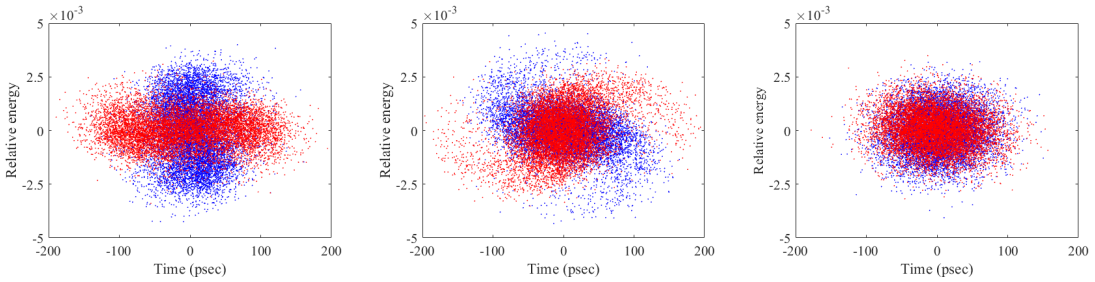

(a) $f_{\mathrm{PM}} = 2f_{\mathrm{s}}$ **(b)** $f_{\mathrm{PM}} = 2f_{\mathrm{s}}-1\,\mathrm{kHz}$ **(c)** $f_{\mathrm{PM}} = 2f_{\mathrm{s}}+1\,\mathrm{kHz}$

Figure 2.6.: Phase space of modulated bunch The simulation results of the longitudinal phase space, for different phase modulation frequencies. The excitation amplitude is 5.7 deg in multi-bunch condition in KARA [34].

reduced to

$$\frac{\mathrm{d}^2\tau}{\mathrm{d}t^2} + 2\gamma_\epsilon \frac{\mathrm{d}\tau}{\mathrm{d}t} + \omega_{\mathrm{s}}^2 \left[1 + \epsilon \cos\left(2\omega_{\mathrm{s}} t\right)\right] \tau = 0. \tag{2.47}$$

This is only valid only for small oscillation amplitudes. An approach for an approximation can be found by

$$\tau(t) = a(t) \sin\left(\omega_{\mathrm{s}} t\right) + b(t) \cos\left(\omega_{\mathrm{s}} t\right) \tag{2.48}$$

where the functions $a(t)$ and $b(t)$ are slowly changing in time, so that a solution for them can be found by averaging over a whole synchrotron period. Thereby an approximate solution for τ is given by

$$\tau(t) = \mathrm{e}^{-\gamma_\epsilon t} \left[C_1 \mathrm{e}^{-\alpha_{\mathrm{g}} t} \cos\left(\omega_{\mathrm{s}} t - \frac{\pi}{4}\right) + C_2 \mathrm{e}^{\alpha_{\mathrm{g}} t} \cos\left(\omega_{\mathrm{s}} t - \frac{3\pi}{4}\right) \right] \tag{2.49}$$

with the constants C_1 and C_2, that depend on the boundary conditions, and the growth rate of the synchrotron oscillation α_{g}, which is defined as

$$\alpha_{\mathrm{g}} = \frac{\omega_{\mathrm{s}} \Psi_{\mathrm{PM}} \cot \Psi_{\mathrm{s}}}{4} \tag{2.50}$$

and is determined by the phase modulation. As you can see in Equation (2.49), synchrotron oscillation increases exponentially only if the growth rate and, therefore, the modulation amplitude Ψ_{PM} is larger than a threshold defined by γ_ϵ. Also, for modulation amplitudes above this threshold, the growth of the synchrotron oscillation and the related bunch length is limited. This saturation is reached as soon as the nonlinear term, which was neglected in Equation (2.47), becomes dominant. So after the equilibrium state is reached, the longitudinal single particle motion can be described as

$$\tau(t) \sim \pm\tau_{\mathrm{sat}} \cos\left(\omega_{\mathrm{s}} t - \frac{3\pi}{4}\right). \tag{2.51}$$

Before the leveling on this saturation amplitude, the time displacement growths exponentially over the several thousand turns [13].

For a detailed look at the substructure on the bunch in dependency on the modulation frequency, it is necessary to expand Equation (2.45) up to higher order terms, that were neglected before. With a Taylor expansion and omitting terms of $\tau^3 m$, it can be written by

$$\begin{aligned} \cos\left(\Psi_{\mathrm{s}} + \omega\tau + m(t)\right) \approx & \left(\cos\Psi_{\mathrm{s}} - \sin\left(\Psi_{\mathrm{s}}\right)\omega\tau - \frac{1}{2}\cos\left(\Psi_{\mathrm{s}}\right)(\omega\tau)^2 + \frac{1}{6}\sin\left(\Psi_{\mathrm{s}}\right)(\omega\tau)^3\right) \\ & - \left(\sin\Psi_{\mathrm{s}} + \cos\left(\Psi_{\mathrm{s}}\right)\omega\tau - \frac{1}{2}\sin\left(\Psi_{\mathrm{s}}\right).(\omega\tau)^2\right) m. \end{aligned} \tag{2.52}$$

This also leads to additional terms in Equation (2.46) with different powers of τ. A more detailed explanation is given in [14]. In the following the case of modulation frequency around twice the synchrotron frequency with perturbation χ will be considered

$$\omega_{\mathrm{PM}} = 2\omega_{\mathrm{s}} + \chi. \tag{2.53}$$

The deviation from the unperturbed synchrotron frequency makes a slightly changed approach for τ necessary:

$$\tau(t) = a(t)\sin\left(\omega_{\mathrm{s}}t + \frac{\chi}{2}t\right) + b(t)\cos\left(\omega_{\mathrm{s}}t + \frac{\chi}{2}t\right) \tag{2.54}$$

Insertion into the expanded differential equation yields a set of coefficients. If higher orders of $\chi, \gamma_\epsilon, \dot{a} = \frac{\mathrm{d}a}{\mathrm{d}t}$ and $\dot{b}$ are neglected those coefficients are given by

$$2\dot{a} + 2\gamma_\epsilon a + (\alpha + \chi)\, b + \kappa b\left(a^2 + b^2\right) = 0 \tag{2.55a}$$

$$2\dot{b} + 2\gamma_\epsilon b + (\alpha - \chi)\, a + \kappa a\left(a^2 + b^2\right) = 0 \tag{2.55b}$$

with the substitutions $\alpha = \frac{\omega_{\mathrm{s}}\epsilon}{2}$ and $\kappa = \frac{\omega_{\mathrm{s}}}{8}$.
In the equilibrium state, that is reached as mentioned after a short period of time, the parameters do not vary with the time anymore ($\dot{a} = \dot{b} = 0$), so that the first term of each equation is equal to zero. For these coupled equations a solution of the form $a = r\cos\Theta$, $b = r\sin\Theta$ can be assumed. Beside the trivial solution $r = 0$ a quadratic solution for r^2 can be found. In [14] it is shown, that the trivial solution corresponds only to stable oscillation, if the absolute value of the deviation is larger than a threshold ($|\chi| > \sqrt{\alpha^2 - 4\gamma_\epsilon^2}$).
However a real solution other than $r = 0$ can only exist, if the condition $\alpha > 2\gamma_\epsilon$ is fulfilled. The quadratic solutions are given by

$$r^2 = \frac{-\chi \pm \sqrt{\alpha^2 - 4\gamma_\epsilon^2}}{\kappa} \tag{2.56a}$$

$$\tan\Theta = \frac{-\alpha \pm \sqrt{\alpha^2 - 4\gamma_\epsilon^2}}{2\gamma_\epsilon} \tag{2.56b}$$

at which the sign in front of the square root has to be identical for both equations.
As you can see, the value of the purely real solution depends on the value of χ.

$\chi > \sqrt{\alpha^2 - 4\gamma_\epsilon^2}$:
r^2 is, independent from the square-root's sign, negative and $r = 0$ is the only solution and therefore the single stable region is at $\tau = 0$.

$|\chi| < \sqrt{\alpha^2 - 4\gamma_\epsilon^2}$:
$r^2 > 0$ is fulfilled for the positive sign of the square-root, so that $r = \pm r_1$ are stable solutions, whereas $r = 0$ doesn't correspond to a stable oscillation. In the near range around twice the synchrotron frequency, consequently two stable oscillation regions exist: $\tau = \pm r_1 \cos(\omega_{\mathrm{s}}t + \frac{\chi}{2} - \Theta_1)$

$\chi < -\sqrt{\alpha^2 - 4\gamma_\epsilon^2}$:
For large negative deviations $r^2 > 0$ for both signs, why the solutions $r = \pm r_{1,2}$ exist, from which r_2 are unstable solutions indeed. So in this case three stable regions exist: $\tau = 0$ and $\tau = \pm r_1 \cos(\omega_{\mathrm{s}}t + \frac{\chi}{2} - \Theta_1)$

This substructure with more than one stable region cause a no longer pure Gaussian particle distribution but an overlap of multiple Gaussians [15]. In Figure 2.6, the longitudinal phase space different modulation frequencies around $2f_{\mathrm{s}}$ are illustrated. The deformation of both the bunch length and the energy spread show a quadrupole mode oscillation. The two spi-

ral arms for the negative deviation in Figure 2.6b, could cause sub-bunches in the bucket [34].

The use of the approach in Equation (2.48), whereby the deviation χ is completely in the slowly varying coefficients $a(t)$ and $b(t)$, allows the description of the particles oscillation amplitude in dependency on the excitation frequency. Also in here, equations for the coefficients can be found by averaging over a whole synchrotron period [34]:

$$\begin{pmatrix} \dot{a}(t) \\ \dot{b}(t) \end{pmatrix} = -\gamma_\epsilon \begin{pmatrix} 1 & 0 \\ 0 & 1 \end{pmatrix} \begin{pmatrix} a(t) \\ b(t) \end{pmatrix} + \frac{\omega_\mathrm{s}\epsilon}{4} \begin{pmatrix} \sin\chi t & -\cos\chi t \\ -\cos\chi t & -\sin\chi t \end{pmatrix} \begin{pmatrix} a(t) \\ b(t) \end{pmatrix} \tag{2.57}$$

With a complex function $\xi(t) = a(t) + ib(t)$, Equation (2.57) can be simplified and solved analytically, so that their solutions are given as

$$a(t) = \xi_0 \exp\left(-\gamma_\epsilon t + \frac{\omega_\mathrm{s} t\epsilon}{4}\cos\chi t\right) \cdot \cos\left(\frac{\omega_\mathrm{s}\epsilon}{4}\sin\chi t\right) \tag{2.58}$$

$$b(t) = \xi_0 \exp\left(-\gamma_\epsilon t + \frac{\omega_\mathrm{s} t\epsilon}{4}\cos\chi t\right) \cdot \sin\left(\frac{\omega_\mathrm{s}\epsilon}{4}\sin\chi t\right) \tag{2.59}$$

So the amplitude the electrons, can oscillated in the exponential term, whereby the oscillation amplitude is determined by $\epsilon \sim \Psi_\mathrm{PM}$. With the assumption, that the deviation χ is much smaller than the synchrotron frequency, the RMS value of the electrons oscillation amplitude can be determined by [34]:

$$\sqrt{\langle\tau^2\rangle} = \frac{\xi_0}{2}\exp\left(-\frac{2\pi n\cdot\gamma_\epsilon}{\chi} + \frac{\omega_\mathrm{s}\epsilon}{4}\cos\left(\sin^{-1}\left(\frac{4\gamma_\epsilon}{\omega_\mathrm{s}\cdot\epsilon}\right)\right)\right) \tag{2.60}$$

with the inter n and the amplitude ξ_0. As seen, the amplitude of the electrons depends on the deviation χ, whose dependency is given by the term $\exp\left(-\frac{2\pi n\cdot\gamma_\epsilon}{\chi}\right)$, that is why the amplitude depends on the sign of χ for non-zero detuning. For the the dependency of the bunch length on the modulation frequency, this means a peak for $\chi = 0$ with asymmetric flanks for negative and positive deviation from the resonance. The ϵ in front of the cos-term, determines, beside the damping rate γ_ϵ the magnitude of the bunch as well, so that the bunch length can be increased with the excitation amplitude Ψ_PM.

3. KARA

The Karlsruhe Institute of Technology (*KIT*) synchrotron storage ring KARA is operated as an accelerator test facility and synchrotron light source. The synchrotron radiation is provided at 23 beamlines, which use different parts of the spectrum for different purposes, e.g., lithography, X-ray fluorescence, or tomography [35]. Beside the beamlines, diagnostic ports are used for beam diagnostics.
To reach the beam energy of 2.5 GeV, the particles pass a chain of multiple pre-accelerators and are ramped up to their final energy in the storage ring, which is described in the first section of this chapter. The ensuing section takes a closer look at the RF system and the way, the phase modulation is generated, primary based on [35, 36, 37]. For the study of the longitudinal beam profile, a streak camera (*SC*) is used, which is why its working principle is explained in Section 3.4. It is located at the visible light diagnostic port (*VLDP*), which is described in the preceding section.

3.1. Accelerator chain & storage ring

Because the storage ring itself can be operated in an energy range from 0.5 GeV to 2.5 GeV a chain of different pre-accelerators is necessary.
The electrons are generated by a thermionic electron gun (*E-Gun*) and are already accelerated to 90 keV within the gun. The following racetrack microtron is build up of two dipoles and a 5.3 MV linear accerator (*Linac*) in-between. The electrons pass the Linac ten times, until they have reached a total energy of 53 MeV [35, 38]. The last pre-accelerator, the booster, is a small synchrotron with a circumference of 26.4 m, the harmonic number $h = 44$, and a simple FODO magnet structure. Over multiple turns, the energy is ramped up to 500 MeV, until the beam is finally injected into the storage ring. The whole booster cycle can be repeated with a frequency of 1 Hz. This process is repeated until the required current is accumulated. Because of the pulse devices' time window, 33 RF-buckets are filled with the electrons.
By varying the injection time into the storage ring, the range of consecutive bunches that are filled can be changed, so that multiple so-called trains with 33 buckets each are filled with electrons. An exemplary filling pattern is shown in Figure 3.2.
The main synchrotron consists of four nearly symmetric bending sections, each composed of two Double-Bend-Achromats (DBAs). The DBA consists of two dipole magnets for the bending and additionally four quadrupoles for the beam focusing. Also, installed sextupoles are necessary for higher-order corrections. In the normal DBA lattice, the dispersion is zero in the straight sections, which are used for insertion devices and the cavities [39]. In contrast to that, the magnets strengths in the here used extended DBA lattice are set such, that the dispersion does not vanish in the straight section, but do reduce the beam emittance. A schematic layout of the storage ring design is given in Figure 3.1. After the injection is finished, the particles can be accelerated up to a maximum energy of 2.5 GeV, although another operation mode at 1.3 GeV exists. Parts of the synchrotron radiation spectrum, ranging from infrared until X-rays, are coupled out at 0°, 5° and 11.25°

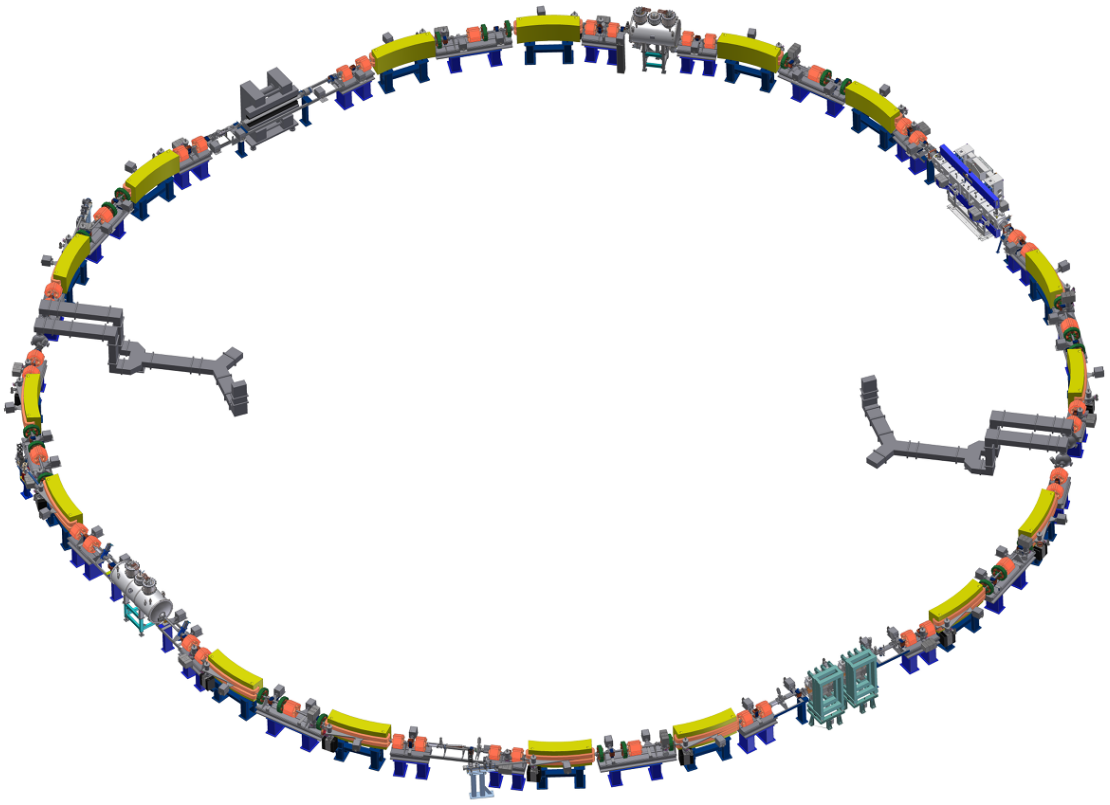

Figure 3.1.: Layout of the KARA storage ring This ring is built up of four nearly symmetric bending section with 4 dipole magnets (yellow) each. A total of 40 quadrupole magnets (red) are used for the beam focusing in the vertical and horizontal plane. In two of the straight sections, two radio frequency (*RF*) cavities are installed in each. The gray parts inside the ring illustrate the waveguide-coupling to a klystron. The synchrotron radiation is coupled out at different ports of the bending magnets and is used for the beamlines as well as for diagnostics [40].

of dipole the magnets with a total bending angle of 22.5° and extracted to 23 beamlines and additional diagnostic ports.

3.2. RF-system

To gain energy and momentum or to compensate the losses via radiation, two cavities are installed in two straight sections each. Because of the storage ring's circumference of 110.4 m, the RF frequency f_{RF}, which is nearly 500 MHz and with Equation (2.7), the revolution frequency is f_{rev} =2.76 MHz. Inside the cavities the electrons are accelerated by a standing electro-magnetic field, that changes with the RF frequency.
Those cavity pairs are waveguide-coupled to a klystron, which provides the RF-voltage. In the normal 2.5 GeV mode, the amplitude of this voltage is ∼350 kV. A higher voltage amplitude causes an increase of the voltage's gradient and therefore, because of the phase-focusing Section 2.2.2, the bunch length can be reduced (seeEquation (2.22)): $\sigma_l \sim \frac{1}{\sqrt{q \cdot U \cdot \cos(\Psi_s)}}$. So the beam parameters such as synchrotron frequency and bunch length can be adjusted properly by changing the acceleration voltage's magnitude.
A low-level RF (*LLRF*) system manages the provision of the desired field in the cavities and stabilizes the output signal with integral loops [36]. This system is also necessary to generate the phase modulation. Therefore the LLRF measures the transfer function from the setpoint to the cavity probe, so that the setpoint signal for the desired cavity

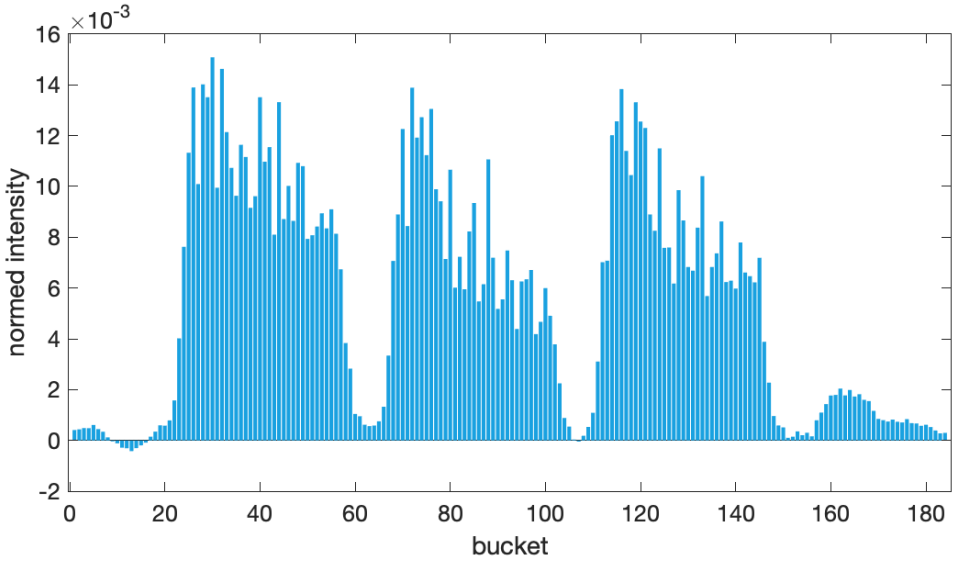

Figure 3.2.: Filling pattern The filling pattern is recorded by the Bunch-By-Bunch (*BBB*) feedback system. A separation of three trains with 33 bunches each, can be seen clearly. This pattern is averaged over around one hour.

field can be calculated and produced. With the generation of setpoint waveforms, it is possible to perform phase and amplitude modulation simultaneously with only 4 calculated parameters: voltage setpoint V_0, amplitude modulation magnitude a_a, phase modulation amplitude Ψ_PM, and relative phase between amplitude and phase modulation waveforms $\Delta\Psi_\mathrm{ap}$. A more detailed description of the LLRF and how the RF-PM is implemented is given in [16].

3.3. Visible light diagnostic port

One of the previously mentioned diagnostic ports is the visible light diagnostic port (*VLDP*), which only is used for beam diagnostics' experiments. It is placed at the 5° port of a dipole magnet and saw the first light in October 2010 [41]. The radiation at this port is inspected by time-correlated single photo counting (*TCSPC*), which measures the filling pattern, the fast-gated intesified camera (*FGC*) for the transversal, and the SC for the longitudinal bunch profile. The used part of the radiation spectrum at this port is visible light with a small amount of ultraviolet. As shown in Figure 2.3b, there is only incoherent synchrotron radiation for this part of the spectrum. This is suitable for beam diagnostics because the ISR's intensity represents the charge distribution directly inside the bunch.

Table 3.1.: KARA key parameter

Parameter	Value
Circumference	110.4 m
bending radius ρ	5.559 m
Beam energy	0.5–2.5 GeV
RF frequency	499.7 MHz
harmonic number h	184
Revolution time	368.2 ns
α_c	0.008670
$\sigma_\mathrm{E,rms}$	2.270 70 MeV

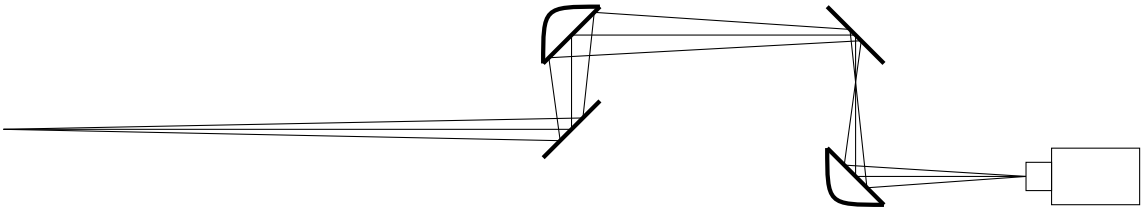

Figure 3.3.: Beam path A cooled aluminum mirror deflects visible part of the beam upwards on a focusing parabolic mirror. The focused pulse propagates through a radiation safety wall into the lab. After being deflected downwards by a planar mirror, a second parabolic mirror focuses the beam to the experiments, which are reached due to mirrors in the horizontal plane, that are not shown in this [21].

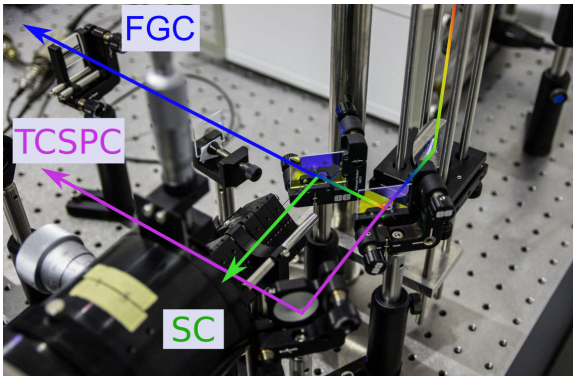

Figure 3.4.: Beam splitter Two shortpass filters split the in three wavelength regions, so that the TCSPC, FGC and SC can operate in the range of their optimal efficiency. The first one spits in the ranges below and above λ =400 nm and the second one separates the wavelength regions λ =400–500 nm and λ =500–600 nm [38].

The first mirror in the guideway, a cooled aluminum planar mirror, separates the visible light from the radiation spectrum and deflects the beam upwards, where it leaves the vacuum pipe through a quartz glass viewport. A first off-axis parabolic mirror focuses the light through a hole in the radiation safety wall into the lab. At the next planar mirror, the light is directed downwards on the level of the experimental table. Before the second and last parabolic mirror focuses the beam on the experiments [41, 21, 38]. The beam path is sketched in Figure 3.3. With a set of two short-pass filters, the light is split into three wavelength regions, so that the experiments operate in the range of their optimal efficiency, as illustrated in Figure 3.4. The first one delivers the range below λ =400 nm for the TCSPC and the second one splits the leftover beam into the parts for the FGC (λ =400–500 nm) and the streak camera (λ =500–600 nm).

3.4. Streak camera

The streak camera is a detector device to investigate the longitudinal particle distribution and is also used to estimate the bunch length and to study its temporal change. For that, it is exploited that the longitudinal profile of the electron bunch is the same as for the synchrotron radiation pulse. At the VLDP at KARA, a Hamamatsu C5680 is used. The working principle is illustrated in Figure 3.5 and is described in detail in [41, 43].
The arriving visible light pulse from the synchrotron radiation (SR) is converted into a pulse of photoelectrons with the same temporal structure by the photo-electric effect at the photocathode. At the end of an evacuated tube, these electrons hit a fluorescence screen, and the emitted photons are detected by a CCD camera array with 1024 × 1280 px. For a better signal-to-noise ratio 2x2 neighbouring pixels are combined to a so-called macropixel,

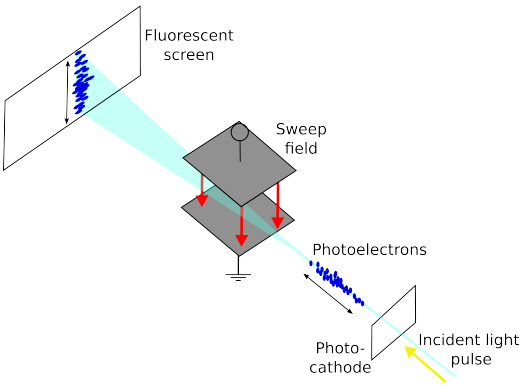

Figure 3.5.: streak camera working principle The incident light pulse, with the same temporal profile as the radiating electron bunch, is converted into an electrons' pulse by hitting a photocathode. On their pathway through an evacuated tube, the charged particles are vertically deflected due to a fast sweeping electric field. Therefore the deflection's magnitude depends on the arrival time so that the longitudinal timing profile is transferred into a spatial one on a fluorescent screen. The photons emitted by the screen are detected by a CCD camera. A second horizontal sweeping field, allows the investigation of the bunch's profile over the time [41, 42].

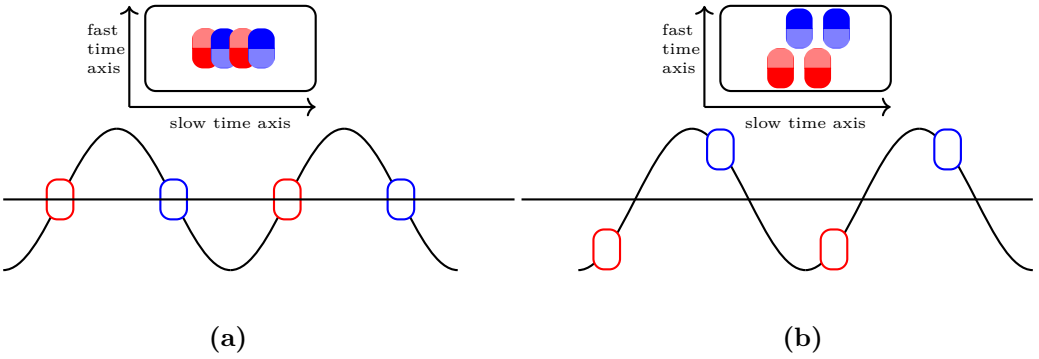

Figure 3.6.: Schematic drawing of delay timing The 250 MHz sine wave is the smallest frequencies to show up all bunches on the SC screen. When the timing is so chosen that the bunches arrive exactly at zero passing, all bunches are spotted on the same vertical spot (a). Indeed, as shown in the upper part, where the bright color symbolizes the bunch's head, the odd bunches are deflected in the other direction than the even ones. Thereby all information about asymmetries of the profile gets lost. With a delay of timing (b) the odd and even bunches can be separated and can be investigated independently.

so that the detection area is segmented into 512×640 px.
The electrons are deflected on their pathway inside the tube by a sweeping field generated between two metallic plates. Therefore the longitudinal temporal profile is displayed spatially on the screen, as shown in Figure 3.5. So it is not only possible to evaluate the pulse length, but also characteristics about the pulse shape can be extracted. The resolution is not only limited by the number of pixels but also by the slit opening outside the photocathode, on which the SR pulse is focused. The width of the longitudinal profile is not only determined by the actual bunch length, but also by the repulsion between charged particles inside the tube so that the longitudinal profile is expanded.
To study also, the temporal behavior of the longitudinal shape's change over multiple turns is of interest. For that purpose, a time range of several hundred nanoseconds to a few milliseconds is needed. On the other side, a picosecond-resolution for the shape and bunch length investigation is necessary. This problem can be solved with a dual sweep unit, which provides an additional time-varying high voltage, which is orthogonal to the first one so that two different time axes are possible. For the streak camera at KARA time

range of the fast axis can be set on 4 steps between 190 ps and 800 ps. For a time range, on the slow axis, larger than 1 µs, the time range per pixel tops the temporal distance between consecutive bunches, so that the signal of multiple bunches or even revolutions are accumulated in a single pixel.
Because also for elongated bunches, the bunch length is well below 200 ps, there is some unused space on the fast vertical axis, if a range of at least 400 ps is set. This space can be used to solve the problem of smearing due to transversal beam size, in the way that two neighboring bunches can be deflected to different spots on the vertical axis, so the odd and even bunches can be investigated independently from each other. This working principle is illustrated in Figure 3.6.
To make this possible, a sine wave with the frequency $\frac{f_{\mathrm{RF}}}{2}$ =250 MHz is used. With a shift in phase due to a timing delay, one becomes upwards, and the other one is deflected downwards so that they are separated on the vertical axis. It has to be mentioned, that - as shown in Figure 3.6b - the longitudinal profile of consecutive bunches is mirrored.
As a consequence of that, the information about bunches' shape gets lost, if the spots overlap, as illustrated in Figure 3.6a. The sine wave signal is generated by the „Countdown Unit“, which is fed by the 500 MHz RF clock, and divides the frequency by two. The clock is synchronized with the bunches and is also used to align and synchronize the starting time of the two sweeping axes [41].

4. Measurements and data analysis

This chapter describes the procedure during the PM experiment at KARA under the use of the streak camera (*SC*). In the first section, the actual execution of the phase modulation experiments and the necessary preparations are explained. The analysis of the data obtained thereby is discussed in the second part of this chapter.

4.1. Measurements

After the preparation and SC setting, the execution of the PM experiment and the therefore measured parameters are explained. Because of precisely measured bunch length, and exactly calibrated SC time axis is necessary, the transfer-function between pixel and time has been measured, which is described in Section 4.1.3.

4.1.1. Experiment preparation

To perform any experiment, the storage ring has to be filled at the injection energy 500 MeV. Therefore, with the previously explained acceleration chain, electron bunches are stored in the ring. For all experiments discussed in this thesis, all magnets are set in the user operation's optic. Because after the ramping to 2.5 GeV, no electrons can be injected anymore, the maximum necessary beam current has to be stored before the ramping. Since the machine and beam settings can vary between different fillings and therefore experiments from the same filling are more comparable, it has been tried to perform multiple different beam current and excitation amplitude settings with a single fill. For better comparability of different experiments, three trains with 33 bunches each, has been filled for all experiments and fillings, to have a direct correlation between the beam and bunch current and thereby one possible tuning knob is fixed.
Before each experiment, it is necessary to adjust the streak camera and focuses the beam. As already shown in Figure 3.5 and described in the previous chapter, the bunch length measurement's resolution, is limited by the width of the slit, because of the spot's elongation on the CCD screen without any deflecting field.
For this reason, the slit's opening, and its position, has to be adjusted in the horizontal and vertical plane. Even if the time resolution on the slow time axis is not important for this work, the V-shaped slit has been set in the way, that the spot has a small horizontal elongation.
In order to do this, both sweeping fields are turned off, so that all the particles are focussed on a small spot on the CCD screen, whose expansion determines the SC resolution. During this adjustment, a small number of camera pixels are exposed to a high intensity, why the incident intensity is reduced by multiple beam filters, to avoid reaching saturation of the camera pixel's signal or even the destruction of the image's intensifier. A exemplary so-called *focus mode* measurement and its horizontal and vertical profiles are shown in Figure 4.1.
For the second part of the adjustments, both sweep fields have to be turned on again,

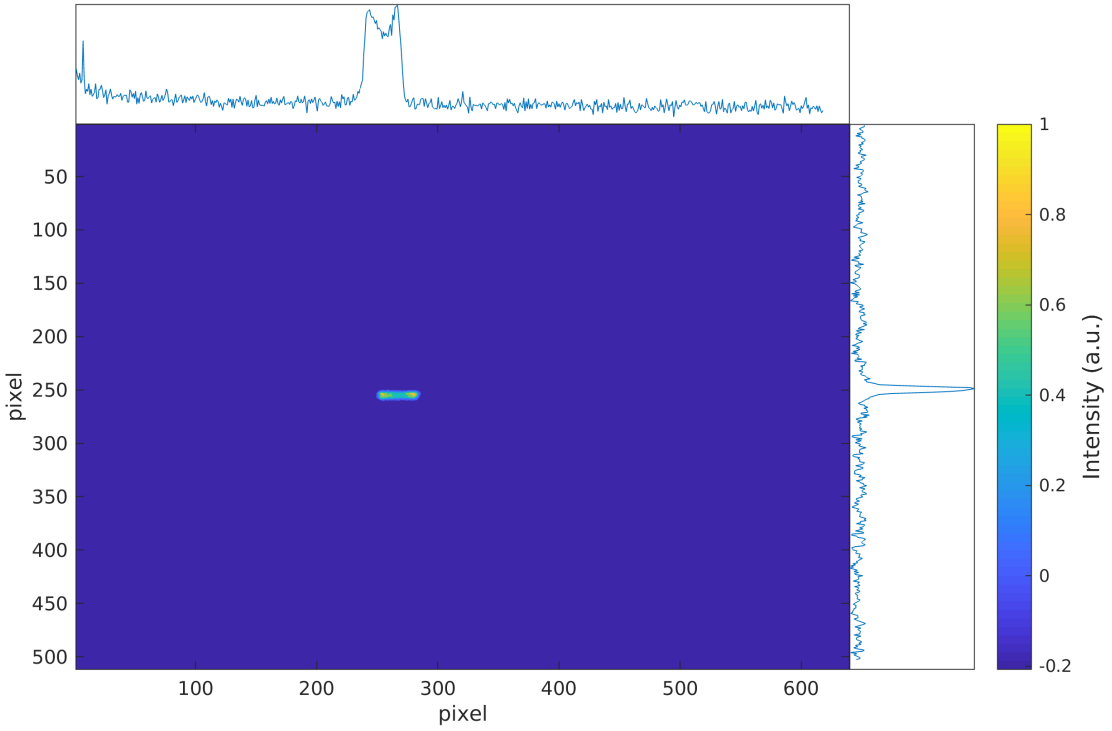

Figure 4.1.: Exemplary focus mode measurement The streak camera image (a) shows after background subtraction a focused spot with a small vertical and horizontal expansion. Particularly the vertical projection at the right, indicates a narrow peak.

by using the SC's *operate* mode. For the synchronization between the accelerating radio frequency and the sweep of the vertical deflecting field, a 250 MHz trigger signal, which is the second sub-harmonic frequency from the RF cavities has to be locked. Because the intensity accumulation per pixel increases with the blanking time of the horizontal axis, all settings for the experiment must be executed with the longest blanking time used, which is the reason to choose a range of 200 µs for this work's measurements. Besides the reduced risk of image intensifier's damage, a small reasonable intensity is also important for the resolution. A high beam intensity at the photocathode results in detachment, a high number of charged electrons, and, therefore, a high space-charge. This can lead to inter-bunch rejection and, in this way, cause a vertical distribution, which does not depend on the longitudinal time structure. So this space-charge effect can, in addition to the slit width, limit the spatial profile's resolution. For this as few filters as possible but as many as necessary, to see a clear bunch signal on the screen, are removed. On top of the filters, the internal micro channel plate (*MCP*) inside the image intensifier is a tuning knob to increase the signal on the phosphor screen without any space-charge effect. The set arbitrary value defines the high voltage value inside the image intensifier so that the signal is amplified and the signal-to-noise ratio is improved [44].
As described in Section 3.4, the odd and even bunches should be placed spatially separated. Because of a natural bunch length in the size of σ =45 ps and the expectation of a bunch lengthening under PM, a vertical separation of two consecutive bunches without overlap can only be achieved with the maximum provided a vertical range of 800 ps, even if the resolution limited for this setting. The value of the timing delay is so chosen that half of the bunches are centered in each half of the SC image.

Table 4.1.: Approximately detuning curve steps

range	steps
0-1000	100
1000-2000	200
> 2000	500

4.1.2. Performing phase modulation experiment

To perform the phase modulation, in a first step the RF autopilot in Control System Studio (*CSS*) has to be switched off so that an automatic correction of the RF voltage to stabilize the synchrotron frequency is turned off. During the experiment it is useful, to have a look at the LLRF panel, which shows the actual waveform, that has to change if a PM parameter is set on a new value, as described in Section 3.2.
For the creating and loading a new ramping profile to the LLRF a Matlab® script, to which the RF section's EPICS PV, that should be modulated, the modulation's frequency ω_{PM} and the excitation amplitude Ψ_{PM} will be handed over, which characterize the PM according to Equations (2.41) and (2.42).

$$U = U_0 \cdot \sin\left(\omega_{\mathrm{RF}} \cdot t + m(t) + \Psi_{\mathrm{s}}\right)$$
$$m(t) = \Psi_{\mathrm{PM}} \cos\left(\omega_{\mathrm{PM}} \cdot t\right)$$

The script writes back the actual set value of the frequency so that the uncertainty is estimated as the difference between the chosen and the actual value. For all experiments for this work, the modulation was performed in the same RF section. The used script also switches the ramping off while a new profile for another setting is calculated.
For each scan measurement the value of the PM amplitude and beam current are fixed whereas the PM frequency $f_{\mathrm{PM}} = \frac{\omega_{\mathrm{PM}}}{2\pi}$ can be variegated. Because of the limited time available for a single scan measurement, it is necessary to do a rough scan to estimate the excitation frequency, which affects the bunch length most effectively, precisely. During a rough frequency scan around $2f_{\mathrm{s}}$, the PM excitation frequency is estimated, which has the most significant visual effect on the bunch length and shape. Besides this assessment of the peak value, this fast scan is also used to check the maximum possible PM amplitude for the given beam current, to avoid an over-excitation. For this, the backward power from the RF cavity should be below a certain threshold.
For the actual frequency scan, a range of $\pm$ (2500 Hz–3000 Hz) around the approximated peak value is investigated, when the scan always started at the smallest frequency and increased from that value. The frequency steps in dependency on the deviation from the maximum, are given in Table 4.1. After setting a new PM configuration to the LLRF system, there were a few seconds to wait until all the settings have been done correctly before a row of SC images has been taken. Since the average bunch length, as well as its change over time, should be investigated, different requirements for resolution and averaging time must be fulfilled. For the average bunch length calculation, which is described in the next section, a horizontal timing range of 200 µs, also used for the adjustment, turned out as suitable. For the determination of the bunch length's changing, however, a higher time resolution is necessary. For this purpose, the time range is set on 100 µs, in order to still reach a significant enough intensity with the same SC settings. These two ranges allow taking data with the same parameters, without changing any filter or MCP amplification settings. At the end of each frequency scan series, 100 images without phase modulation as well as with closed shutter for the background analysis are taken. After this, the whole process can be repeated with different beam current and amplitude setting.

Table 4.2.: Horizontal time axis' transfer function parameter The used transfer function is described by $f(x) = p_3 \cdot x^3 + p_2 \cdot x^2 + p_1 \cdot x$. Thereby the unit of the addends is the same as for the range.

range	p_1	p_2	p_3
100 µs	7.545×10^{-2}	1.358×10^{-6}	-3.095×10^{-10}
200 µs	1.471×10^{-1}	2.889×10^{-6}	1.049×10^{-10}
1 ms	7.403×10^{-4}	7.360×10^{-9}	4.342×10^{-12}

For an additional more detailed lifetime experiment, the same principle for the frequency scan is applied. In this, a long time with a fixed PM parameter is needed to measure the beam lifetime more accurately and with smaller statistical uncertainty. That is why each step is kept for at least 4 min. Because of the longer time, this kind of experiment needs, that number of frequencies steps has to be reduced, so that 7 to 8 levels with a spacing of 500 Hz are taken.
In addition to the streak camera images, there are permanently measured and stored parameters required. The beam's direct current is measured non-destructively with a Direct Current Current Transformer (*DCCT*) and is stored about once a second. The magnetic field of two similar torii is changed periodically up to saturation. An additional field, induced by the passing charged particles, shifts the time of reaching saturation so that the flux of both torii is not canceled out completely. The magnitude of the net flux is used to calculate the beam current [45]. This method allows the measurement of currents in a range from µA to A.
The value of the synchrotron frequency, which is also managed and stored approximately once a minute by the CSS. Therefore the bunch's longitudinal center of charge (*CoC*) is detected by a beam position monitor (*BPM*). Due to a fast Fourier transform (*FFT*) of the data points from about 65000 turns, the frequency spectrum is given. With this bunch's coherent motion can be investigated, so that the coherent synchrotron frequency is calculated as the spectrum's peak position, whereby the value's fluctuation magnitude, based on systematic errors, determines the uncertainty.

4.1.3. SC calibration

The streak camera raw data are stored as **.img* files, which are a 512x640 intensity matrix with parameter settings inside the header. Until here, the matrix axes are the corresponding pixel number without any time information. For the transformation from the pixel number to time information, Hamamatsu® provides a cubic polynomial transfer function. The nonlinearity results from the non-linear field gradient and the trigonometric relation between the deflection angle and the vertical spot on the screen. Because, on the one hand, the accuracy of this function has deteriorated by the SC's age, and on the other hand - especially for the bunch length measurements - a precisely calculated vertical time axis is of great importance, a new calibration has been carried out.
In comparison with the vertical axis, the non-linear terms are nearly negligible for the horizontal transfer function because of the linear sweeping waveform. As there is currently no method at KARA for the horizontal calibration and the given transfer function fitted quite well, a new evaluation on this axis was waived. The used coefficients for the cubic polynomial of the horizontal axis are given in Table 4.2. It has to be noted, that the transfer function is made for the normal and not the superpixels, why in this $(2 \cdot x - 1)$, with the superpixel number x, has to be used.
In this work, the vertical calibration is done only for the used complete range of 800 ps. For this experiment, a very precisely measured bunch shape but no horizontal time resolution is needed. That is why a long horizontal range of 1 ms is chosen. Another reason for the long

vertical sweeping time is the low beam current used for this experiment and the therefore necessary long exposure time, to accumulate a reasonable intensity. The used current of about 1 mA and the operation at the injection energy 500 MeV guarantee both a stable bunch condition and a small parasitic energy loss which could cause the change of the beam's phase on the accelerating field. Also, the RF voltage is increased to a peak-to-peak value of 899.3 kV, which reduces the bunch length as described previously in Section 3.2, so that a more precise measurement of the longitudinal bunch position is possible.
Since the timing signal for the sweeping of the RF accelerating field is not related to the global phase of RF voltage, changing this phase results in a shift of the bunch arrival time and because of that a deflection to another vertical spot. For the manipulation of the RF global phase, the BBB feedback system has to be switched off. Due to that strong couple bunch instabilities can occur, which can be detuned by an increased RF voltage, due to the resulting shift of the synchrotron frequency d_{s}.
For the use of the full range, the odd and even bunches are such separated by the timing delay, that they are spotted at both borders of the screen. In this calibration experiment, the global phase is changed in 10° steps, which corresponds due to KARA's RF frequency (listed in Table 3.1), to a arrival time shift at the SC is given by:

$$\Delta t = \frac{\Delta\Phi}{360^\circ} \cdot \frac{1}{f_{\mathrm{RF}}} \tag{4.1}$$

so that the 10° steps result in a arrival time shift of approximate 55 ps. Here, the steps are chosen so that a suitable compromise between the step number and the time expenses is found. Analogous to the PM experiments, a set of 100 single shots are taken, for each configuration.

4.2. Data analysis

In this work, the SC data has been analyzed with Matlab®. In the first part of this section, recalibration results and the new transfer-function between pixel and time is presented. Afterward, the calculation of the relevant parameter according to the PM and Touschek lifetime experiments are explained.

4.2.1. SC calibration

In Figure 4.2 the SC images after the background subtraction for 4 different phases are shown. As described in the previous section, the two bands go away from the border during the enlargement of the global phase, whereby the gab between the bands is reduced up to $\Phi \approx 60^\circ$, where the spots of the odd and even bunches overlap. For larger phase shifts the bands change their position.
For this calibration only the position of the longitudinal CoC, dependent on the timing delay, is of interest. To analyze this, the vertical projection integrated over all 640 columns is taken for each of the 100 single shot images. The averaged projection is shown exemplary for $\Phi = 0^\circ$ is shown in Figure 4.3a. The error-bar on the y-axis corresponds to the standard error of the mean (*SEM*):

$$\sigma_{\bar{\mathrm{x}}} = \frac{\sigma}{\sqrt{N}} \tag{4.2}$$

,which is determined with the mean $\bar{x}$ and the standard deviation σ:

$$\bar{x} = \frac{1}{N} \sum_{i=1}^{N} x_{\mathrm{i}} \tag{4.3}$$

$$\sigma = \sqrt{\frac{1}{N} \sum_{i=1}^{N} (x_{\mathrm{i}} - \bar{x})^2}. \tag{4.4}$$

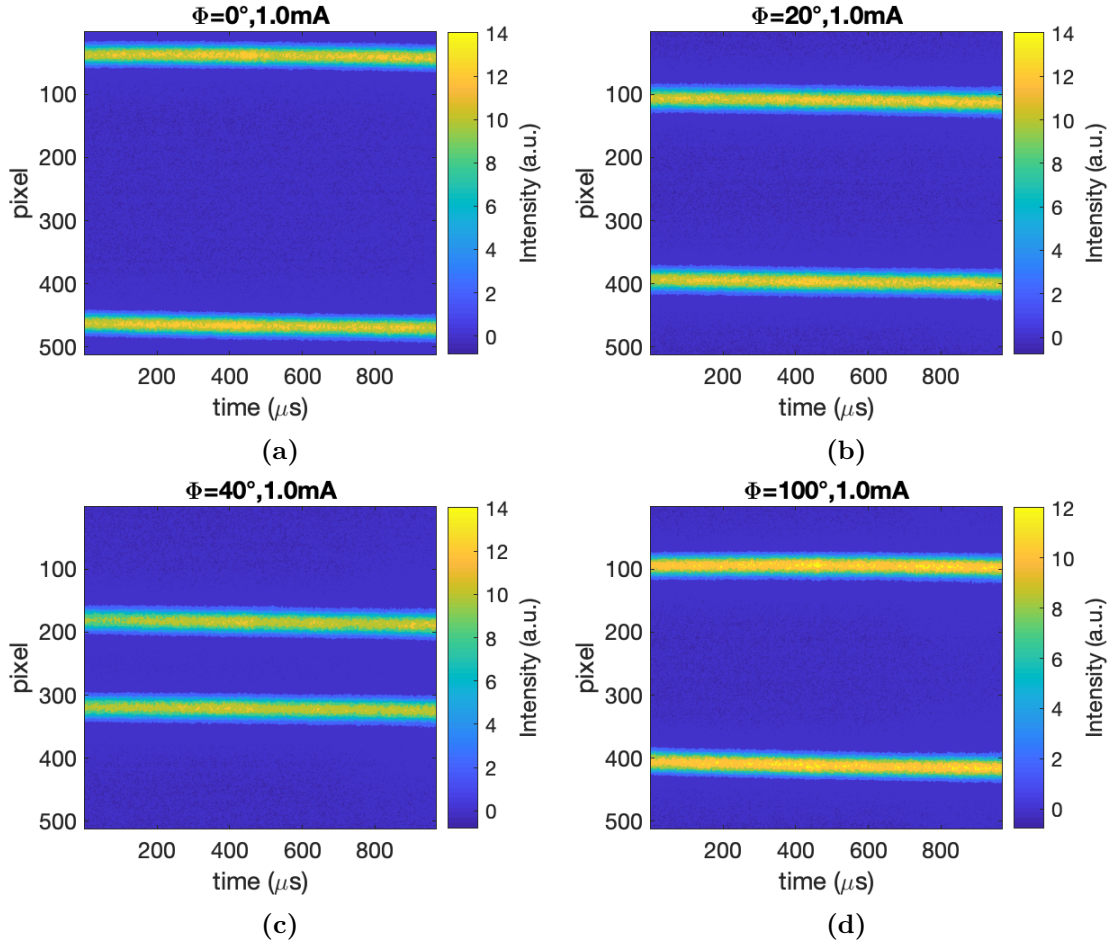

Figure 4.2.: Streak camera images for different global phases From the vertical position of the bunch, the calibration is done.

If nothing else is said, the statistical error is always calculated with the SEM for the 100 images.
Due to the long horizontal accumulation time, averaging out the synchrotron motion, the shape can be described very easily with a Gaussian distribution, which is also displayed in Figure 4.3a. The Figure 4.3b shows the projection for all phase steps, except for Φ=60°, in which the bands overlap. For all the conditions, only half of the projection is used, which contains the part of bunches that are located, for the phase shift Φ =0°, in the upper half. So up to Φ =50° the upper half is displayed, whereas from Φ =70° the lower half of the SC image is shown and analyzed.
For the determination of the peak position, the projection is fitted with the Gaussian distribution

$$f(x;\mu,\sigma) = A \cdot exp\left(-\left(\frac{x-\mu}{2\cdot\sigma^2}\right)^2\right).$$

For a better adaption to the data points, they are weighted for the fitting with $\frac{1}{\sigma^2}$, so that the values with smaller uncertainties are stronger weighted. This method, with weighed data points, is used for all fits in this work if nothing else is said. The fitting parameter μ gives the bunch's peak position pixel value, and also, the uncertainty on this value can be read out from the fit. Because for this only the peak position and not the peak's width is from interest, there is no systematic error from the slit width to take into account. In Figure 4.4 the time delay, calculated according to Equation (4.1), is plotted versus the peak position pixel. Analogous to the original transfer function, the data are fitted with a

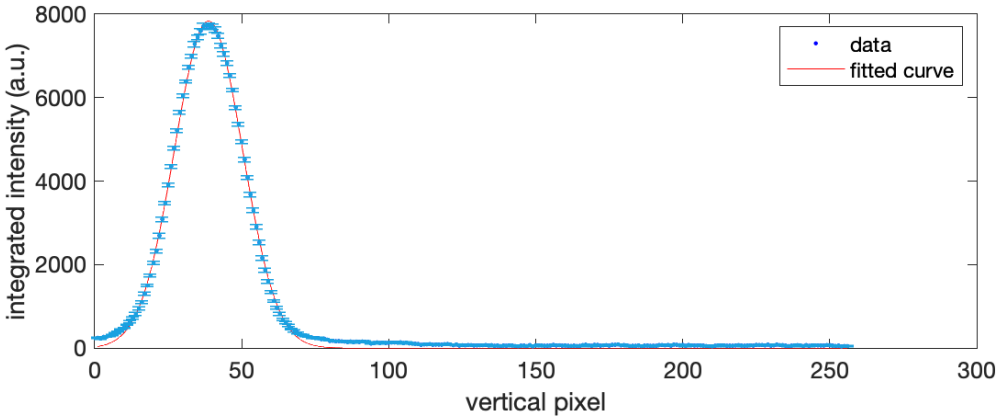

(a)

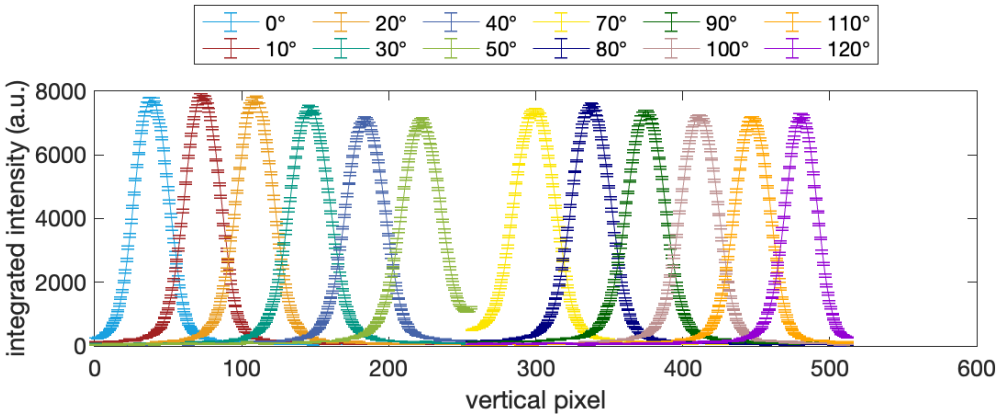

(b)

Figure 4.3.: Bunch projection in dependency of the global phase In (a) the projection of the upper band with the global phase Φ=0° is plotted and fitted with a Gaussian distribution. The projection of one half each is shown in (b). Up to 50° the upper half and from 70° on the lower half is displayed.

cubic polynomial, with the form

$$f(x) = p_3 \cdot x^3 + p_2 \cdot x^2 + p_1 \cdot x + p_0. \tag{4.5}$$

The coefficients and their uncertainties are shown in Table 4.3. Because the absolute value is not of interest, for the transfer from pixel number to time delay, the constant offset p_0 is set to zero, so that the first pixel corresponds to the delay t =0 s. This new calibrated transfer function is used for all the following in this work.

Table 4.3.: Vertical time axis' transfer function parameter

i	p_i	$\sigma_{\mathrm{p_i}}$
0	-64.62	0.29
1	1.711	0.007
2	-1.095×10^{-3}	3.9×10^{-5}
3	1.463×10^{-6}	5.9×10^{-8}

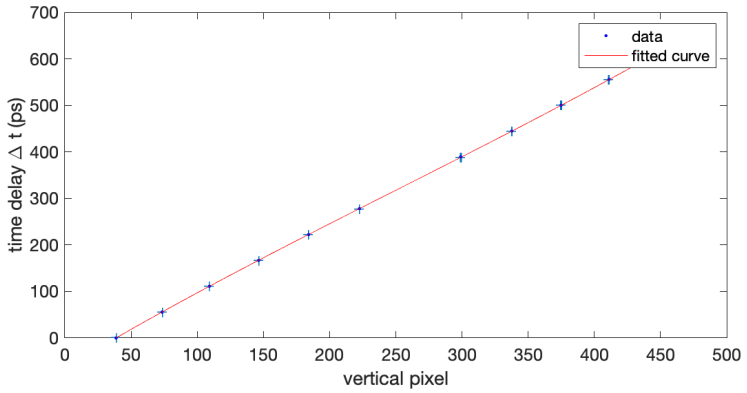

Figure 4.4.: Streak camera time axis calibration The timing delay due to the global phase is plotted versus the corresponding peak position. The data are fitted with an cubic polynomial, for the transfer function of the vertical SC axis.

4.2.2. Bunch's parameter under PM

Besides the SC data, the beam current and synchrotron frequency values are needed to characterize the parameter setting. They both are averaged throughout the experiment, whereby for the current, the SEM is used to define the uncertainty. In contrast to that, the calculated coherent synchrotron frequency's fluctuation is a systematic uncertainty, so that it is determined by Equation (4.4).
In this work, one is primarily interested in the bunch's length and its length oscillation amplitude but also the oscillation amplitude of the bunch's longitudinal position. In contrast to that, the absolute value of the bunch position on the SC screen is not of interest, because it does not have any physical meaning and only depends on the SC's parameters and settings. Figure 4.5 shows the SC image close to the maximum excitation condition's frequency for the parameters (5°/89.5 mA), and it shows up, that the PM influences not only the bunch length but also the longitudinal shape of the bunch. Next to the original data, the vertical projection over all columns (Figure 4.5b) and over a small range of 5 pixel columns, which corresponds to a width of rough 1.5 µs, (Figure 4.5c) are displayed. It can be seen that under these conditions, the longitudinal bunch shape can not be described by a Gaussian distribution. For this reason, another method of length and shape determination and also a different definition of the bunch length is necessary, which allows comparing the parameters of different shaped bunches. The longitudinal position, as well as the bunch length, are calculated via the first and second statistical moment:

$$\mu = \frac{\sum_{i=1}^{N} x_\mathrm{i} \cdot f(x_\mathrm{i})}{\sum_{i=1}^{N} f(x_\mathrm{i})} \tag{4.6}$$

$$\mathrm{Var} = \sigma^2 = \frac{\sum_{i=1}^{N} (x_\mathrm{i} - \mu)^2 \cdot f(x_\mathrm{i})}{\sum_{i=1}^{N} f(x_\mathrm{i})} \tag{4.7}$$

As described in Section 3.4, the width of the SC's slit not only limits the resolution but also enlarges the size of the spot and, therefore, the measured bunch length. To compensate the second effect, the width of the *focus mode* spot σ_slit has to be subtracted from the calculated bunch length

$$\sigma = \sqrt{\sigma_\mathrm{meas.}^2 - \sigma_\mathrm{slit}^2}. \tag{4.8}$$

For that, the width of this vertical spot projection σ_slit has to be calculated in the same way as the measured average bunch length $\sigma_\mathrm{meas.}$, which is estimated from the 200 µs SC-image. Although a better signal-to-noise ration can be reached by using the vertical projection of the whole image, the data matrix has been sliced into slices with a width of 5 pixels

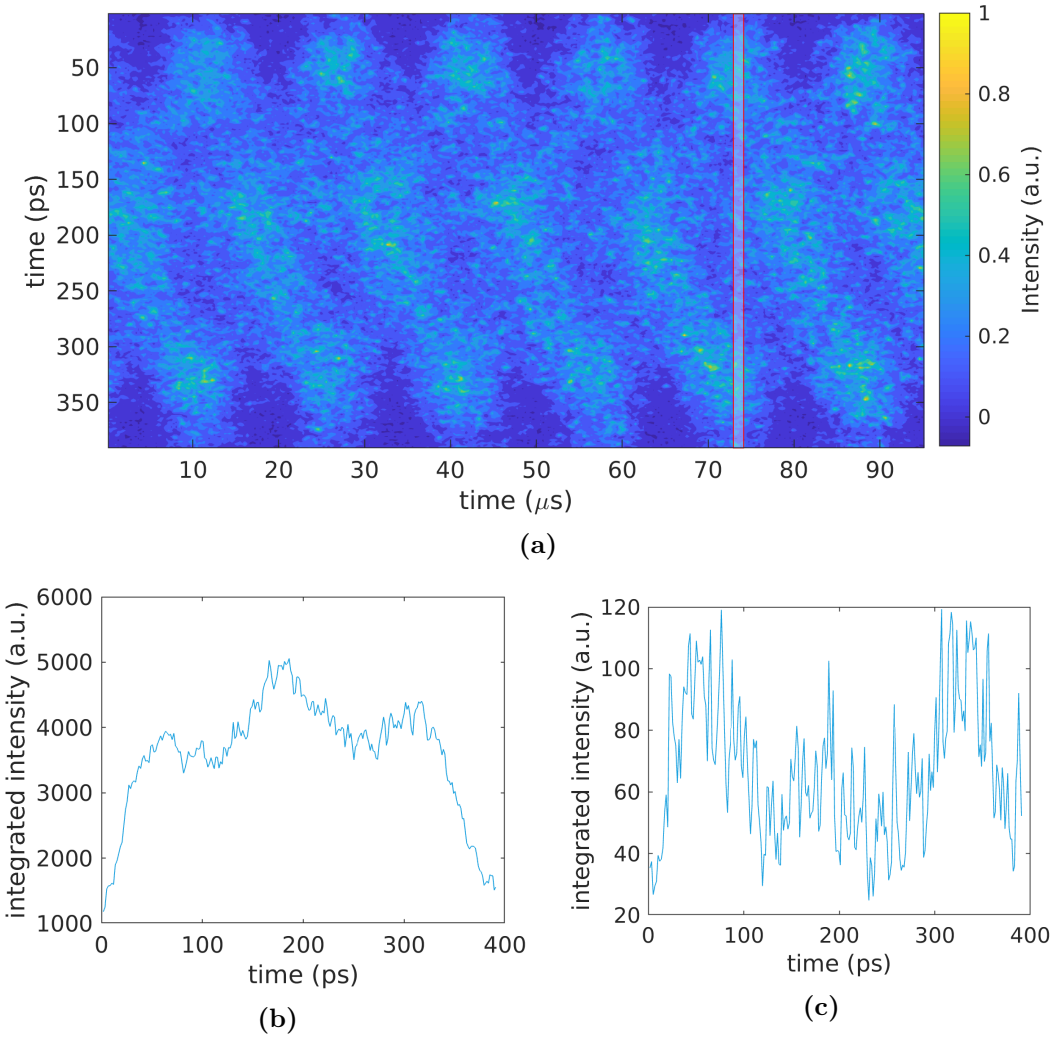

Figure 4.5.: Bunch excitation due to PM The excitation frequency is close to the resonance (a), so that on the vertical projection the bunch's shape, which is averaged over 100 µs differs from a Gaussian shape (b). Additional the projection a slice with the wide of rough 1.5 µs, which corresponds to the grey marked area, shows a complete different shape and the bunch's longitudinal distribution changes over the time (c).

each. This is done to avoid adulteration due to the bunches' longitudinal moving because of the coherent synchrotron oscillation. The slice width corresponds to a time range of approximately 1.56 µs, which is much smaller than the synchrotron oscillation periodic time $T = \frac{1}{f_s} \approx 30\,\mu s$.
For the oscillation amplitude of the bunch's length and position, the images with a horizontal time range of 100 µs are used, whereby the resolution can be increased and smearing over multiple bunches can be decreased. In analogy to the averaged length determination, also here, the image is sliced in 128 strips with a width of 5 pixels each. In this, the bunch length and position are calculated for each strip, so that the oscillation amplitude can be defined as the parameter's standard-derivation.
Because in the SC image, the odd and even bunch are located on different vertical spots, the parameters are calculated separately for both halves. There is no physical reason for differences in the behavior of odd and even bunches. Their derivations are inside the uncertainties, as shown in Figure 4.6 for the conditions (3°/113 mA), so the results of the separated analysis are combined for better statistics.

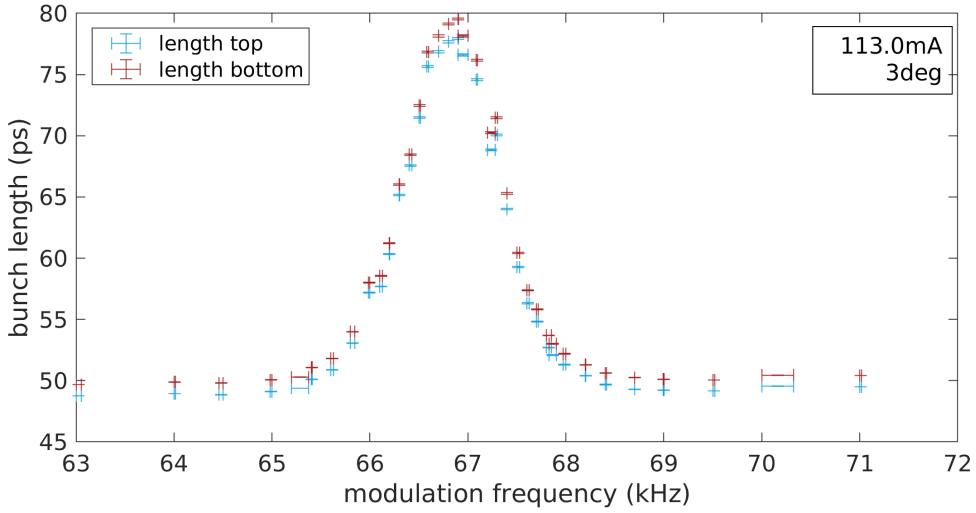

Figure 4.6.: Comparison of bunch's length for top and bottom half of the streak camera image

4.2.3. Phase modulation frequency scan

To find the best condition for the beam excitation due to PM, the parameters described in the previous section should be investigated in dependence of the excitation frequency. In Figure 4.6 this is shown exemplary for the average bunch length. Thereby the uncertainties on the parameter are given as the SEM of the 100 images times the number of slices. For the investigation of the parameter's relative change concerning the user operations mode, the parameter is divide by its value without PM, which is also called modulation factor in this work.
For the comparison between different settings of beam current or excitation amplitude, the curve has to be characterized by its peak position, maximum value, amplitude, width, and asymmetry. The curve's asymmetry disqualifies the Gaussian distribution as a fitting function. To justice, this asymmetric part, fitting with an exponentially modified Gaussian (*EMG*) distribution was evaluated but only worked for some settings quite well. Therefore and because there is also no physical motivation for an EMG distribution as well as the focus of this work is not the fit of the curve but its parameters, they are determined due to the distribution's moment.
The peak position μ and the width σ are calculated by the 1st-order raw and the 2nd-order central moment, which is previously used for the bunch shape characterization and given by the Equations (4.6) and (4.7). For the asymmetry's estimation the skewness, which is defined as the 3rd-order normalized moment $\tilde{\mu}_3$ and given by

$$\mu_3 = \frac{\sum_{i=1}^{N}(x_\mathrm{i} - \mu)^3 \cdot f(x_\mathrm{i})}{\sum_{i=1}^{N} f(x_\mathrm{i})} \tag{4.9}$$

$$\tilde{\mu}_3 = \frac{\mu_3}{\sigma^3} \tag{4.10}$$

is used. For all the parameters, which are calculated by a moment, it is necessary to subtract the offset value. This is determined here by the investigated value with turned off PM. The uncertainties of these parameters, are estimated by error propagation of all data points error.
With the calculated moments, it is not possible to estimate the peak value. Because the shape of the distribution is close to the maximum, nearly Gaussian, 4 data points are used for a fitting with a Gaussian distributed function $f(x)$. For this, the two data points left

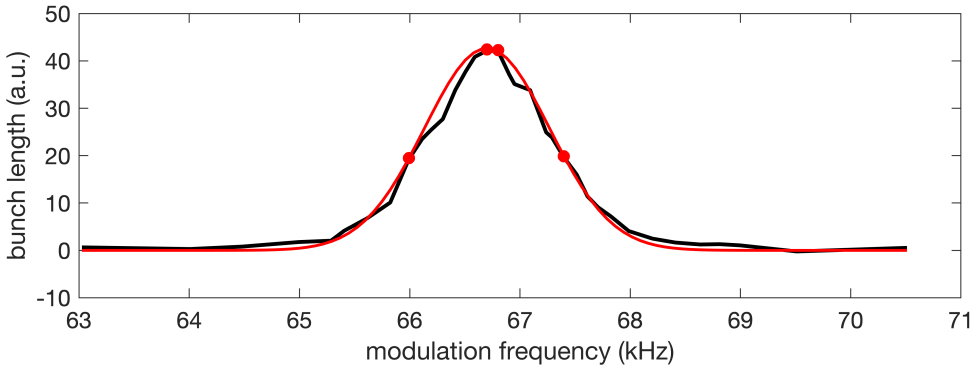

Figure 4.7.: Schematic presentation of the peak value reconstruction by a Gaussian fit with the two data points close to the resonance and the points at the edge of the FWHM.

and right from the previously calculated peak position and the respective data points at the edge of the full width at half maximum (*FWHM*) range are used, which is shown in Figure 4.7. The peak value is out of that defined as whose value at the peak position $f(\mu)$.

4.2.4. Lifetime

The total lifetime measurement is based on Equation (2.32) and is calculated from the beam current's change via

$$\tau_{\mathrm{tot}} = -I_{\mathrm{beam}}(t) \cdot \frac{\Delta t}{I_{\mathrm{beam}}(t+\Delta t) - I_{\mathrm{beam}}(t)}. \tag{4.11}$$

To suppress spikes in the lifetime by large instantaneous particle losses, the time steps are set to Δt =5 s. For a better statistics, the conditions are fixed for at least 4 min, whereby the first 30 s are not used for the lifetime measurement but to make sure, an equilibrium is reached with the set parameter, and the conditions of the previous experiment do not influence the measurement.
An investigation of the Touschek lifetime's dependency on the bunch length varied due to PM, makes an estimation of the other terms in Equation (2.33) necessary. To do that, those terms are summarized to $\tau_{\mathrm{vac.}}$, which includes all particle loss due to rest gas scattering. The theoretical value of the Touschek lifetime under the normal condition without PM is calculated from Equation (2.36) with user operation mode's α_{c} and the bunch length from the SC image projection. Because the formula is based on the assumption of Gaussian particle distribution, the bunch length is determined due to a Gaussian fitting of the total projection for 200 µs. For further analysis, $\tau_{\mathrm{vac.}}$ is kept constant under the assumption that the rest gas scattering only depends on the number of particles and is not affect by the PM.

[1] Lifetime measurement with reduced number of frequency steps

Table 4.4.: Experiments

Exp.	Amplitude (deg)	Current (mA)
1	3	104.1
		113.7
	4	50.1
2	3	84.4
		98.9
		113.1
		135.5
3	3	11.2
	5	11.1
	7	11.1
4	3	113.0
	4	93.6
		109.6
	5	105.6
5	3	65.5
		76.9
		88.2
	4	64.5
		75.8
		91.1
	5	63.6
		74.7
		89.5
6[1]	3	79.4
		106.3
		145.7
	5	104.0
7	3	107.3
		118.8
		124.3
	4	109.6
		115.3
		127.0

5. Bunch lengthening and shaping due to phase modulation

In this chapter, it is shown, how the excitation of the bunch due to phase modulation affects the bunch's length and shape for specifically chosen excitation amplitudes and frequencies at three different beam currents in the experiment at KARA.
In the first section, the high beam current situation is investigated at 124.3 mA. For that the PM's influence is discussed for an excitation frequency close to the $2f_s$ resonance as well as for a deviation of ± 500 Hz and ± 1000 Hz.
In the following the change of the bunch shape and its oscillation depending on the beam current is shown. The next section is focused on the middle-range current at about 89 mA, whereas in the last section the PM at a low current of 11.1 mA is investigated.
Because for the lower beam current configurations, higher excitation amplitudes are suitable as well, the last two sections also examine how the excitation amplitude affects the bunch shape.

5.1. High beam current

The setting with a beam current of 124.3 mA with 3° excitation amplitude is used to describe the quantitative impact of the PM in the bunch parameters, the creation and filling of subbunches and the temporal course of the bunch shape due to PM excitation. The parameters for this general description are chosen in this way because the substructures are more pronounced for higher currents. Most of the studies in this thesis use an amplitude of3°, because higher currents or amplitudes are not practicable close to the resonance frequency, which will be explained in more detail later in this chapter.
The values of a non-excited bunch used for the calculation of the PM influence discussed in this chapter are: A SC measurement for such a non-excited bunch is shown in Figure 5.1.

Excitation frequency (Hz)	σ (ps)	Bunch length oscillation amplitude (ps)	CoC oscillation amplitude (ps)
Off	47.26 ± 0.25	1.74 ± 0.02	3.37 ± 0.02

5.1.1. On resonance phase modulation

In the beginning, the bunch shape excited with a frequency close to the resonance is investigated. The resonance frequency is determined as the peak position of the detuning-curve, whose calculation is explained in detail in the next chapter, and has a value of 66 828 Hz for the (3°/124.3 mA) condition.
The measurement closest to the this resonance is taken with an excitation frequency of

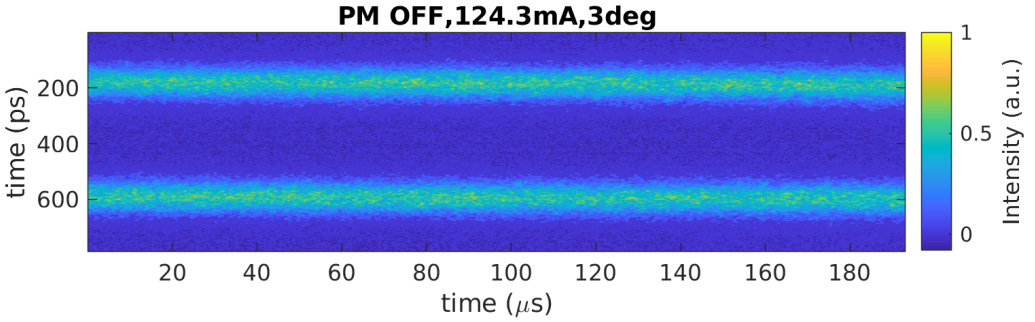

Figure 5.1.: The longitudinal bunch profile for separated odd and even bunches over a period of 200 µs at a beam current of 124.3 mA without PM is shown.

66 801 Hz, whose SC image is shown in Figure 5.2a. In this, not only a lengthening of the bunch in total but also the development of substructures can be seen clearly. Because the SC horizontal axis' timing is not synchronized with the bunch's oscillation frequency, the series of 100 images can not be averaged, so that each image has to be examined individually.
In contrast to the non-excited situation, the averaged bunch shape over the total period of 200 µs, which is displayed in Figure 5.2b, does not contain much information about the bunch length and shape at any arbitrary point in time, because of the bunch structure and periodical length oscillation. At least it can be seen that on average the number of particles far away from the peak and CoC is increased significantly.
In addition to Figure 5.2a, the SC image over a period of roughly three periods of the $2f_s$ resonance oscillation in the top row of Figure 5.3 also shows a stationary core as well as a significant number of particles moving around the CoC. In the process, the bunch splits up into 3 subbunches, from which one stays stable close to the CoC, while the other two are oscillating around the longitudinal focus. In contrast to the quadrupole motion, corresponding to lengthening and shorting in the longitudinal phase-space, the movement of the two subbunches is based on the synchrotron oscillation comply with a rotation in the phase-space. The motion in this longitudinal phase-space during PM excitation has to be investigated in further experiments.
In the bottom row of Figure 5.3, the bunch's lengthwise profile is shown for three specific positions during the periodic length and shape changing. They represent from left to right a short time range, whose bunch length is corresponding to the minimal, maximal and average total bunch length, each determined throughout approximately one $2f_s$ oscillation period.

Table 5.1.: For the (3°/124.3 mA) condition , the bunch length, its oscillation amplitude and the CoC oscillation amplitude are shown for an excitation close to the resonance $f_{res.}$ =66 828 Hz (grey) and with frequency deviations of about ±500 Hz and ±1000 Hz.

Excitation frequency (Hz)	σ (ps)	Bunch length oscillation amplitude (ps)	CoC oscillation amplitude (ps)
65823	51.92 ± 0.4	2.81 ± 0.11	4.32 ± 0.12
66300	74.48 ± 1.28	9.04 ± 0.16	7.48 ± 0.18
66802	82.33 ± 1.6	11.31 ± 0.15	12.77 ± 0.22
67290	72.8 ± 1.38	9.69 ± 0.13	12.69 ± 0.22
67825	55 ± 0.74	5.19 ± 0.12	6.69 ± 0.13

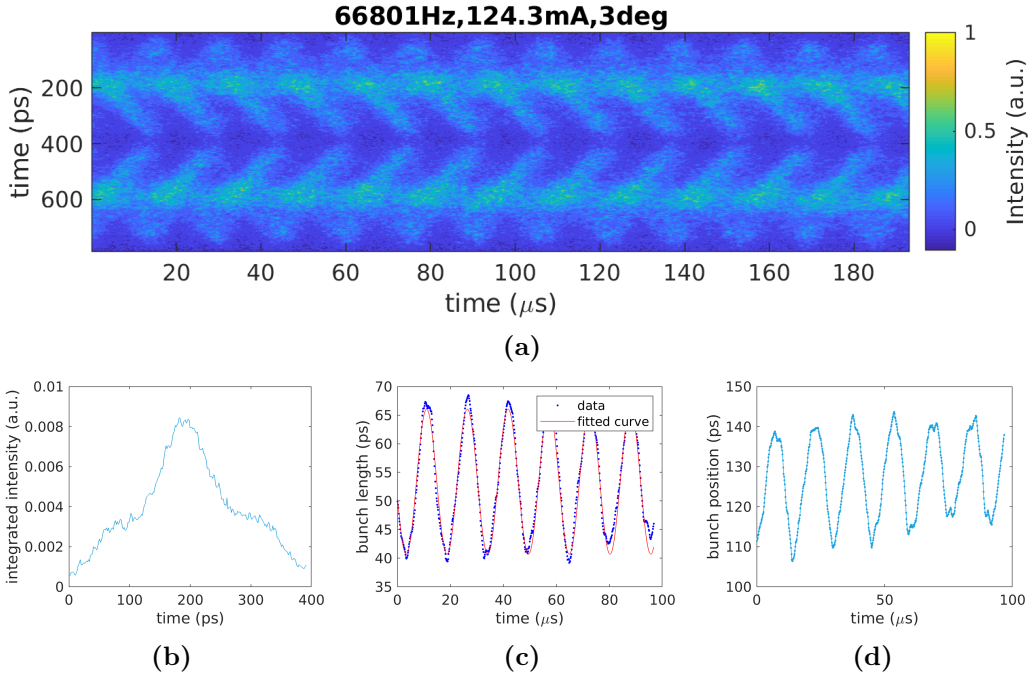

Figure 5.2.: (a) shows in the SC raw data. Visible is the time-variation of the longitudinal bunch profile caused by a PM with a frequency close to the resonance. In (b) the averaged bunch profile over 200 µs indicates a increased number of particles far away from the peak position. The temporal course of the length and CoC of the bunch is displayed in (c) and (d), where the bunch length oscillation is fitted with an sinusoidal function.

It can be seen that the two oscillating subbunches fulfill the equivalent movements with a shift of nearly 180°.

Nevertheless, a small head-tail-asymmetry is recognizable, because the width of the subbunch located at the border of the SC images is reduced. This is caused by the strong lengthening at this conditions so that no longer the entire bunch is shown on the SC image. Consequently, a detailed bunch shape analysis at such a high beam current is not suitable with the odd and even bunches on the same image. However, since the reduction due to the limited SC image is the same for both oscillating subbunches, they are completely identical. Resulting from the oscillation of the subbunches, the total bunch length reaches its minimum, if the center of charge of all three subbunches are located at the same longitudinal position. In this situation the bunch shape is close to a Gaussian distribution, which means that all subbunches look identically and they have at this point the same length, so that the minimal total bunch length is $\sigma = (71.02 \pm 0.14)$ ps (Table 5.1) and is determined by the subbunch's length. Compared with the non-exciting bunch length, the bunch is even for the minimum of the oscillation elongated by (50.3 ± 0.3) %.
The projection of the average bunch length is displayed in the bottom row's 3rd image of Figure 5.3. In this, the three subbunches are nearly separated, why the longitudinal profile has three peaks. The intensity of these three peaks is roughly the same, which is an indicator that the three parts of the bunch are filled with the same number of particles. The averaged bunch length, given in Table 5.1, is increased by (74.2 ± 0.3) % relatively to the non-excited length.
The Figures 5.2c and 5.2d illustrate the temporal oscillation of the bunch length as well as the movement of the bunch's CoC. The total bunch length's oscillation frequency is mainly determined by the subbunches' motion around the CoC, and each subbunch's individually lengthening and shortening due to the quadrupole mode motion. An investigation of each multipole order's magnitude is not possible, because of the few data points a frequency

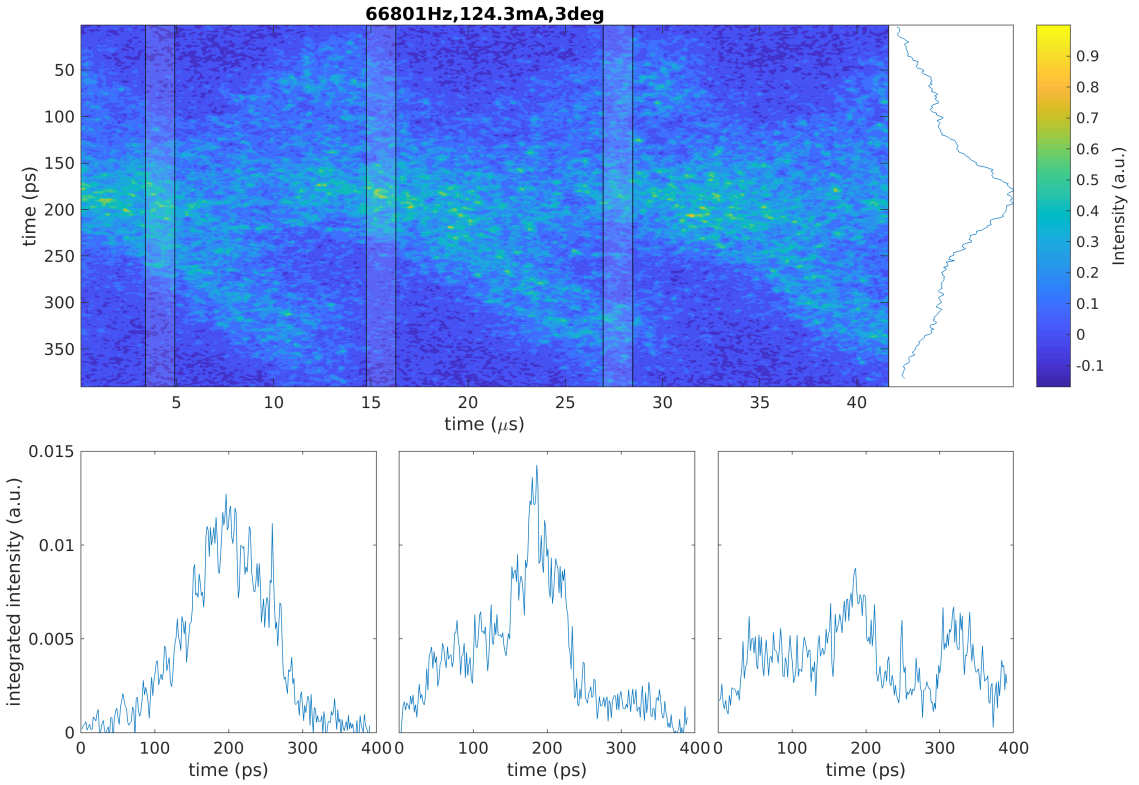

Figure 5.3.: On resonance PM excitation at (3°/124.3 mA) In the top panel, the SC raw data image with a vertical range of 400 ps, so that only one of the two bands is shown, throughout roughly three periods of the $2f_s$ resonance oscillation and its projection over the total 200 µs is shown. From left to right, the longitudinal bunch profile for minimal, maximal, and averaged bunch length are displayed in the bottom panel, which corresponds to the grey marked spots in the SC image. The shown bunch is excited with a PM frequency close to the $2f_s$ resonance with the setting (3°/124.3 mA).

analysis and peak reconstruction using FFT with a suitable resolution is not feasible. Therefore a fit with the sinusoidal function

$$a \cdot \sin(\omega t + \Phi) + c$$

is used to identify the most dominant oscillation mode. The thereby calculated oscillation frequency is f =64 991 Hz±43 Hz, which is about 2 kHz below the excitation frequency corresponding to twice the synchrotron frequency, why the most dominant mode is the second harmonic of the synchrotron frequency f_s. Even so, information about the actual value of the first and second harmonic frequency as well as their amount at the total bunch motion cannot be obtained.

On the $2f_s$ resonance, the total bunch length oscillation amplitude and the CoC oscillation amplitude are nearly the same, as seen in Table 5.1 and are increased by (550.0 ± 0.9) % respectively (278.9 ± 0.6) % relatively to the non-excited bunch, where especially the bunch length oscillation is negligible. So the oscillation amplitudes increase 3.5 to 7.5 times stronger than the actual total averaged bunch length due to PM. This is of interest because both amplitudes are a first indicator to evaluate the longitudinal bunch stability, which may influence the quality of the synchrotron radiation beam.

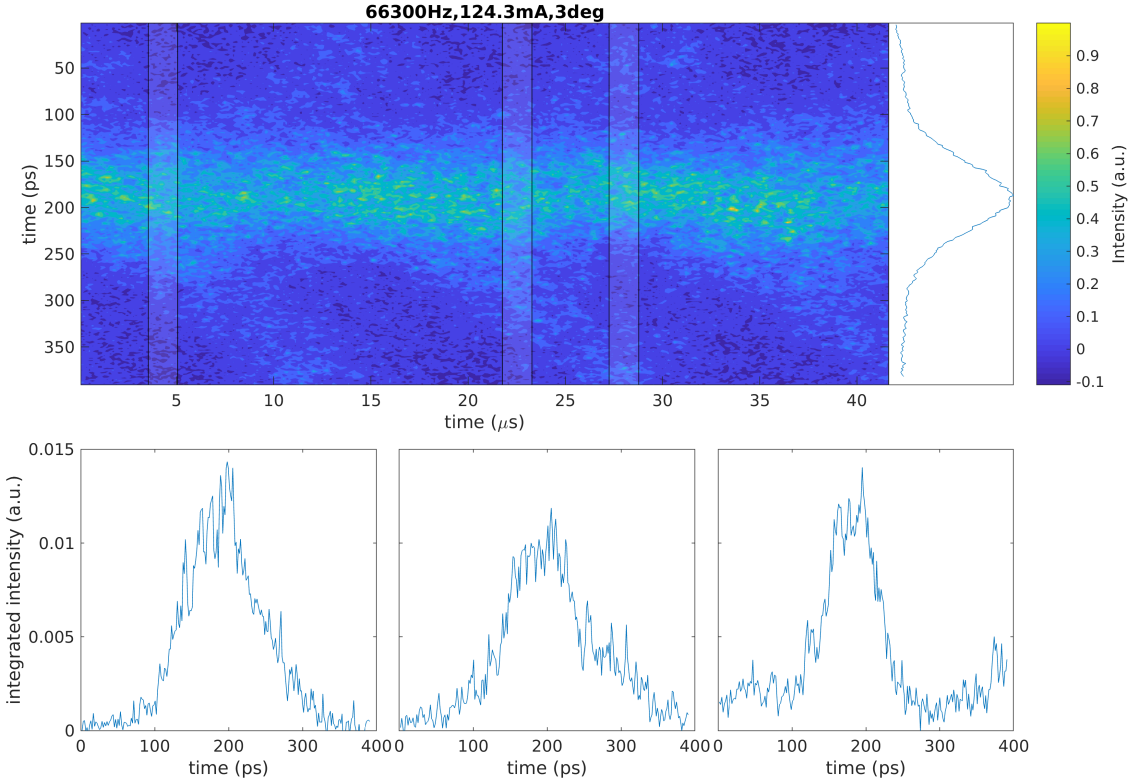

Figure 5.4.: Off resonance -500 Hz **PM excitation at** (3°/124.3 mA) In comparison with an excitation frequency close to its resonance, the most of the intensity is in the stationary core. The lengthening and shorting due to its quadrupole motion is shown in the longitudinal projection for minimal, maximal and averaged bunch length in the bottom panel.

5.1.2. Off resonance phase modulation

In this section, the impact on the bunch's shape due to PM, whose excitation frequency deviates by ±500 Hz and later by ±1000 Hz from the $2f_s$ resonance is described. The frequencies of the measurements used for this are shown in the first column of Table 5.1, in addition to the on-resonance condition.
In the Figures A.1 and A.2 the SC measurements with a frequency deviation of ±500 Hz is displayed. It can already be seen in these, that there are similarities as well as characteristic differences between the positive and negative deviation from the resonance condition. In comparison to the on-resonance, independent of the sign of deviation, the amplitude of the bunch length oscillation is significantly reduced. However, the bunch length oscillation amplitude, as well as the motion of the CoC, is significantly smaller at negative deviation for both deviation values, which is shown in Table 5.1 as well. The frequency of the bunch length oscillation, calculated as described previously, is $f = (64\,532 \pm 63)$ Hz for the negative and $f = (65\,519 \pm 54)$ Hz for the positive detuning. So the oscillation frequencies are about 2 kHz below the respective excitation frequency, which is the same as at the resonance.
For the negative deviation of −500 Hz the averaged profile over a period of 200 µs in Figure 5.4 and the SC image show a very clear and stable middle peak with low intensity side-peaks. Also, the longitudinal profiles at minimal, maximal, and average bunch length do not show significant side-peaks, which means, that for this negative detuning mostly the stationary and only marginally the oscillating subbunches are filled. Nevertheless, the total bunch length oscillates due to the quadrupole motion of this stationary bunch, whereas the synchrotron motion does not influence the total bunch length in here. This motion enlarges the bunch by (57.6 ± 0.3) %.

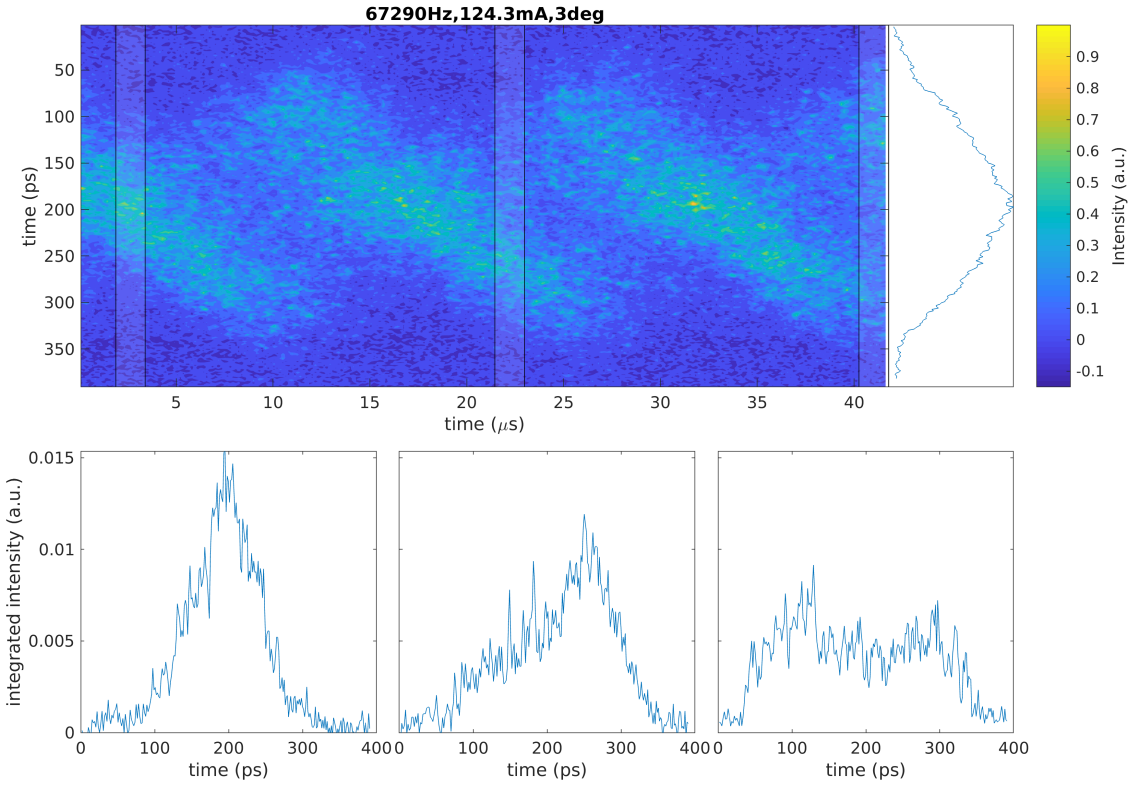

Figure 5.5.: Off resonance +500 Hz PM excitation at (3°/124.3 mA) For a positive deviation from the resonance frequency, most of the intensity is located in the both oscillating subbunches, whereas the core is nearly empty.

Even if the total bunch profile also does not show any significant side-peaks in Figure Figure 5.5, the bunch length oscillation for the positive deviation is based on a completely different mechanism. In contrast to the negative variance from the resonance frequency, in here, separated subbunches occur during the oscillation, as shown in Figures 5.5 and A.2 and the width of the averaged bunch shape is clearly increased. At points in time corresponding to the average bunch length the shape has two peaks with a local minimum of the particle's density at the CoC. This is caused by the two subbunches moving around the CoC, filled with most of the charged particles, whereas the stationary core of the bunch is nearly empty. This can be seen in the zoomed-in SC in Figure 5.5, where right after the position of maximal bunch length, the density at the CoC is nearly zero.
For negative and positive deviation from the resonance the in Section 2.5.2 described bunch shape with three respectively two filled subbunches can be seen. However, the theory predicts that for small symmetric deviations two stable solutions should be recognized. This asymmetric development of subbunches indicates that the synchrotron frequency shifts to higher values under PM, or the set excitation frequency is not the same as the modulation frequency inside the cavity. Both opportunities will be discussed again in Section 6.1.
1000 Hz deviation, both negative and positive from the $2f_s$ resonance (Figures A.3 and A.4), affects the bunch's shape in the same way as the deviation with a smaller magnitude. Independent from the deviation's sign, the total bunch length decreases with larger deviance from the resonance, illustrated in Table 5.1. Besides, the magnitude of the oscillation is so decreased that the two filled subbunches at the positive deviation are not separated at any point of the oscillation but overlap the whole time.
The total bunch length's oscillation amplitude is significantly smaller for the negative deviation. This is caused by the fact that only the magnitude of the quadrupole mode determines the bunch length for the negative deviation. In contrast, for the positive

deviation, the superposition with the synchrotron oscillation amplitude of the moving subbunches results in a still larger bunch length oscillation. Because the total averaged bunch length depends much less on the deviation's sign, the negative deviation is more interesting, why the same lengthening can be achieved with much smaller longitudinal instabilities.

5.2. Middle beam current

In the first part of this section, the shape and length with the PM parameter setting (3°/88.2 mA), will be discussed and compared with the beam excitation at higher current. The bunch length, its oscillation amplitude and the amplitude of the CoC motion are summarized for on and off resonance conditions in Table 5.2.
The SC image associated with the on-resonance frequency (66 900 Hz) is shown in Figure 5.6a. The $2f_s$ resonance frequency is increased by only 71 Hz in comparison to (3°/124.3 mA), which will be discussed more detailed in the Chapter 6. It is visible that the amplitude of the oscillation depends strongly on the beam current and is significantly reduced. The same phenomena can be seen for the averaged bunch length, which is increased by (49.6 ± 0.2) % concerning the non-excited bunch and therefore the enlarging is significantly smaller than for the (3°/124.3 mA) condition.
In the Figures A.5 and A.6 the off-resonance conditions with a deviation of ±500 Hz are illustrated, which show a nearly identically shape and oscillation behavior as the conditions discussed in the previous section at higher beam current. Nevertheless, the amplitudes of the bunch length and CoC oscillation decreased drastically, which results in an overlap of the moving subbunches and the stationary one during the whole oscillation period. Therefore a detailed discussion about the number of particles in the three different subbunches is not possible. Table 5.2 also points out, compared with Table 5.1, that the CoC motion amplitude depends much stronger on the beam current than the amplitude of bunch length oscillation.

In addition to the PM with an excitation amplitude of 3°, for this current higher amplitudes can be used to affect the bunch, because of the smaller oscillation magnitudes. In the following the excitation due to PM with the parameter setting (5°/89.5 mA) will be discussed.
In Figure 5.6b the SC data for the frequency closest to the $2f_s$ resonance (f_{res} =66 653 Hz) is displayed. In this, both odd and even bunches fill the complete range of 400 ps, which

Table 5.2.: For the (3°/88.2 mA) the bunch oscillation parameters are shown for on resonance $f_{res.}$ =66 895 Hz (grey) as well as for excitation frequencies which deviates from the resonance and without any excitation.

Excitation frequency (Hz)	σ (ps)	Bunch length oscillation amplitude (ps)	CoC oscillation amplitude (ps)
65823	50.11 ± 0.33	2.27 ± 0.09	3.77 ± 0.14
66414	58.5 ± 0.56	3.95 ± 0.15	4.21 ± 0.17
66901	71.03 ± 1.06	7.48 ± 0.32	4.93 ± 0.2
67398	60.87 ± 0.83	5.83 ± 0.22	4.31 ± 0.15
67825	50.98 ± 0.48	3.36 ± 0.15	3.73 ± 0.16
Off	47.45 ± 0.27	1.85 ± 0.01	3.42 ± 0.02

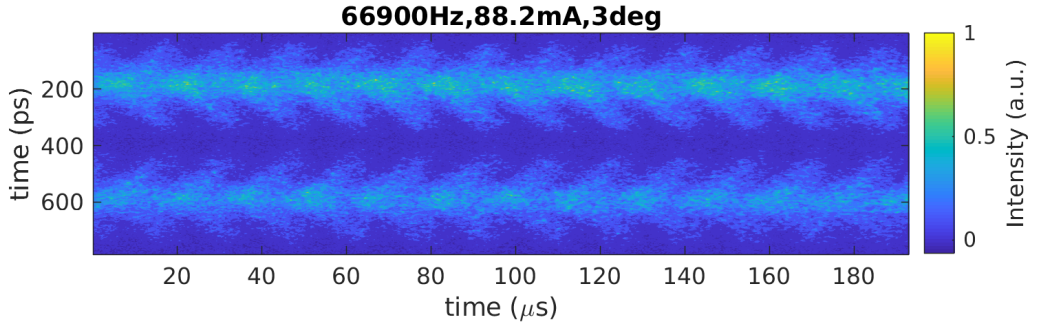

(a) (3°/90 mA)

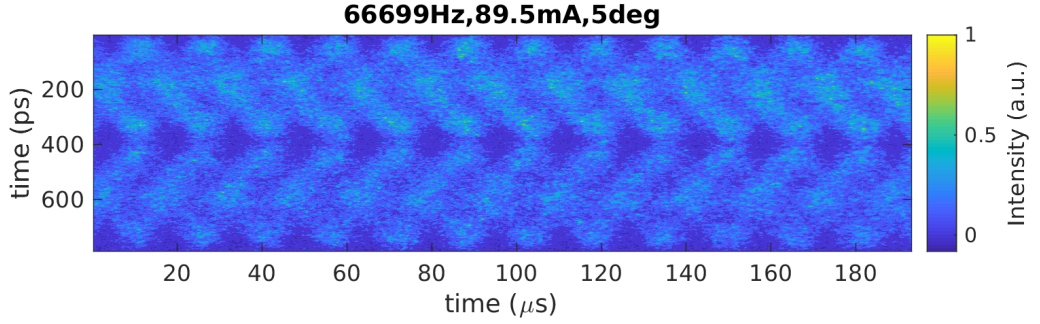

(b) (5°/90 mA)

Figure 5.6.: On resonance PM excitation at 90 mA Over a range of 200 µs the bunch shows temporal fluctuations, whose amplitude depends on the magnitude of the excitation. In both plots the excitation frequency is close to the $2f_s$ resonance frequency of the 3 deg (a) and 5 deg (b) modulation amplitude.

is available for this measurement. That is the reason, why on the one hand, this is the maximal used amplitude for this current, and on the other hand, an excitation with 5° at the resonance frequency is not practicable for systematic studies for higher beam currents and the here used filling pattern. Both limits apply because it is not possible to investigate the bunch's length and shape with the SC, which has a maximal vertical range of 800 ps since not separated, but overlapped odd and even bunches results in losing information about the bunch's shape. The larger excitation amplitude causes not only large oscillation amplitudes but also enlarges the averaged bunch length by $(109.0 \pm 0.3)\,\%$ (Table 5.3), which means a strong lengthening dependency on the excitation frequency.

The larger bunch length oscillation amplitude compared to the 3° excitation allows an analysis of the three subbunches individually because they are completely separated at special points of the oscillation period, which is displayed in Figure 5.7. The bunch profile at the moment of the average bunch length shows that the three subbunches are not filled with an equal number of particles, but the density of the moving ones is much higher than for the stationary core of the bunch. Because of the non-separated subbunches for the excitation with a 3° amplitude at the same beam current, it is not possible to say, if the different subbunches' filling of (5°/89.5 mA) and (3°/124.3 mA) depends on the beam current or the excitation amplitude. Figure B.1 shows for the on-resonance at (4°/91.1 mA), a more filled stationary bunch, which indicates that the filling depends stronger on the excitation amplitude than the current.

In comparison to the 3° on-resonance, both the bunch length's oscillation and the CoC moving amplitude are increased as well. Indeed, the CoC motion increases exactly in the same way as the bunch length, whereas the length oscillation amplitude is 1.5 times enlarged.

The off-resonance SC images for a deviation of ±500 Hz are shown in Figures A.7 and A.8 as well as their bunch profiles in Figures B.2 and B.3. In case of the positive deviation

from the resonance, similar to the high current condition, both moving subbunches are filled equally, whereas the stationary one is almost empty. In combination with the huge oscillation amplitude, this results in a periodic change between most particles close to the CoC at the minimum of the bunch length oscillation and two completely separated subbunches with a nearly zero-density region in the middle of the bunch (Figure B.3). The averaged bunch shape over multiple oscillations shows, therefore, a bunch with a homogeneous density over a wide range of nearly 200 ps.
For the detuning of −500 Hz, analog to the previously discussed excitation conditions, mainly the permanent part of the bunch is filled with electrons, while in contrast to the PM with lower excitation amplitude, the side-bunches are more filled. Nevertheless, the lengthening of the bunch is mainly determined by the quadrupole motion of the stationary subbunch. The asymmetry between the filling of the two moving subbunches and the higher particle number in the right-hand side-peak in Figure B.2 is based on the overlap of the odd and even bunches in the middle of the image because a complete separation is by virtue of the oscillation's magnitude impossible.
From Table 5.3, it becomes clear, that although the bunch length is larger for negative than for positive deviation, the magnitude of its oscillation is significantly smaller. This is independent absolute value of the deviation because only the oscillations amplitude but not the bunch's shape is influenced by the value of the deviation from the resonance frequency. In comparison to the excitation with 3° the bunch length is much stronger affected by PM far away from the resonance frequency, so that the bunch length is still increased by (38.8 ± 0.1) % for negative respectively (34.1 ± 0.2) % for the positive deviation.

5.3. Low beam current

At a total beam current of about 11 mA, the bunch length is elongated by only (40.4 ± 0.3) % even on the $2f_s$ resonance for a PM excitation's amplitude of 3°. As Figure A.9 also shows, the bunch shape oscillations are minimal. Therefore and because the backward power remains below the threshold, the bunch can be excited with an amplitude up to 7°.
The excitation with 5° amplitude shows, analogous to the previously discussed 3° phase modulation, only a smaller effect on the bunch's shape than higher current conditions, as shown in the Figures A.10 and B.4, while the average bunch length is still increased by (89.5 ± 0.4) %. However, in addition to the reduced oscillation amplitude, it shows that a larger amount of particles remain in the stationary subbunch so that the three subbunches are filled alost equally. Analogous to the on-resonance case the excitation with an off-resonance frequency affexts the bunch shape in the same way than asin the higher

Table 5.3.: For the (5°/89.5 mA) the bunch oscillation parameters are shown for on resonance $f_{\text{res.}}$ =66 653 Hz (grey) as well as for excitation frequencies which deviates from the resonance and without any excitation.

Excitation frequency (Hz)	σ (ps)	Bunch length oscillation amplitude (ps)	CoC oscillation amplitude (ps)
65614	65.88 ± 0.67	4.71 ± 0.15	3.8 ± 0.16
66113	93 ± 1.72	12.11 ± 0.28	6.02 ± 0.25
66700	99.17 ± 2.03	14.35 ± 0.43	6.86 ± 0.27
67092	89.01 ± 1.82	12.83 ± 0.33	6.11 ± 0.24
67612	63.62 ± 1.02	7.15 ± 0.21	4.3 ± 0.16
Off	47.45 ± 0.25	1.68 ± 0.01	3.4 ± 0.02

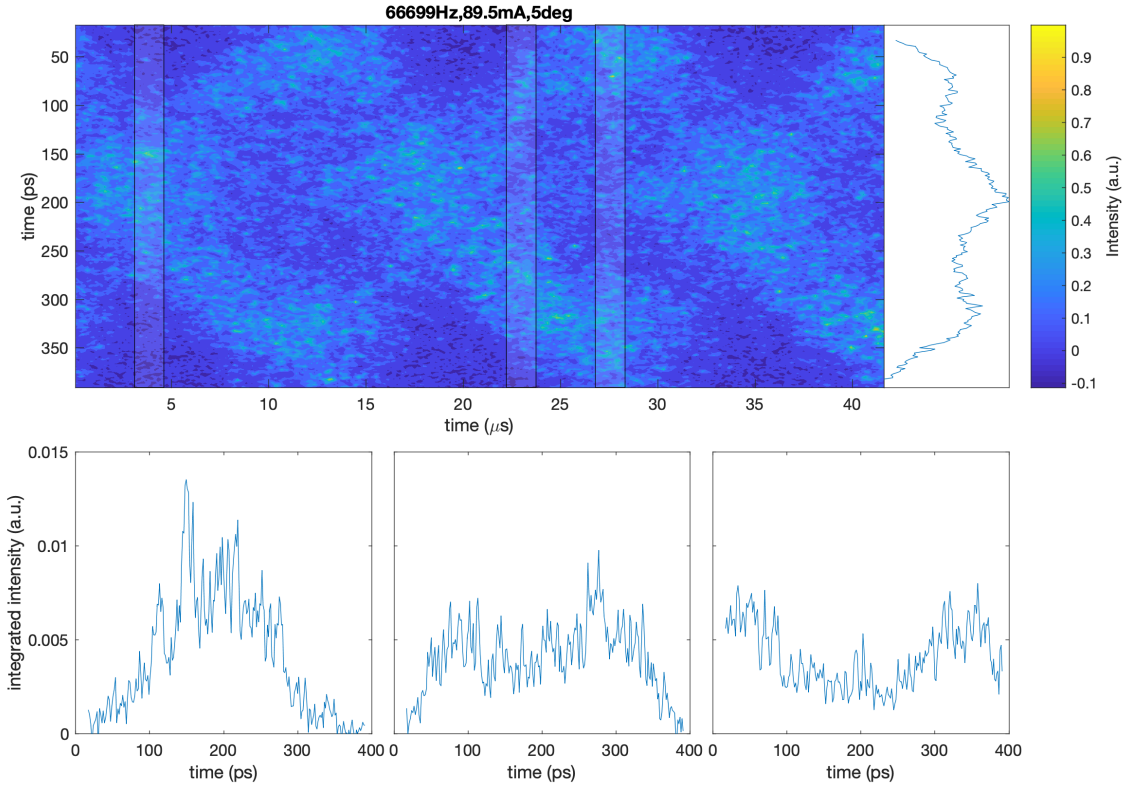

Figure 5.7.: On resonance PM excitation at (5°/89.5 mA) With a higher excitation amplitude the subbunches are completely separated at special points, so that the core is empty surrounded by two moving subbunches.

current condition, described previously. However, the value of all the discussed parameter (Table 5.4) are reduced.

The PM configuration (7°/11.1 mA) close to the resonance, displayed in the Figures 5.8 and A.11, clarifies the strong bunch's shape and lengthening dependency on the excitation amplitude as well. The strong excitation results in a huge oscillation amplitude of both moving subbunches therefore the separation of the three subbunches is much more pronounced than for the 5° or even 3° PM amplitude. Therefore the average bunch length is, even for this low beam current, increased by $(143.6 \pm 0.5)\,\%$, which is the largest bunch lengthening for all investigated settings. For a frequency deviation from resonance frequency, the bunch shape, and subbunches' filling is the same as described in the previous sections, whereby in general the moving subbunches are filled with more particles than for the lower excitation amplitudes (Figures B.5 and B.6).

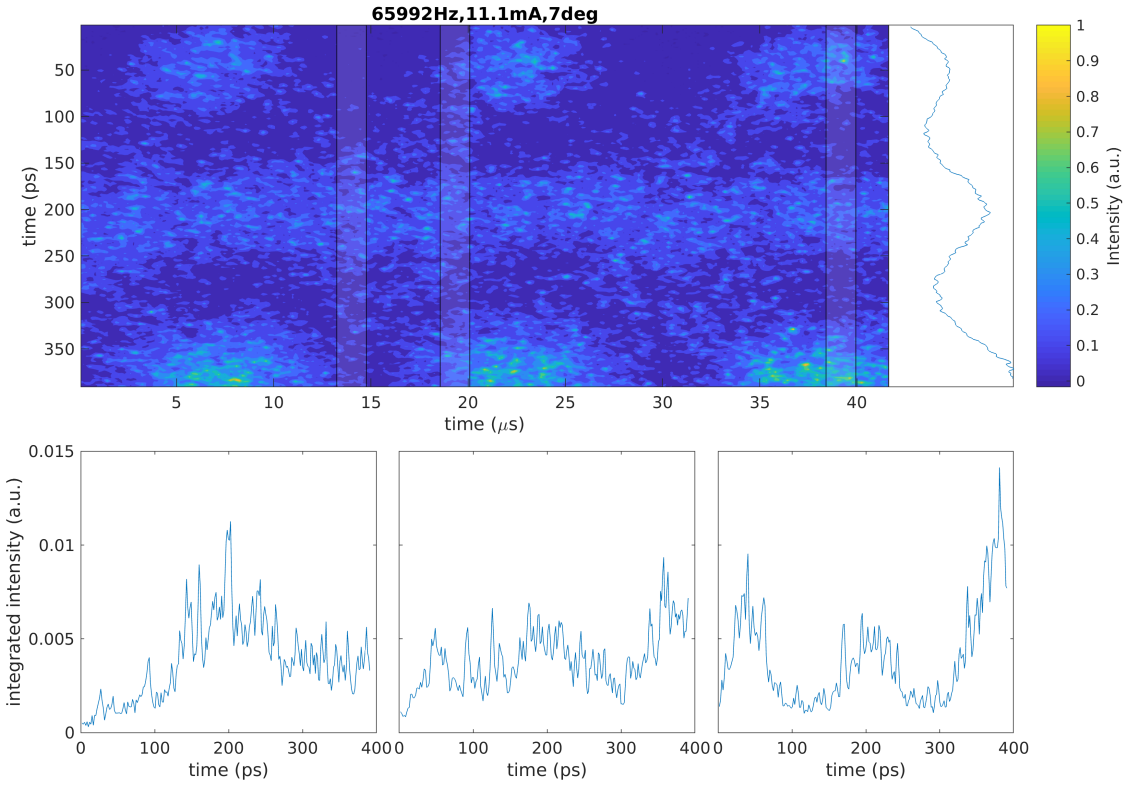

Figure 5.8.: On resonance PM excitation at (7°/11.1 mA) Even at this low current, the 7° excitation separates the subbunches stronger than at all other condition investigated in this work, as illustrated in the SC raw data in the top panel as well as in the average bunch projection in the left corner of the bottom panel.

Table 5.4.: For the (5°/11.1 mA) the bunch oscillation parameters are shown for on resonance $f_{\text{res.}}$ =66 782 Hz (grey) as well as for excitation frequencies which deviates from the resonance and without any excitation.

Excitation frequency (Hz)	σ (ps)	Bunch length oscillation amplitude (ps)	CoC oscillation amplitude (ps)
65823	59.47 ± 0.32	2.13 ± 0.09	3.19 ± 0.16
66414	81.22 ± 0.56	3.89 ± 0.1	4.23 ± 0.17
66790	86.32 ± 0.63	4.36 ± 0.18	6.11 ± 0.9
66950	83.76 ± 0.61	4.26 ± 0.09	5.93 ± 0.16
67825	53.15 ± 0.31	2.03 ± 0.16	4.01 ± 0.22
Off	45.55 ± 0.24	1.52 ± 0	3.36 ± 0.02

Table 5.5.: For the (7°/11.1 mA) setting the bunch oscillation parameters are shown for on resonance $f_{\text{res.}}$ =66 408 Hz (grey) as well as for excitation frequencies which deviates from the resonance and without any excitation.

Excitation frequency (Hz)	σ (ps)	Bunch length oscillation amplitude (ps)	CoC oscillation amplitude (ps)
64990	54.81 ± 0.26	1.72 ± 0.06	3.29 ± 0.16
65504	74.51 ± 0.47	3.26 ± 0.12	3.16 ± 0.15
65992	110.94 ± 0.87	6.06 ± 0.15	6.96 ± 0.29
66507	107.76 ± 0.85	5.96 ± 0.23	8.16 ± 0.38
66950	89.9 ± 0.7	4.84 ± 0.13	7.15 ± 0.23
Off	45.55 ± 0.24	1.52 ± 0	3.36 ± 0.02

6. Phase modulation frequency scan

After the analysis of the influence on the longitudinal bunch shape due to phase modulation (*PM*), in this chapter, the frequency dependence of the average bunch length and its oscillation amplitude will be discussed. For this purpose, the frequency detuning curve is introduced, and its parameters are described in the first section. In the following two sections, the dependence of the detuning curve's parameters as the resonance frequency on the beam current, respectively, the PM modulation amplitude is explained. Additionally, a stable beam criterion is defined, whose dependency on the PM parameters is discussed, too.

6.1. Phase modulation frequency dependence

In this, the configuration (5°/89.5 mA), whose characteristic excitation frequencies are explained in the previous chapter, is used to describe the shape and characteristics of the frequency detuning curve in principle.
As discussed previously, the magnitude of the average bunch length elongation is strongly affected by the PM excitation frequency, which is illustrated in Figure 6.1. This detuning curve shows that the bunch lengthening due to PM is most effective near the resonance, which is determined by $(66\,650 \pm 80)$ Hz (Table 6.1). Because the maximal averaged bunch length is very close to the discussed one for the actual measured point close to the resonance. Also, the shape of the bunch under this condition, described in detail in Section 5.2, is valid for the exact resonance condition. Nevertheless, the slightly stronger lengthening results in a maximal bunch elongation by (112.4 ± 0.2) %.
In a range of about ±1 kHz around the resonance, the lengthening of the bunch is nearly symmetric, whereas further away from this resonance, stronger asymmetries occur. This asymmetry results from the gradual slope on the negative detuning flank in opposite to the positive flank, so that the PM affects the bunch length up to larger frequency deviation for the positive detuning than for the negative one. This detuning curve shape agrees with the theoretical prediction in Equation (2.60) and the simulation results for the KARA storage ring parameters in [34]. On both directions of the detuning, in the plateau region, where a change of the excitation frequency does not have an impact on the average bunch

Table 6.1.: Detuning curve parameters for bunch length and bunch length oscillation as well as CoC oscillation curve for (5°/89.5 mA) condition. The resonance frequency $f_{\max}$ is identical for the three detuning curves but the amplitude and the skewness $\tilde{\mu}_3$ is different for the three curves.

	$f_{\max}$ (Hz)	$\sigma_{\text{detun.}}$ (Hz)	$\sigma_{\max}$ (ps)	$\sigma_{\max} - \sigma_0$ (ps)	$\tilde{\mu}_3$
bunch length	66650 ± 80	629.6 ± 13	100.8 ± 0.4	53.4 ± 0.4	0.23 ± 0.106
bunch length oscillation	66790 ± 80	634.6 ± 13.6	18.2 ± 0.1	15.2 ± 0.1	0.534 ± 0.164
position oscillation	66640 ± 210	960.9 ± 29	9.4 ± 0	5.6 ± 0	-0.548 ± 0.213

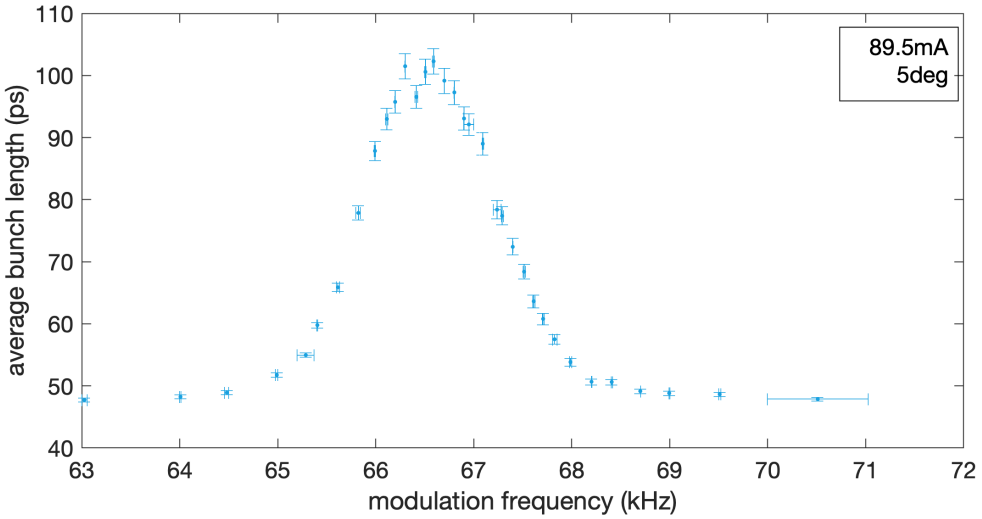

Figure 6.1.: Bunch length detuning curve for (5°/89.5 mA) The averaged bunch length is determined over range of modulation frequencies. The resulting detuning curve, shows a maximum at its resonance frequency. The characteristic of this curve can be described by the bunch length at the resonance, the width of the curve and its asymmetry, which denotes a right-tailed detuning curve in here.

length, the bunch length is not increased in comparison with the non-excited bunch length $\sigma = (47.45 \pm 0.04)$ ps.
The positive skewness that denotes a right-tailed detuning curve is, besides the width of the curve, an additional parameter to describe the detuning curve's shape. Both parameters are given in Table 6.1, whereby they are primarily needed in the following, for the comparison of different parameter configurations.
As mentioned previously in Section 4.1.2, the synchrotron frequency $f_s = (32\,611 \pm 535)$ Hz can only be measured with a great uncertainty. In Figure 6.2 the bunch length detuning curve concerning $2f_s$ is shown, in which the error bar is dominated by the coherent synchrotron frequency's uncertainty. Therefore no clear statement about the deviation of the resonance regarding twice the synchrotron frequency ($\mu = (1431 \pm 610)$ Hz) is possible, where at least, a positive deviation can be seen. The sign of this deviation is in contradiction with the theory in Section 2.5.2 based on [15, 34], which predict a negative deviation because of the much larger separatrix for an excitation frequency below $2f_s$ and the shift of the synchrotron frequency due to the non-linearity of the particles motion, which can be described by a harmonic oscillator. For the here used excitation amplitudes, the motion has non-linearity, which tends to a decreasing of the oscillation period and so increases the synchrotron oscillation, why the resonance is shifted to negative deviation.
For a more accurate determination of this resonance deviation, it is necessary to measure the synchrotron frequency more precisely in further experiments. In this process, it has to be taken into account, that the incoherent synchrotron frequency deviates from the here measured coherent synchrotron frequency and may be influenced by the PM. Besides that, it must be checked whether the set value of the excitation frequency is the same as the PM frequency inside the cavity, by doing a RF spectrum analysis and determining the sidepeaks.

Figure 6.3 plots in addition to the relative bunch lengthening also the detuning curves of the bunch length oscillation amplitude and CoC oscillation amplitude modulation factor. For the oscillation amplitude of the bunch length, the detuning curve has the same width and resonance frequency as the bunch length itself, which is shown in Table 6.1. Nevertheless, there are characteristic differences, from which the much stronger amplitude is the

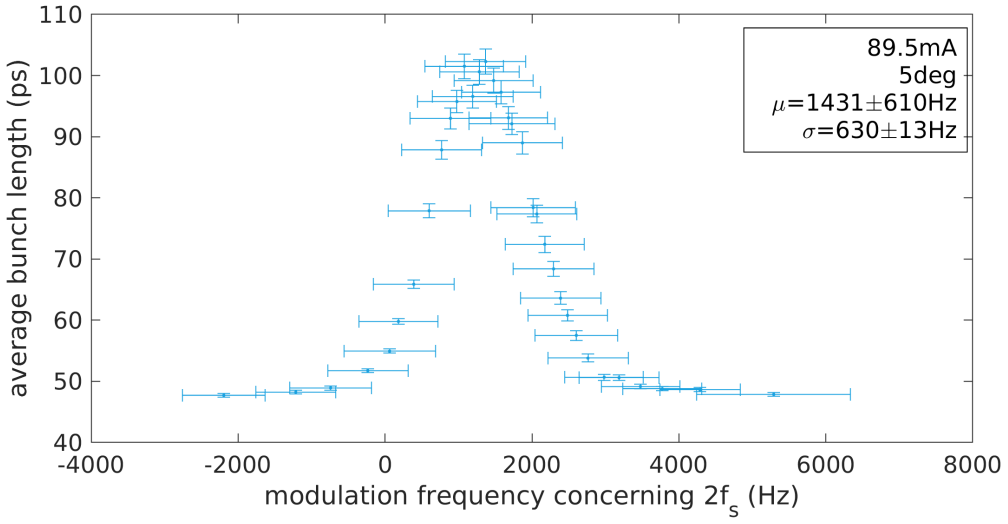

Figure 6.2.: Bunch length detuning curve for $(5°/89.5\,\mathrm{mA})$ **concerning** $2f_\mathrm{s}$ In this the averaged bunch length as in Figure 6.1 is shown. On the horizontal axis, the deviation from twice the synchrotron frequency f_s=$(32\,611 \pm 535)\,\mathrm{Hz}$ is plotted. The error bars are dominated by the coherent synchrotron frequency's uncertainty.

obvious and most important one. Because such a strong length oscillation possibly affects the radiation beam quality, further experiments on the radiation quality during PM are necessary. Moreover, it is needful for the bunch lengthening due to PM in normal user operation to define a stability criterion for the radiation beam in cooperation with the radiation users.
For this work the stability parameter Γ is defined as the ratio between the relative bunch lengthening $\frac{\sigma}{\sigma_0}$ and the relative bunch length oscillation amplitude $\frac{\delta\sigma}{\delta\sigma_0}$. In here the stability criteria is fulfilled for

$$\Gamma = \frac{\frac{\sigma}{\sigma_0}}{\frac{\delta\sigma}{\delta\sigma_0}} > 0.5 \tag{6.1}$$

In the bottom panel of Figure 6.4, the parameter Γ in dependency of the excitation frequency is shown, which clarifies that the instability increases with a shorter deviation from the resonance frequency. For the configuration $(5°/89.5\,\mathrm{mA})$, the limit frequencies for the stable range are 65 992 Hz, and 67 987 Hz or rather deviate -661 Hz and 1334 Hz from the resonance frequency, which shows up a clear asymmetry. They are determined by linear interpolation of Γ between the two data points next to $\Gamma = 0.5$. Corresponding to those frequencies the bunch can be enlarged by $(87.8 \pm 0.1)\,\mathrm{ps}$ for the negative respectively $(53.8 \pm 0.1)\,\mathrm{ps}$ for the positive flank, so the bunch lengthening is $(63.2 \pm 0.3)\,\%$ larger for the negative limit frequency. This follows from the differences in the shape of the bunch length and its oscillation amplitude detuning curve, which has a more than two times stronger asymmetry. Consequently, the oscillation amplitude influencing by the PM on the negative detuning flank becomes effective at higher frequencies than the bunch lengthening, as shown in Figure 6.4, so that the stability criterion is fulfilled up to stronger enlarged bunches than on the positive detuning flank.

In contrast to the length oscillation amplitude, the relative CoC oscillation amplitude is affected by the PM in almost the same way as the bunch length, which is shown in Figure 6.3. The significant differences in width and skewness (Table 6.1) occur because of an additional increase after reaching the minimum at about 65 500 Hz and 69 000 Hz, which corresponds with the transition to the plateau of the quadrupole motion.

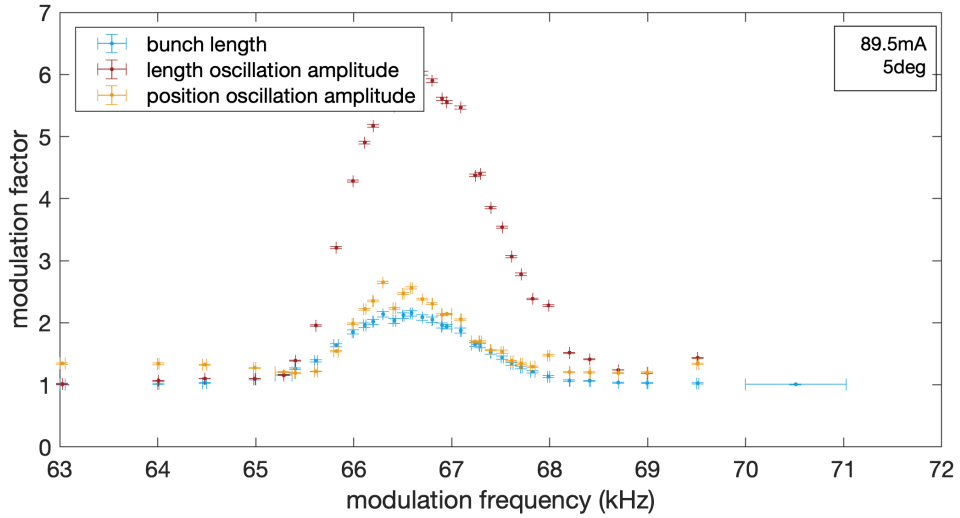

Figure 6.3.: Beside the detuning curve of the bunch length, the curves of the bunch length oscillation amplitude and the CoC oscillation amplitude are plotted. For the comparison of these three detuning curves, they are divided by the respective value without PM excitation, which is called modulation factor. It can be seen, that the relative length oscillation amplitude is increased about two times stronger than the bunch length itself at the PM resonance, whereby the resonance frequency is identical for all three curves.

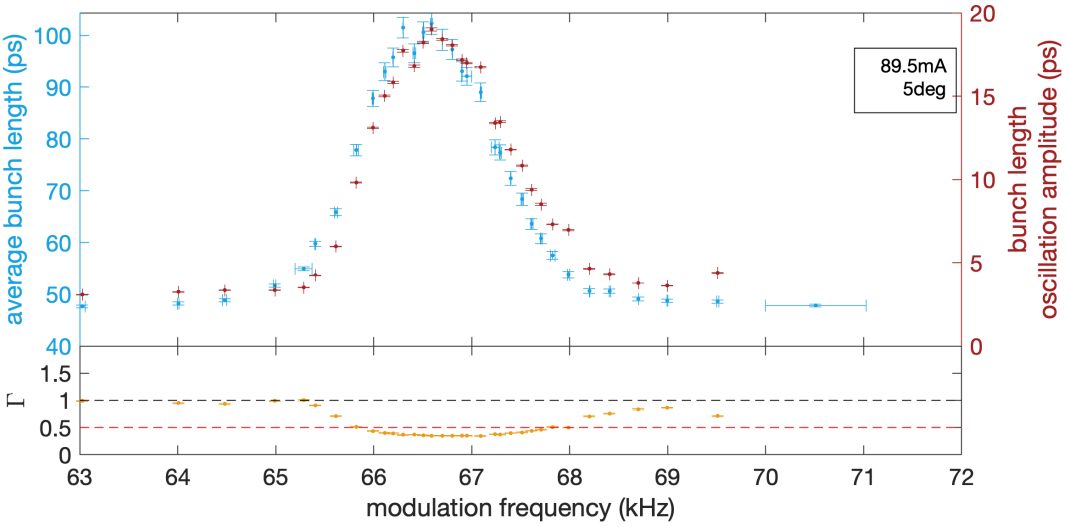

Figure 6.4.: Bunch instability due to PM for (5°/89.5 mA) On the left vertical axis (blue), the absolute average bunch length is plotted, whereas the right side shows its oscillation amplitude (red). The stability factor Γ, which is plotted in the bottom panel and defined by Equation (6.1), describes the ratio between the length and its oscillation amplitude increasing. In here the bunch is defined as stable, if $\Gamma > 0.5$, which is marked by the dotted red line.

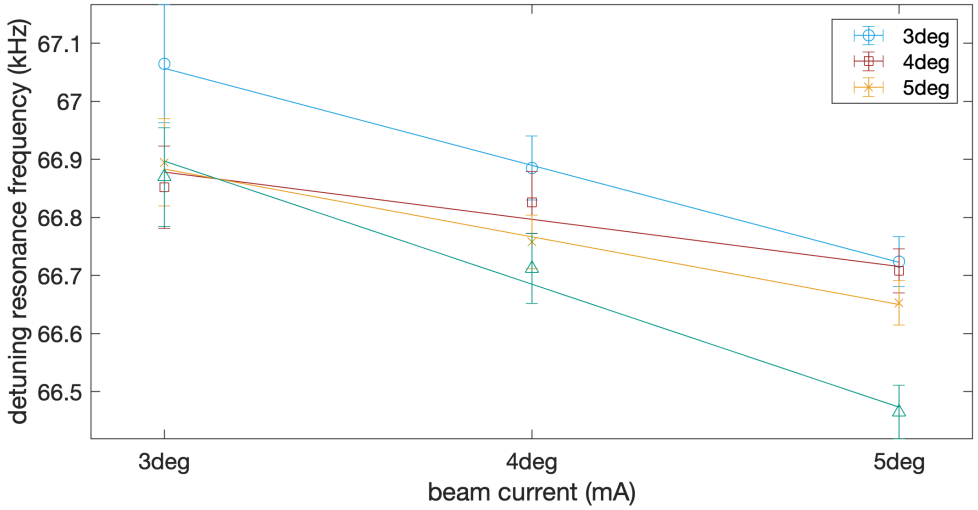

Figure 6.5.: Resonance frequency of the bunch length detuning curve over the beam current for different PM amplitudes. The linear fits show, that the resonance frequency decreases with the beam current.

Close to the resonance the synchrotron oscillation motion is much smaller than the bunch length oscillation amplitude, why the CoC motion is overlaid and determined by the quadrupole motion. In frequency regions in which the length oscillation is small, the CoC motion due to the synchrotron oscillation becomes dominant and is still $(29 \pm 2)\,\%$ and therefore significantly larger than without PM.

6.2. Current dependence of the PM detuning curve

The bunch lengthening due to PM depends not only on the excitation frequency but also on the beam current. A crowd of average bunch length detuning curves for multiple beam currents is shown in Figure 6.7 for different excitation amplitudes.
Over a wide current range from 65 mA to 125 mA, the resonance frequency decreases minimally, whereby the shift increases with the excitation amplitude. The direction of this shift agrees with the theoretical prediction in Section 2.5.1, based on the tune shift from the potential distortion model. This results in a deceasing of the absolute value of the synchrotron frequency second harmonics $2f_s$ with increasing beam intensity. In addition beam loading effects can reduce the effective cavity voltage, which also results in a shift of the synchrotron frequency. However, Table 6.2 shows a very large statistical uncertainty on the resonance frequency, which is of the same order of magnitude as the shift over a range

Table 6.2.: Bunch length detuning curve parameters for modulation amplitude of 3 deg at different beam currents.

mod. Amplitude	current (mA)	$f_{\max}$ (Hz)	$\sigma_{\text{detun.}}$ (Hz)	$\sigma_{\max}$ (ps)
3deg	65.5mA	67070 ± 200	205.4 ± 93.7	67 ± 0
3deg	76.9mA	66850 ± 140	796.4 ± 17.4	69.4 ± 0.4
3deg	88.2mA	66900 ± 150	562.8 ± 23.7	70.7 ± 0.1
3deg	107.3mA	66770 ± 100	507.7 ± 18.6	81.9 ± 0.3
3deg	113.0mA	66870 ± 170	607.2 ± 24.3	78.4 ± 0
3deg	118.8mA	66750 ± 90	548 ± 15.5	84.4 ± 0.2
3deg	124.3mA	66830 ± 100	519 ± 17.1	83 ± 0.3

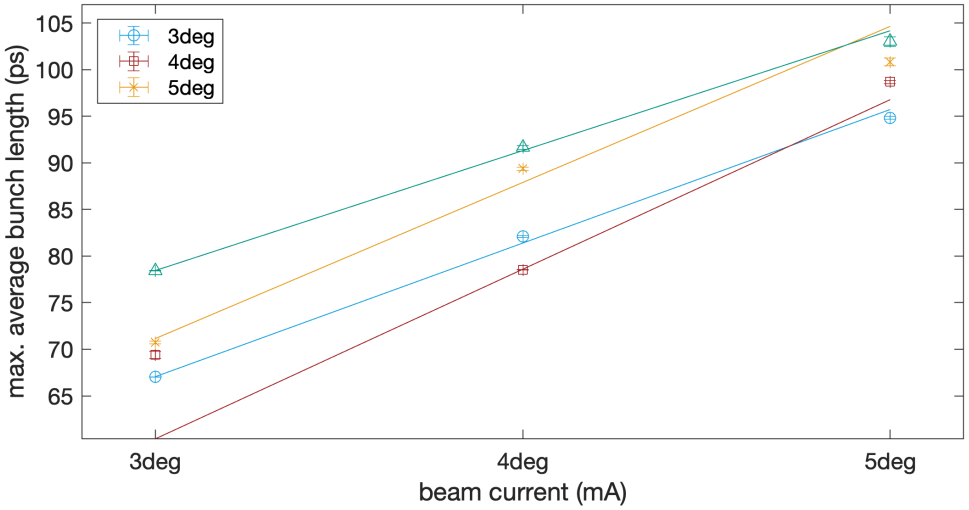

Figure 6.6.: Average bunch length at the resonance over the beam current. With higher beam current, the bunch becomes more extended. For the PM amplitudes 4 deg and 5 deg, the lengthening reaches a saturation, so that a linear fitting is only possible for the 3 deg excitation.

of 30 mA to 40 mA, so that the linear fitting in Figure 6.5 only points out a tendency.
In contrast to the resonance frequency, the maximal average bunch length due to PM, increases clearly, as shown for 3 deg excitation in Figure 6.7a for a range of about 60 mA. The nearly linear correlation is fitted in Figure 6.6 by

$$\sigma_{max} = m \cdot I + \sigma_0 \tag{6.2}$$

with the parameter values $m = (0.32 \pm 0.03)\,\frac{\text{ps}}{\text{mA}}$ and $\sigma_0 = (46.3 \pm 3.4)\,\text{ps}$. According to Equation (2.47), the driving term of the PM depends directly on $\epsilon \sim \cot \Psi_s$. So beam loading effects inside the RF cavities, which increase with the beam charge and current, can change the synchronous phase temporally and effect the parameter ϵ and therefore the magnitude of the lengthening effectively.
In comparison, the detuning curve crowd for an excitation amplitude of 5 deg (Figure 6.7c) only the resonance frequency is shifted, whereby the lengthening saturates and does not have a significant current dependency. This saturation can come from an over-excitation, because of the high excitation amplitude at which non-linear beam dynamic effects become dominant. Alternatively this saturation is based on the limitation of the streak camera range, why additional experiments with only one band in the SC image range are necessary.

Table 6.3.: Bunch length oscillation detuning curve parameters for modulation amplitude of 3 deg at different beam currents.

mod. Amplitude	current (mA)	f_{max} (Hz)	$\sigma_{\text{detun.}}$ (Hz)	σ_{max} (ps)
3deg	65.5mA	66950 ± 240	746.5 ± 32.9	9.79 ± 0.45
3deg	76.9mA	67110 ± 170	406.2 ± 37.3	8.78 ± 0.01
3deg	88.2mA	67060 ± 150	600.6 ± 24.4	9.89 ± 0.01
3deg	107.3mA	66850 ± 370	473.2 ± 78.2	13.74 ± 0.22
3deg	113.0mA	66970 ± 80	516.8 ± 14.3	11.26 ± 0.05
3deg	118.8mA	66820 ± 180	665.1 ± 25.9	14.72 ± 0.08
3deg	124.3mA	66900 ± 130	567 ± 21	13.8 ± 0.01

Besides the resonance frequency and the maximal averaged bunch length, also the shape of the detuning curves is affected by the actual beam current. Independent from the excitation amplitude, the flank of the positive deviation from the resonance does not depend strongly on the beam current. RF phase modulation influences the bunch length, for all beam currents, up to a deviation of about 2 kHz above the resonance frequency. Till close to the respective resonance frequency, where the lengthening reaches its maximum, this flank does not have any beam current dependency, why the lengthening amplitude and the resonance frequency have the same current dependence.
This current independent behavior for the positive detuning requires systematic differences in the negative detuning flank. The Figures 6.7a to 6.7c show, that the bottom end of the range, in which the PM elongates the bunch, shifts to lower frequencies for higher beam current, so that the detuning curve becomes more symmetric for higher beam current condition.

The bunch length oscillation amplitude detuning curves, are plotted in Figure 6.8 for different excitation amplitudes. These show nearly the same current dependency for the resonance frequency as the bunch length itself (Table 6.3). However, it turns out, that the amplitude of the bunch length oscillation increases about twice as strong as the bunch length from 65.5 mA to 124.3 mA for the 3 deg excitation, so that the instability increases for the PM at higher beam current.
Because, for the most investigated configuration, but especially the beam current region of the user operation, the stability criteria $\Gamma > 0.5$ is not fulfilled at the resonance, so limit frequencies on both sides of the resonance frequency exists. These limit frequencies and the corresponding bunch length are discussed in the following. In Figure 6.9, the correlation between the beam current and the borderline frequency below the resonance is shown for different excitation amplitudes, whereby for a beam current of 11 mA, the stability criteria is fulfilled even at the resonance, for all amplitudes. In this, a linear correlation and an excitation amplitude dependency can be seen, which is analogous to the shift of the resonance frequency between different excitation amplitudes. In addition to the lower borderline frequency, Figure 6.10 shows the upper limit frequency as well, for which the correlation is linear, too.
The intersection point of the two linear fits for the upper and lower borderline frequency of the instability regions defines the maximum beam current that fulfills the stability criteria for all PM excitation frequencies. They are determined as

3 deg	4 deg	5 deg
(42.0 ± 6.5) mA	(41.0 ± 9.2) mA	(21.1 ± 22.8) mA

The large uncertainty for the 5 deg excitation amplitude results primarily from the only 4 data points for both fittings. It still shows that an unstable region around the resonance occurs far below the normal user operation, so that the off-resonance condition is of great interest.

The average bunch length belonging to the lower borderline frequency is plotted in the Figure 6.11. In contrast to higher excitation amplitudes, the current has almost no influence on the bunch length at the edge of the stable bunch region for a PM excitation with an amplitude of 3 deg, at least up to 100 mA. However, there is an overall increasing trend with a higher beam current. The stronger excitation due to higher PM amplitudes creates much stronger instabilities, so that the stable excitation region moves further away from the resonance frequency, why the lengthening in there is not that strong.

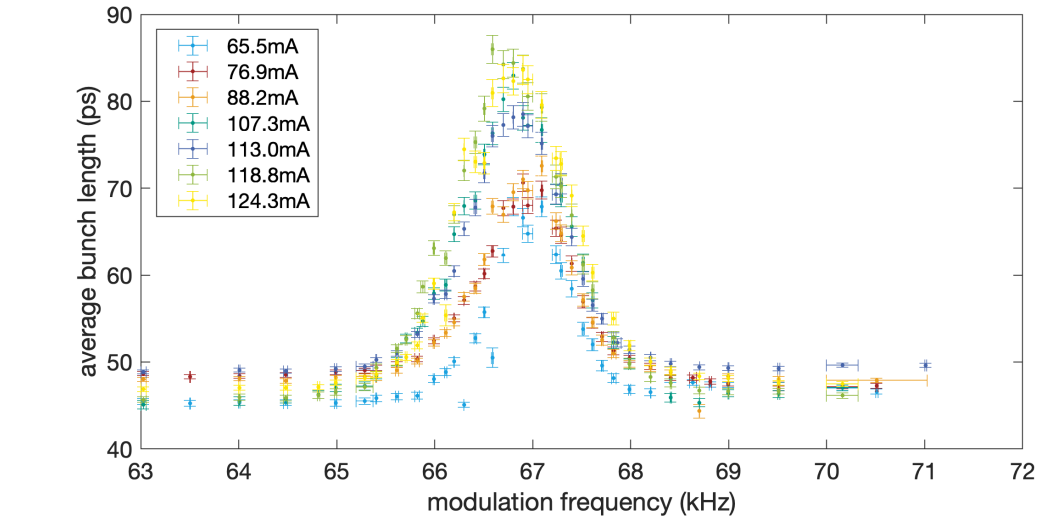

(a) 3 deg

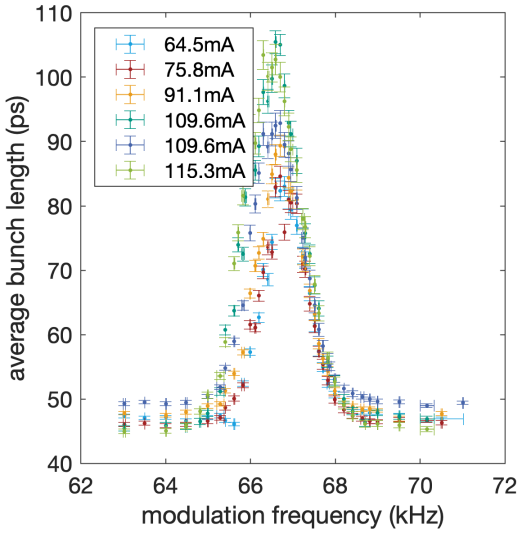

(b) 4 deg

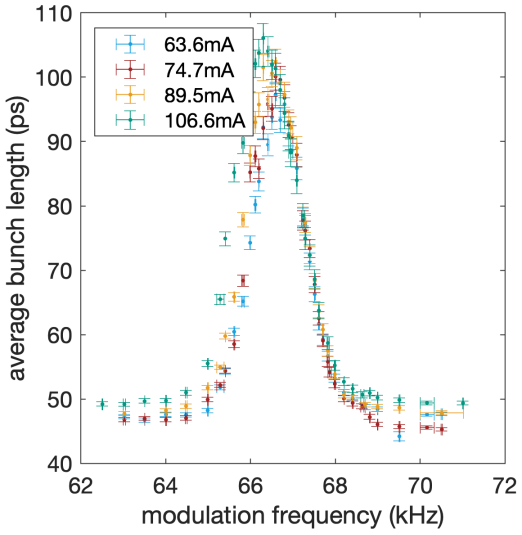

(c) 5 deg

Figure 6.7.: Average bunch length detuning curves at different beam currents with the same PM amplitude. The resonance of the detuning curve shifts to smaller modulation frequencies for higher beam currents. Also the lengthening due to PM increases with the current, independent on the modulation amplitude.

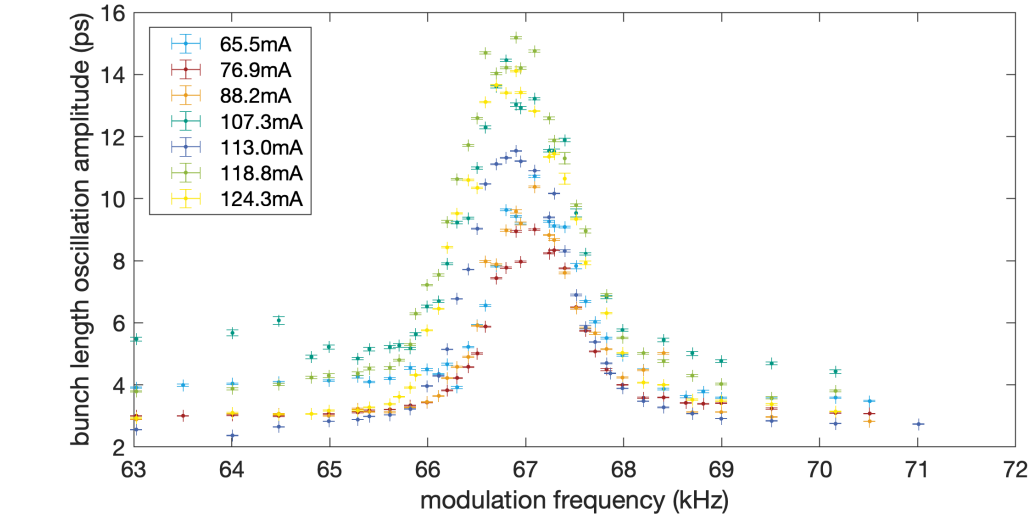

(a) 3 deg

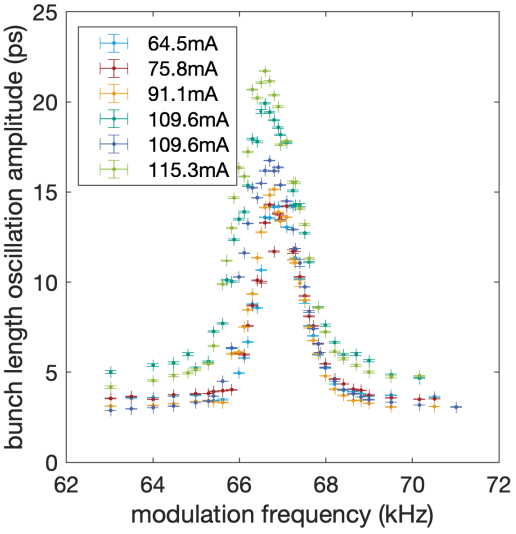

(b) 4 deg

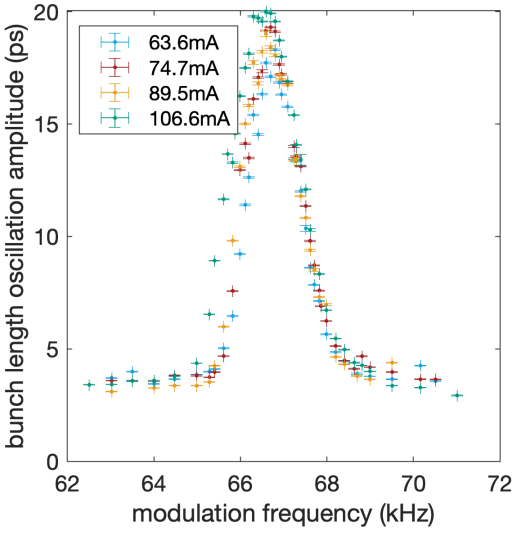

(c) 5 deg

Figure 6.8.: Bunch length oscillation amplitude detuning curves at different beam currents with the same PM amplitude. The shift of the resonance frequency is identical as for the bunch length detuning curves in Figure 6.7.

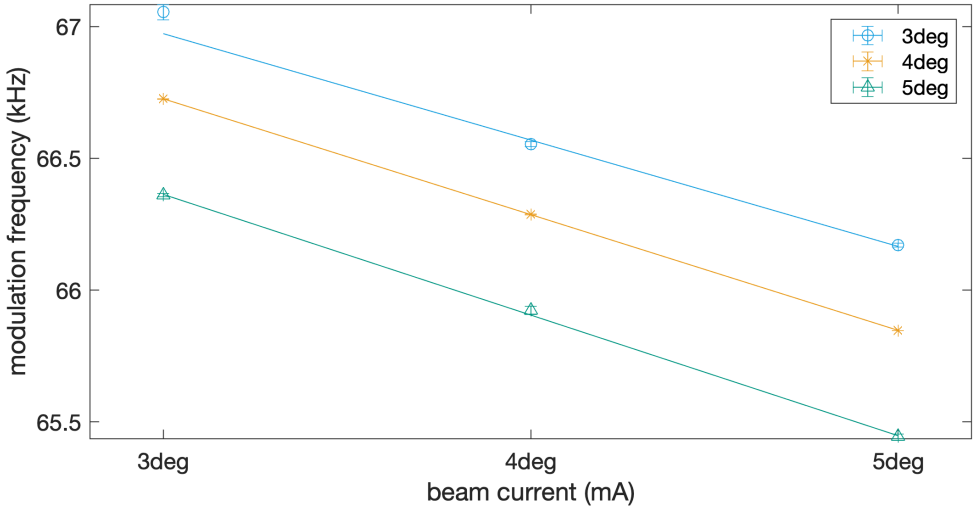

Figure 6.9.: Limit modulation frequency, that fulfills $\Gamma > 0.5$ for negative detuning over the beam current, for different modulation amplitudes.

This effect increases with the beam current so that the maximal bunch length in both stable regions decreases with the current, why it is possible to elongate the bunch with 3 deg stronger than with 4 deg for currents above about 90 mA for negative and 120 mA for positive deviation from the resonance. In total, as discussed in the previous chapter, bunch instabilities are much stronger for the positive frequency deviation. That is why for the negative deviation, not only frequencies closer to the resonance are suitable but therefore also the stable bunch lengthening due to PM is much more effective, so that the bunch length is $(19.0 \pm 5.9)\,\%$ larger on average for the 3 deg excitation.

6.3. Modulation amplitude dependence of the PM detuning curves

In contrast to the beam current steps, the relative changes between the three PM excitation amplitude settings of 3 deg, 4 deg and 5 deg are quite big, why the different influence on the average bunch length detuning curve can be seen clearly and is shown in Figure 6.12 for different beam current settings.

Table 6.4.: The detuning curve parameters for different modulation amplitudes but the same beam current are summed up. The shift of the resonance frequency is dominated by the uncertainty of this value.

(a) 90mA

mod. Amplitude	current (mA)	$f_{\max}$ (Hz)	$\sigma_{\text{detun.}}$ (Hz)	$\sigma_{\max}$ (ps)
3deg	88.2mA	66900 ± 150	562.8 ± 23.7	70.7 ± 0.1
4deg	91.1mA	66760 ± 90	588.4 ± 14.3	89.4 ± 0.2
5deg	89.5mA	66650 ± 80	629.6 ± 13	100.8 ± 0.4

(b) 115mA

mod. Amplitude	current (mA)	$f_{\max}$ (Hz)	$\sigma_{\text{detun.}}$ (Hz)	$\sigma_{\max}$ (ps)
3deg	113.0mA	66870 ± 170	607.2 ± 24.3	78.4 ± 0
4deg	109.6mA	66710 ± 120	636.6 ± 18.2	91.6 ± 0.2
5deg	106.6mA	66470 ± 90	700.7 ± 14.6	103 ± 0.5

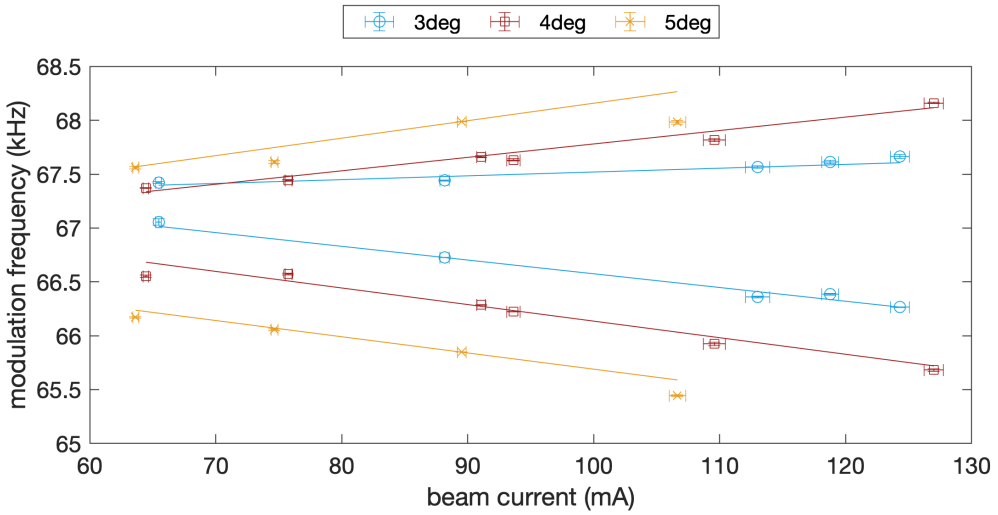

Figure 6.10.: Limit modulation frequency, that fulfills stable criteria for both directions of detuning over the beam current, for different modulation amplitudes. The intersection point of the two lines describes the maximal beam current that fulfills the stable criteria even at the resonance of the detuning curve.

As already described in the previous chapter, the average bunch lengthening is enhanced by the larger excitation amplitude not only for the resonance condition, for which the lengthening effect with 5 deg excitation is at least twice as high as for 3 deg, but also for the whole detuning curve. In Figure 6.13 the maximal average bunch length shows a linear correlation with the excitation amplitude, whose fitting parameter are summed up in Table 6.6. From this, it becomes apparent that a change of 1 deg increases the bunch length by about 15 ps, whereby this lengthening shrinks with the beam current, which is based on the lengthening saturation, discussed in Section 6.2. For a more detailed analysis not only for the linearity of the correlation but also the current dependency, additional excitation amplitude steps, especially below 4 deg or even 3 deg are necessary.
In addition to that, a larger excitation amplitude leads the resonance frequency to smaller values, as shown in Figure 6.12. Despite the clear tendency, the shift of the resonance frequency is dominated by the uncertainty on this value (Table 6.4). Nevertheless, the movement of the resonance agrees with the KARA simulation results in [34]. This negative frequency shift emerges from the motion of the harmonic oscillator system. This effect increases with the modulation amplitude and can cause the negative shift of the detuning curve and its resonance.
For all different beam current conditions, the shape of the average bunch length detuning curves depends on both flanks in different ways on the increased excitation amplitude

Table 6.6.: Fitting parameter from Figure 6.13 for the modulation amplitude dependence of the maximal bunch length, based on the fitting function: $\sigma = m \cdot \Psi_{\mathrm{PM}} + c$. It shows, that the lengthening effect due to an increasing of the modulation amplitude, shrinks with higher beam current.

current (mA)	m (ps/ deg)	c (ps)
63.6	15.29± 0.04	21.55±0.12
74.7	14.4±0.7	26.82± 2.9
89.5	13.8±3.4	33.43± 14.7
106.6	12.9± 0.8	39.8± 2.4

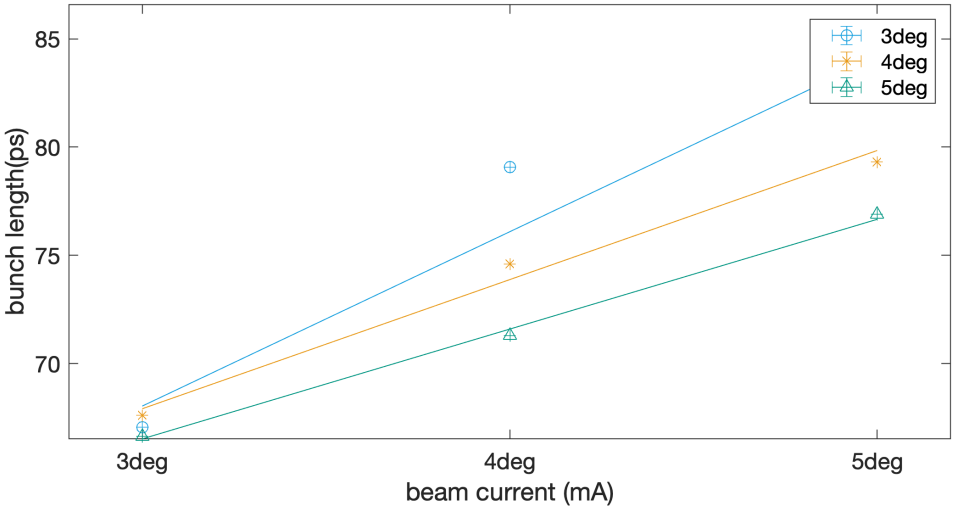

Figure 6.11.: Bunch length under PM with the limit modulation frequency for negative detuning over the beam current. Because of stronger instabilities for higher modulation amplitudes, the stable region moves away from the resonance. That is the reason, why the 3 deg excitation enlarges the bunch more effective at for high current configurations.

(Figure 6.12), but both in a similar manner to the current dependency. Except for the 11 mA situation, the amplitude does not have any influence on the bunch length for a modulation frequency above the resonance. As described for the current dependency, an amplitude dependence occurs not until close to respective resonance, where the lengthening due to PM reaches its maximum.
For the negative deviation from the resonance, the detuning curve flank tends to enhance the negative detuning for larger excitation amplitudes, because of the resonance shift due to the non-linearity of the oscillator motion. In addition to that, the asymmetry decreases as the amplitude increases in the way that the left side tail becomes smaller, and the detuning curve becomes more symmetrical. This second change of the bunch shape can be seen in the width of the detuning curve, which is plotted in Figure 6.14 and does not have the same linear amplitude dependency as the maximum bunch length. The local minimum in the range of 4 deg for all currents up to 90 mA occurs because for the lower excitation amplitudes the asymmetric tail dominates the width instead of the peak height.

Also, for the amplitude dependency, the frequency regions of a stable bunch and, therefore, the maximal suitable bunch lengthening due to PM is of interest. Because the negative deviation allows stronger lengthening while fulfilling the stability criteria $\Gamma > 0.5$ for all detuning curve configuration, here only the limit situation on this side is discussed. In the Figures 6.15 and 6.16 the amplitude dependence of the borderline frequency respectively its corresponding average bunch length is shown.

Table 6.7.: Fitting parameter from Figure 6.15 for the modulation amplitude dependence of the limit frequency for negative detuning, based on: $f_{\mathrm{PM}} = m \cdot \Psi_{\mathrm{PM}} + c$ for different beam current conditions.

current (mA)	m (kHz/ deg)	c (kHz)
63.6	-0.17±-0.06	67.6±-0.3
89.5	-0.117±-0.0003	67.233±-0.002
106.6	-0.21±-0.01	67.53±-0.05

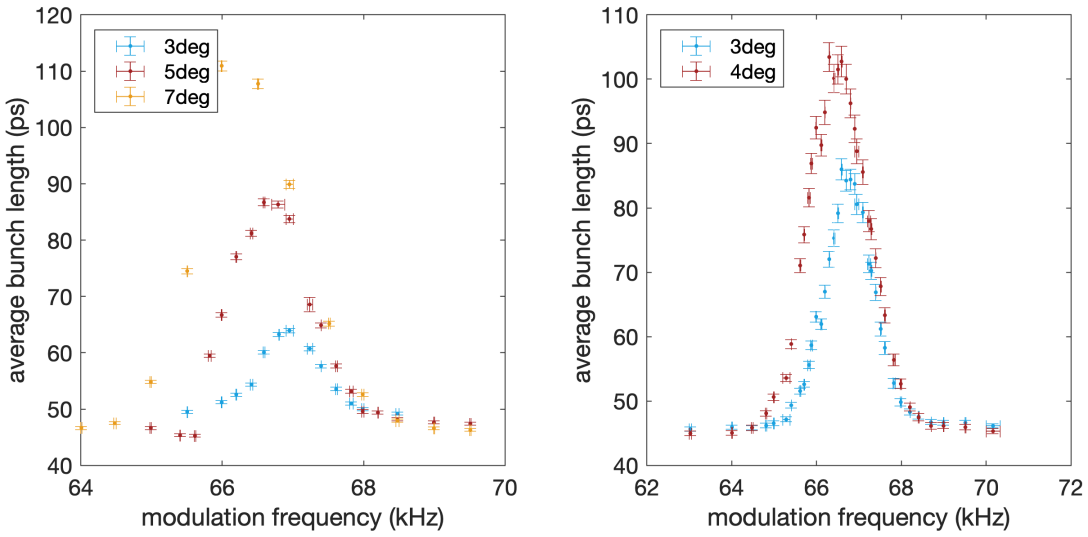

(a) 11 mA

(b) 117 mA

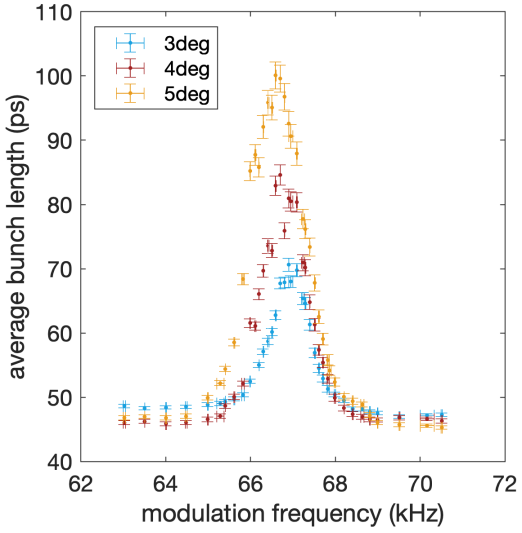

(c) 75 mA

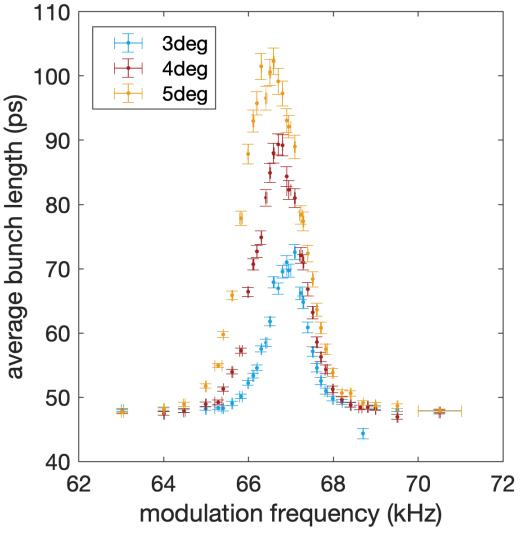

(d) 88 mA

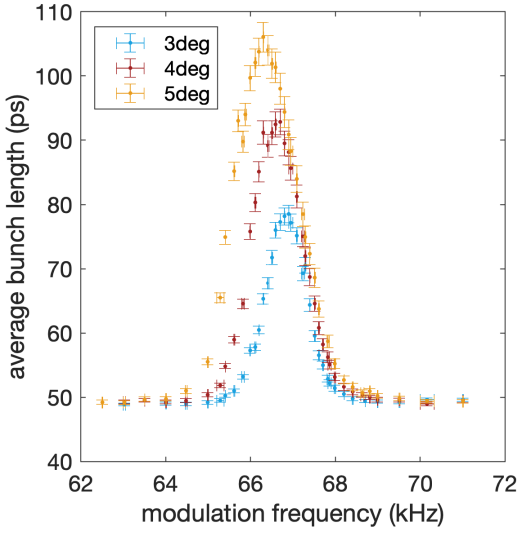

(e) 110 mA

Figure 6.12.: Average bunch length detuning curves for different modulation amplitudes with the same beam current.

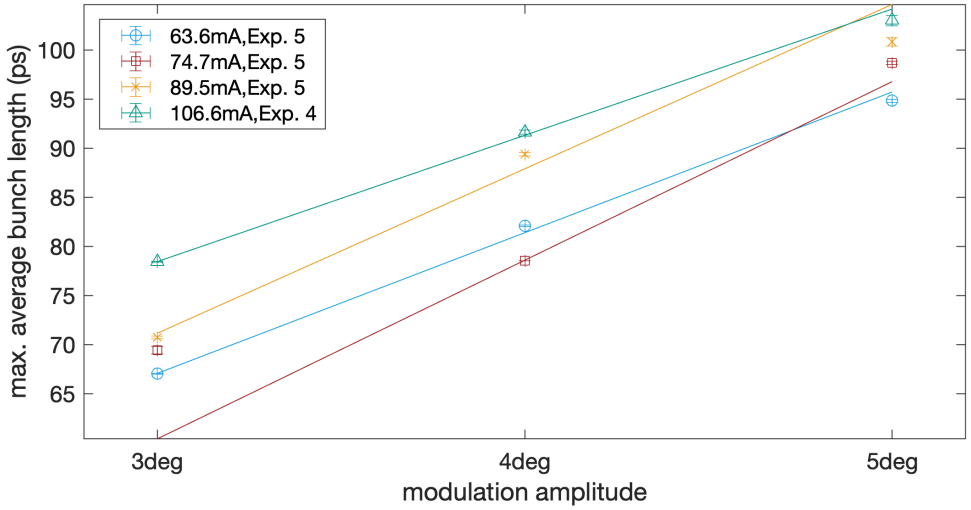

Figure 6.13.: Bunch length under PM with the resonance modulation frequency over the excitation amplitude with a linear fitting. The information content of this fitting is very low because of the small number of data points but shows a clear trend.

For both a nearly linear correlation can be seen, whereby the small number of only 3 different amplitudes does not allow a very detailed analysis of this. Nevertheless, one can see that the slope of the linear fit (Table 6.8) is $(55.1 \pm 12.9)\,\%$ smaller on average than for the maximum bunch length and depends much stronger on the beam current.

6.4. Reproducibility of PM detuning curves

For the current and amplitude dependency discussion in the previous two sections, only the results from experiment 3 on were used. In Figure 6.17 the bunch length detuning curve from different experiments with nearly the identical PM settings are illustrated. In Section 6.2 it has been shown, that the beam current dependence of the detuning curve is minimal, why the differences in the amplitude and resonance frequency of the curve with this small beam current variation of maximal 5.1 mA, should be justified by other reasons.

In the Figures 6.17a and 6.17b it can be seen clearly that the lengthening effect due to PM is much smaller for Exp. 2, for different beam current configuration, why the maximal bunch length is $(20.0 \pm 0.2)\,\%$ at 84.4 mA and $(28.2 \pm 3.8)\,\%$ at 113.1 mA shorter. Nevertheless, during this experiment, the current dependency, shown in Figure 6.17e, is similar to the experiments discussed before, so that the maximal bunch length is reduced identically for all beam current settings.
Besides, Figure 6.17b also shows that for Exp.1, the detuning curve with the parameters $(3°/113.7\,\mathrm{mA})$ is shifted by (1167 ± 193) Hz to larger modulation frequency, in which the

Table 6.8.: Fitting parameter from Figure 6.16 for the modulation amplitude dependency of the bunch length, under PM with the limit frequency for negative detuning, based on: $\sigma = m \cdot \Psi_{\mathrm{PM}} + m$.

current (mA)	m (ps/ deg)	c (ps)
63.6	8.00 ± 4.01	44.1± 15.9
89.5	5.94±1.18	50.1±4.6
106.6	5,09±0.49	51.2±1.9

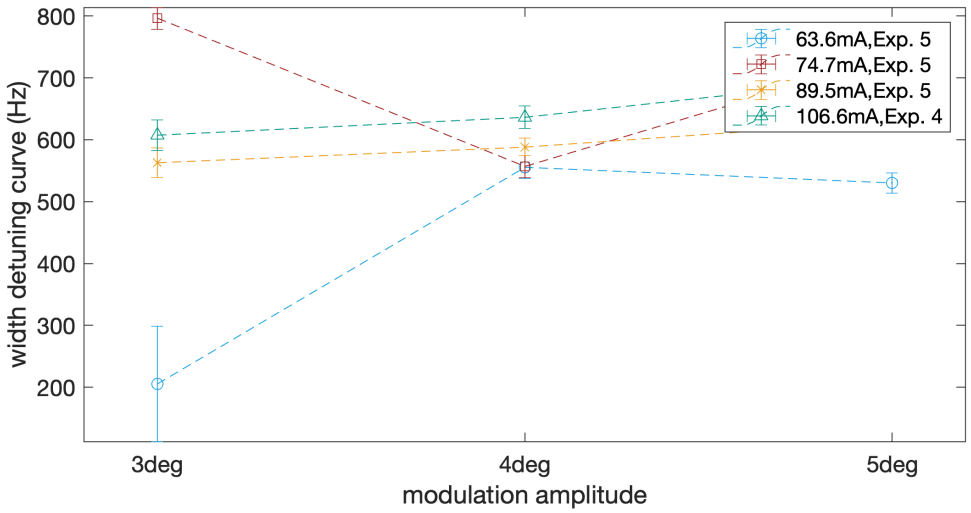

Figure 6.14.: Width of the detuning curve over the excitation amplitude. The width is being influenced by the asymmetry, which dominates for small modulation amplitudes, and the peak height. This results in a local minimum in the range of 4 deg.

maximal bunch length is only reduced by $(9.6 \pm 4.8)\,\%$ in comparison with the later experiments. In this and also in the Figures 6.17c and 6.17d, it shows up, that from Exp. 3 on the detuning curves are reproducible very well, why these results are used for all the parameters discussion.
In all experiments, including Exp.2, the filling pattern, the RF amplitude, and the magnet optics are set in the same way, which neither explains the shift nor the decreased lengthening. The different lengthening may be caused by a change of the induced voltage inside the cavity, because of different tuner condition due to e.g. temperature changes in the KARA hall. The RF frequency changes day-by-day, so that the shift of the detuning curve may be a result of this frequency instability.

In summary, it shows that the resonance frequency, as well as the limit frequency for the stable bunch on the negative detuning flank, have a small beam current dependency. So for the possible including of PM in the normal user operation, the modulation frequency only has to be changed very slowly because of the particle and, therefore, current loss. This negative detuning flank is more interesting than the positive one, because a stronger lengthening of the bunch, while the stability criteria $\Gamma > 0.5$ is fulfilled, is possible for all current and modulation amplitude conditions. From the amplitudes examined in this work, the 3 deg excitation is the best and most stable configuration, especially for currents above 100 mA, because the higher amplitudes create strong instabilities, why the lengthening becomes less effective. So the borderline PM frequency, with 3 deg amplitude, may be interesting for the user operation, whose current dependency is given by

$$f_{\mathrm{PM,border,left}} = -(12.75 \pm 0.30)\,\frac{\mathrm{Hz}}{\mathrm{mA}} \cdot I + (67.85 \pm 0.08)\,\mathrm{kHz} \tag{6.3}$$

with the beam current I.

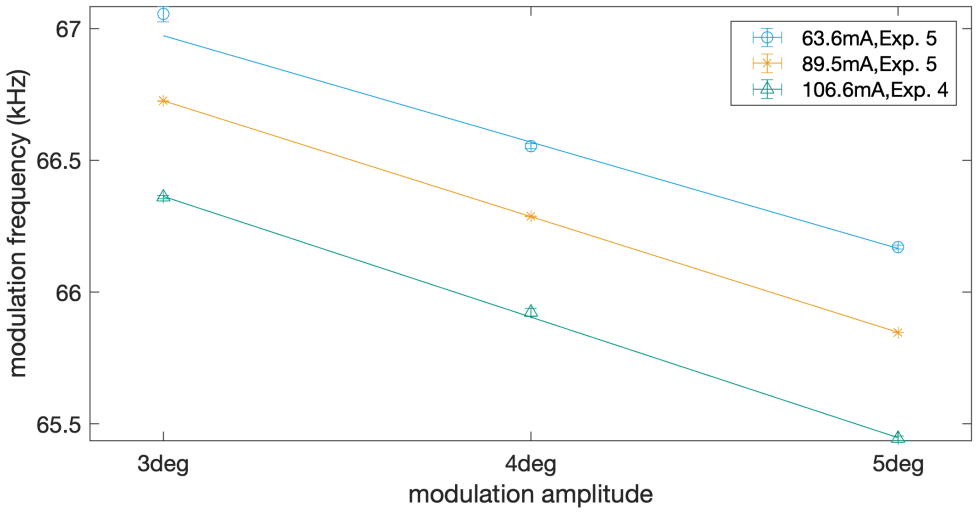

Figure 6.15.: Limit modulation frequency, that fulfills stable criteria for negative detuning over the modulation amplitude.

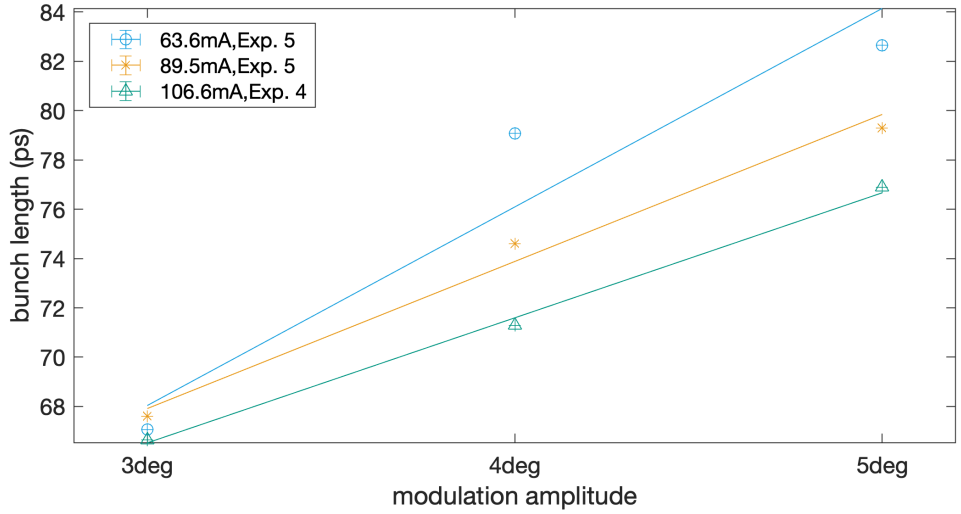

Figure 6.16.: Bunch length under PM with the limit modulation frequency for negative detuning over the excitation amplitude. A nearly linear correlation can be seen, whereby a detailed analysis is not possible because of only 3 data points.

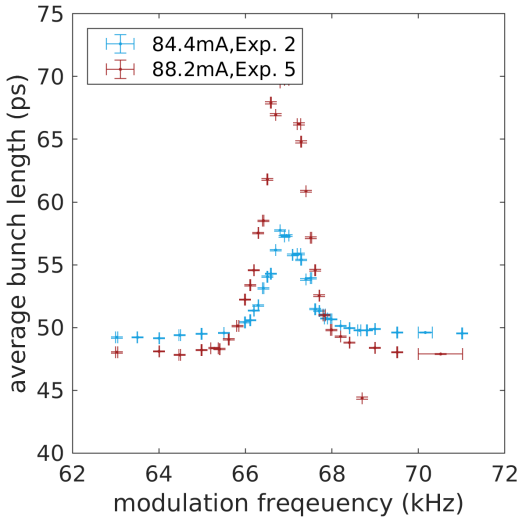

(a) 3 deg

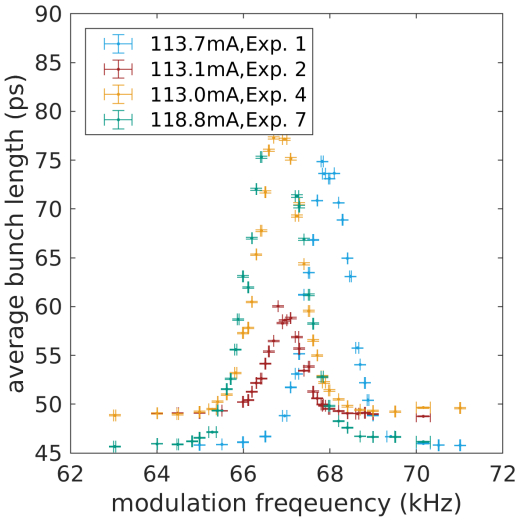

(b) 3 deg

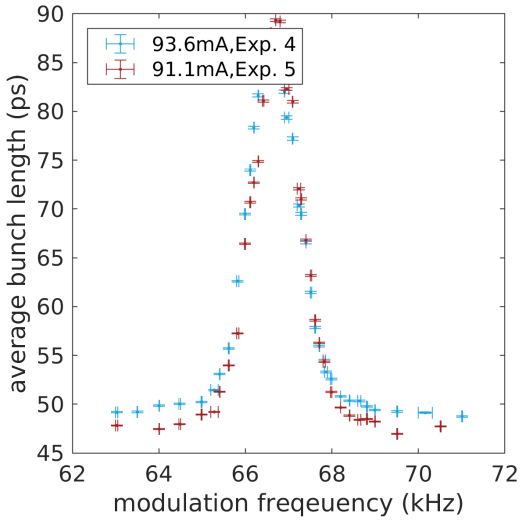

(c) 4 deg

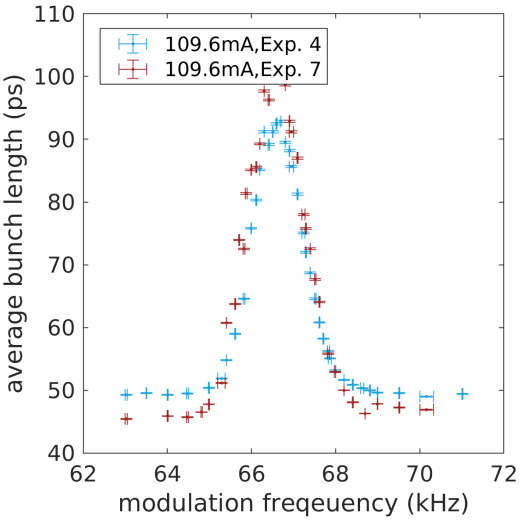

(d) 4 deg

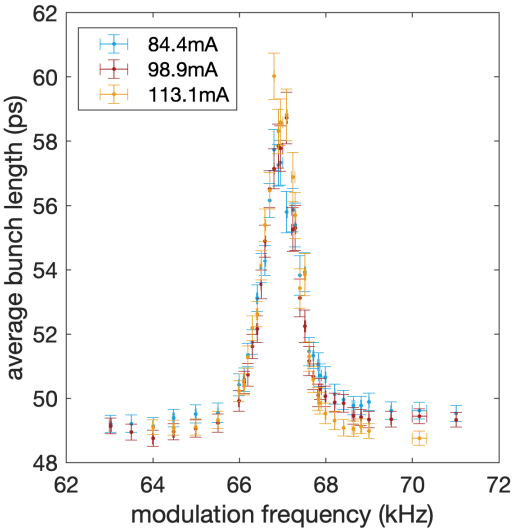

(e) 3 deg/ Exp.2

Figure 6.17.: Reproducibility of the PM detuning curves The detuning curves from different experiments with nearly the same PM conditions are plotted. For all beam currents is the lengthening due to PM in Exp. 2 drastically reduced. In Exp.1 is the detuning curve, compared to the other experiments shifted to higher modulation frequencies ((a)-(d)). In (e) the detuning curves from Exp. 2 for different beam currents are shown. This shows, that the reduction of the lengthening is independent of the beam current.

7. Extension of total and Touschek lifetime due to phase modulation

In this last chapter, the influence of the phase modulation (PM) on the total and especially on the Touschek lifetime, will be shown. The first section is focused on the lifetime detuning curve and its similarities and differences with the bunch lengthening due to PM. In the second section, the Touschek lifetime is determined, and the dependence of the Touschek and total lifetime on the beam current will be discussed.

7.1. Total lifetime detuning

In the Figure 7.1 the rough detuning curves of the total beam lifetime at KARA under PM for different currents and modulation amplitudes are plotted. It turns out, that the modulation with an amplitude of 5 deg does not have any recognizable frequency dependence (Figure 7.1d), but fluctuates around (34.7 ± 1.0) h, which means an increasing of the total lifetime of (12.0 ± 4.9) % regarding the non-excited condition.
In contrast, it can be seen clearly, that the lifetime depends on the modulation frequency for the 3 deg bunch excitation, so that a resonance peak can be seen. For a modulation at the highest beam current (145.7 mA), it seems that the maximal lifetime extending due to PM is reached near the resonance frequency because the Touschek lifetime becomes irrelevant, why the detuning curve saturates at roughly 31 h. The non-excited beam lifetime decreases significantly with the beam current because the vacuum and the Touschek lifetime depend on the particle number and, therefore, on the beam current. That is why the relative lifetime extension is more interesting for the following discussion and is shown, for different settings in the Figures 7.2 and 7.3. Despite the saturation for the highest beam current condition, there is a significant correlation between the maximal lifetime and the beam current. Summed up in Table 7.1 it shows, that the total lifetime can be extend - for the

Table 7.1.: Detuning curve parameters for the lifetime and bunch length The characteristic parameters for the lifetime, and bunch length (grey) detuning curves are shown for 3 deg modulation for different beam currents. It can be seen that the resonance frequency is similar for both detuning curves at the same conditions, whereas the bunch lengthening is significantly stronger than the lifetime extension at the resonance.

I (mA)	$f_{\text{max.}}$ (Hz)	modulation factor
79.4	66200 ± 210	1.129 ± 0.035
79.4	65850 ± 2720	1.545 ± 0.06
106.3	65890 ± 40	1.212 ± 0.019
106.3	65910 ± 1830	1.53 ± 0.022
145.7	65660 ± 30	1.22 ± 0.014
145.7	65670 ± 1810	1.914 ± 0.037

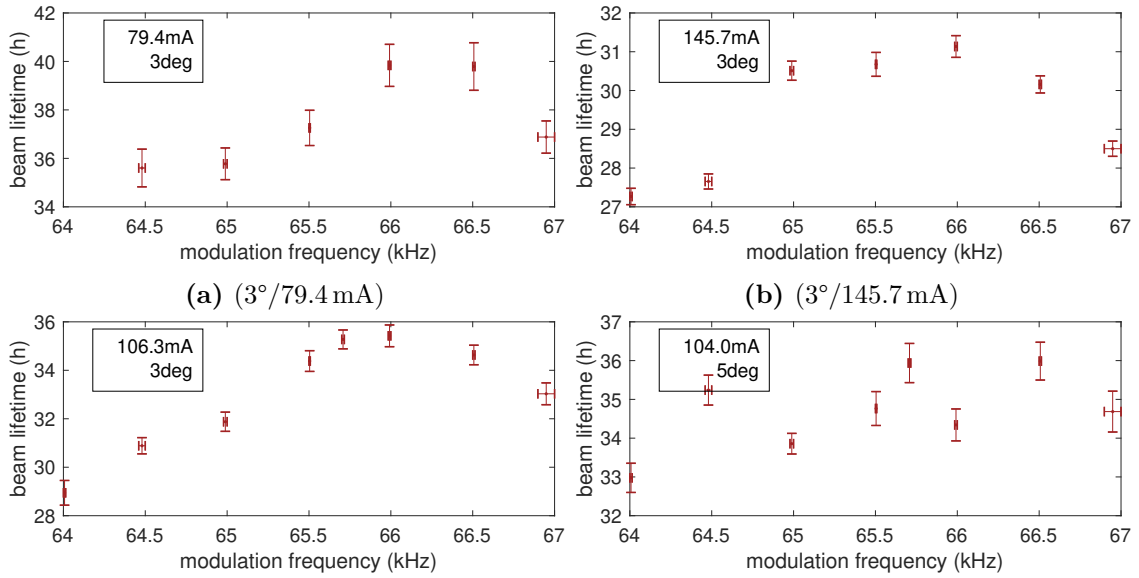

(a) (3°/79.4 mA) **(b)** (3°/145.7 mA)

(c) (3°/106.3 mA) **(d)** (5°/104.0 mA)

Figure 7.1.: Total beam lifetime over phase modulation frequency. For a modulation amplitude of 3 deg, a resonance peak as for the bunch length can be seen. In contrast to that, higher modulation amplitudes do not have a frequency dependence.

configurations in here - by 12.9 % to 22.0 %.
The comparison with the average bunch length detuning curve for the same conditions, which is also shown in Figure 7.3 and Table 7.1. As expected, the resonance frequencies for the lifetime and bunch length are the same, so that the beam current dependence does not differ from the discussion in Section 6.2 and the resonance shifts to smaller modulation frequencies. Because of this similarity, it seems that the bunch length is the only parameter that affects the total lifetime significantly and is itself dependent on the PM frequency, for a modulation amplitude of 3 deg. Also, it can be seen that the bunch length increases much stronger at the PM resonance because the vacuum lifetime terms also limit the lifetime. In analogy to Equation (6.1), the lifetime-bunch-length parameter T is defined as

$$T = \frac{\frac{\tau}{\tau_0}}{\frac{\sigma}{\sigma_0}}. \tag{7.1}$$

The bottom panels in Figures 7.3a to 7.3c, show that lifetime extension due to the bunch lengthening is more effective for shorter a bunch length at the off-resonance condition, because the Touschek lifetime is not relevant at the resonance anymore. Together with the definition of the stable bunch region in the previous chapter, this is another argument for the off-resonance modulation for the user operation.
Also, the lifetime does not have any modulation frequency dependence, for the excitation with 5 deg, and the bunch length is still affected by the PM. Since the bunch is no longer for the off-resonance condition than for the 3 deg modulation amplitude, the lifetime saturation can not be explained by the irrelevant Touschek effect due to a reduced particle density. It means that the PM with such a large amplitude might affect other machine and bunch parameters that have not been considered, such as α_c, the momentum acceptance or a lifetime limitation due to the dynamic aperture. However, this PM parameter setting is not suitable for user operation.

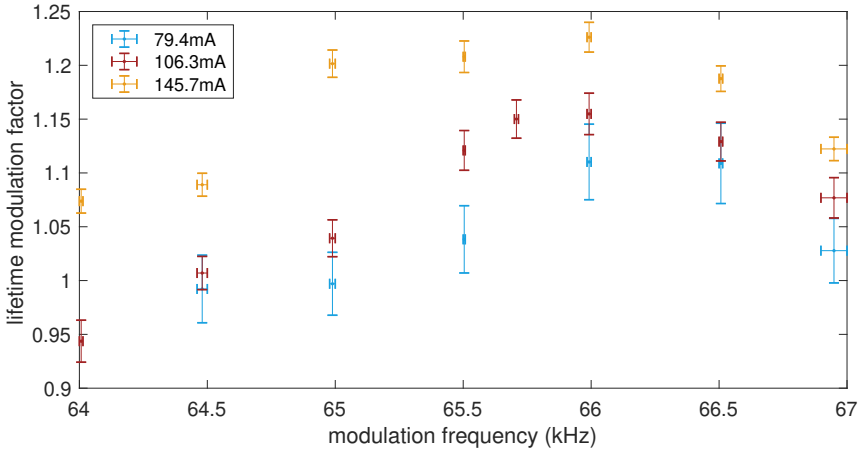

Figure 7.2.: The relative lifetime extension is plotted over the modulation frequency for 3 deg modulation amplitude.

7.2. Touschek lifetime

For the calculation of the Touschek lifetime τ_{touschek} from the total beam lifetime, it is necessary to determine the additional terms, which limits the lifetime. In this work, the impact of the quantum excitation is neglected, and all terms for scattering with rest gas atoms are summed up in τ_{vac}. This term is calculated - under the assumption that the PM does not influence the vacuum lifetime - with the measured total lifetime and the Touschek lifetime term for the non-excited beam condition. Therefore τ_{touschek} is determined by Equation (2.36). In Figure 7.4 is the so estimated Touschek lifetime ($\tau_{\text{touschek}} = \frac{\tau_{\text{vac}} \cdot \tau_{\text{meas.}}}{\tau_{\text{vac}} - \tau_{\text{meas.}}}$) in dependency of the average bunch length for the different PM frequencies plotted. As mentioned before, results in a long Touschek lifetime in a domination of the vacuum terms, why the total and vacuum lifetime are nearly identical. That is the reason why a small uncertainty in the total and vacuum lifetime can cause huge uncertainty for the Touschek lifetime.
For the 3 deg a linear correlation within the scope of the huge uncertainties is observable, why it seems that the bunch length is the only parameter affecting the Touschek effect, which is changed due to the PM. In contrast to most of the previous fittings in this work, for this, the weighted fitting is essential, because the uncertainties depend strongly on the bunch length. It also seems as if the linear fitting works better for the higher beam current condition because the greater particle density in there results in a shorter Touschek lifetime. Therefore the contribution of the Touschek effect becomes relevant for the total lifetime and can be determined more precisely. However, a clear beam current dependence discussion is not possible with 3 settings.
In Figure 7.5, the dependence of the total lifetime on the average bunch length is shown. The fit is based on the assumptions that the vacuum lifetime τ_{vac} is independent of the lengthening and that the bunch length is the only parameter that affects the Touschek lifetime: $\tau_{\text{touschek}} = k \cdot \sigma$, why the theoretical bunch length dependency is given by:

$$\tau(\sigma) = \frac{\tau_{\text{vac}} \cdot (k \cdot \sigma)}{\tau_{\text{vac}} + (k \cdot \sigma)} \tag{7.2}$$

with the fixed and previously calculated vacuum lifetime. Also in here, it shows up, that additional lifetime limiting effects occur for the 5 deg modulation amplitude so that there is no bunch length dependency. For the 3 deg configuration, the bunch lengthening due to PM influences the total lifetime in the way predicted in Equation (7.2), why the used assumptions seem to be correct.
The beginning of the saturation, which marks the bunch length above which the contribution

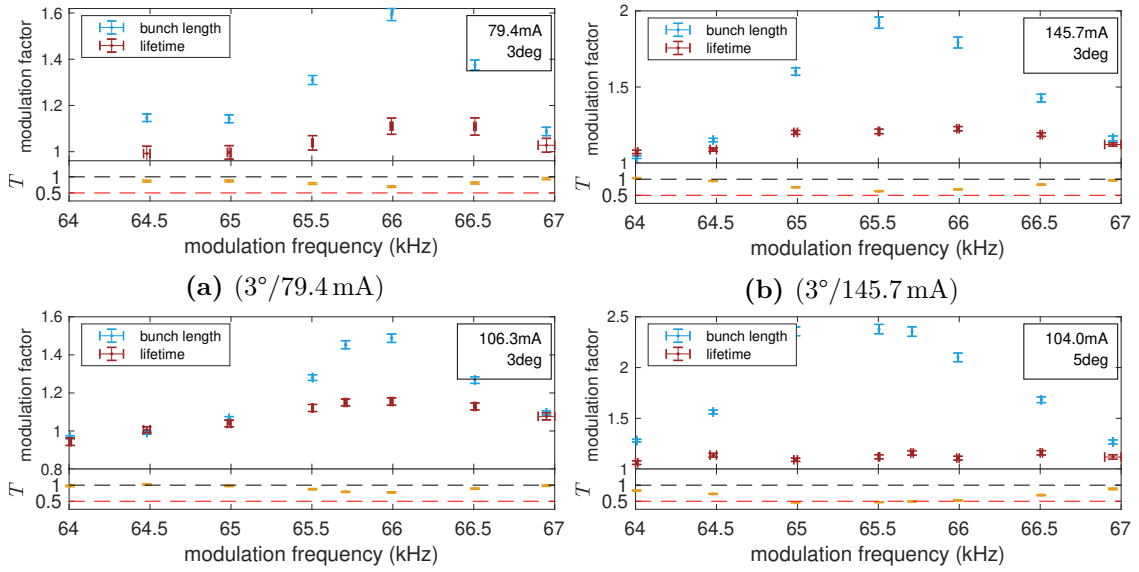

(a) (3°/79.4 mA) **(b)** (3°/145.7 mA)

(c) (3°/106.3 mA) **(d)** (5°/104.0 mA)

Figure 7.3.: In the top panel the relative lifetime extension and bunch lengthening over the modulation frequency are plotted. The bottom panel shows the lifetime-bunch-length parameter T, defined in Equation (7.1). This illustrates, that the bunch lengthening affects the lifetime more effective for off resonance conditions.

of the Touschek effect on the total beam lifetime becomes negligible. It can be seen, that the start saturation shifts to longer bunch lengths with higher beam current, because the Touschek effect depends on the particle density, which also increases with the current, so the Touschek lifetime is still relevant for longer bunches.

From the investigated settings, the (3°/106.3 mA) condition extends the lifetime due to phase modulation most effectively, because the contribution of the Touschek effect is much smaller for the lower beam current and the highest current condition shows not such a great lifetime improvement. This may be caused by a starting over-excitation, comparable with the 5 deg excitation. The region of saturation, in which the lifetime is not extended but the bunch instabilities increase, is not suitable for the PM, why off-resonance phase modulation might be the best solution.

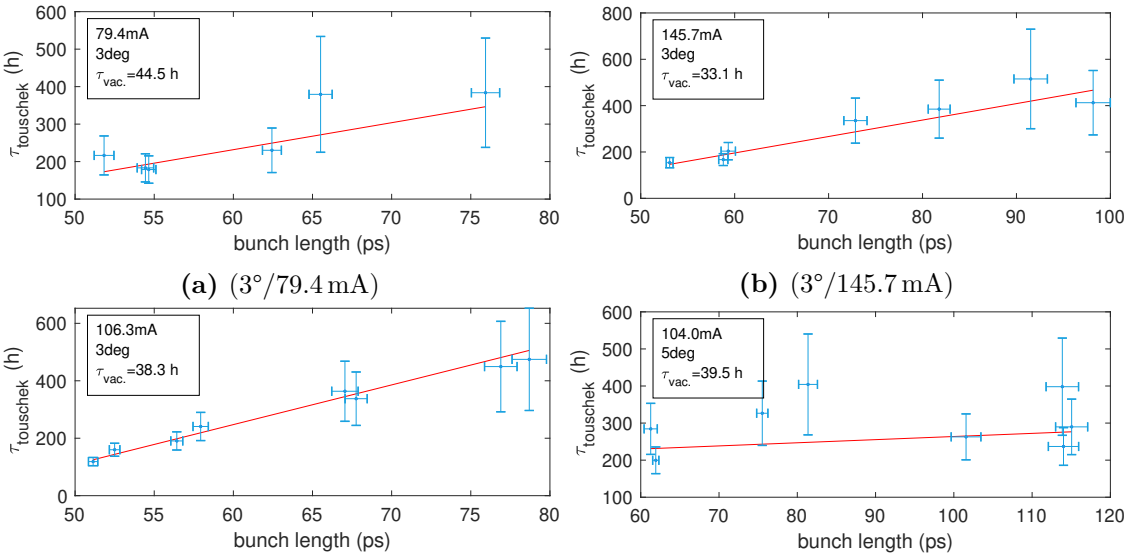

(a) (3°/79.4 mA) **(b)** (3°/145.7 mA)

(c) (3°/106.3 mA) **(d)** (5°/104.0 mA)

Figure 7.4.: The Touschek lifetime is plotted over the average bunch length, which is modified due to PM.The stated vacuum lifetime τ_{vac} is calculated for the non-excited beam condition. The linear fitting is based on the assumption that the PM only affects the bunch length and no other Touschek lifetime parameter.

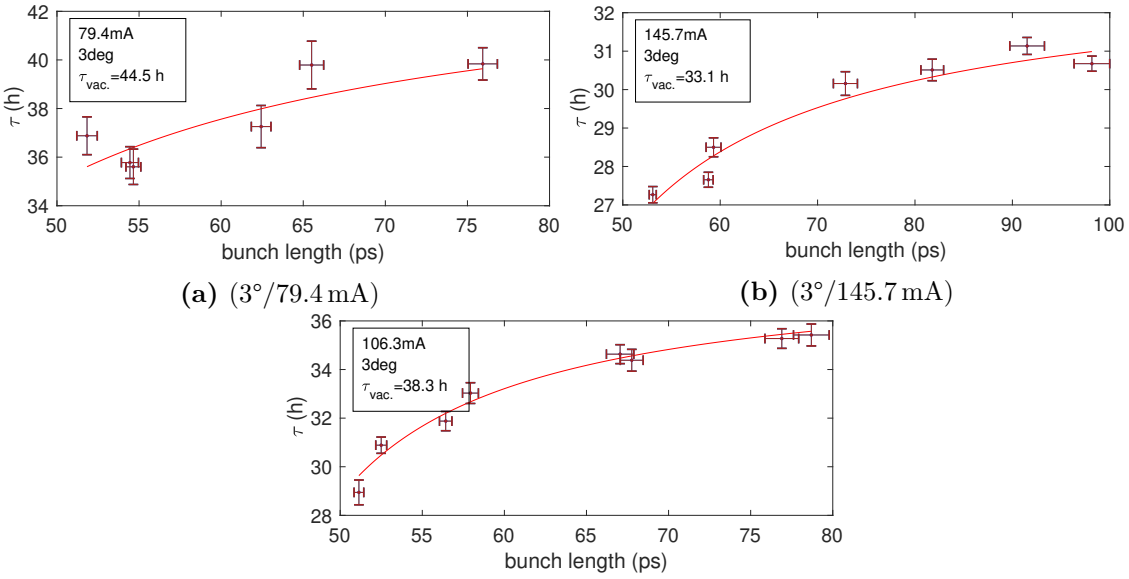

(a) (3°/79.4 mA) **(b)** (3°/145.7 mA)

(c) (3°/106.3 mA)

Figure 7.5.: The total beam lifetime is plotted over the average bunch length, which is modified due to PM. The fitting is based on Equation (7.2) with the assumptions described in Figure 7.4.

8. Summary and outlook

In order to improve the beam lifetime and stability for the synchrotron radiation experiments as well as radiation protection in all operation schemes, the bunch can be elongated due to phase modulation (*PM*), which is of great interest especially for small emittance storage ring with a short Touschek lifetime. In contrast to e.g. harmonic cavities, the PM can be switch on and off relatively easily. Before the RF phase modulation can be included into the normal Karlsruhe Research Accelerator (*KARA*) user operation scheme, a systematic study in what way the longitudinal bunch profile is affected and the search of the optimum PM condition from the modulation amplitude and frequency in dependence of the beam current has to be done. In this thesis, these studies have been started, whereby the modulation frequency was varied around twice the synchrotron frequency, and a first criterion for the optimal condition has bee defined and discussed.

First the longitudinal bunch shaping due to PM has been investigated. It has been shown up that the sign of the deviation from the $2f_\mathrm{s}$ resonance influences the creation and filling of subbunches significantly. For the positive detuning the quadrupole excitation results in a splitting into two subbunches which are oscillating around the core of the bunch, whose oscillation amplitude increases with the modulation amplitude. That is why for a 5 deg modulation the subbunches are separated completely. On the contrary, the bunch is not split for negative deviation from the resonance, so that in this the bunch length oscillation is dominated by lengthening and shorting of the total bunch due to the quadrupole mode excitation.
Nevertheless the average bunch length is increased due to PM, whose modulation frequency dependence has been described by the detuning curve. It has been shown that there is resonance frequency which affects the bunch length most effectively, at which the length - depending on the modulation amplitude and beam current - can be approximately doubled. Therefore the theoretical prediction and simulation results by A. Mochihashi for the shape and asymmetry of the detuning curve has been verified, so the bunch length is influence by the PM up to larger deviation for positive than for negative deviation.
The detuning curve study for different beam currents has pointed out, that the resonance frequency decreases because of the beam loading effect and that the lengthening increases for higher beam current condition. Furthermore the average bunch length increases with the modulation amplitude very strong, why the 5 deg modulation is not practicable for systematic investigations because the bunch length overlays the streak camera (*SC*) range. The different bunch lengthening for positive and negative deviation as well as the temporal changing bunch shape has made the definition of a longitudinal stability criterion necessary. It could be demonstrated, that this criterion is fulfilled for smaller deviation from the resonance for the negative detuning, so that the bunch can be stronger elongated, which makes the negative deviation more interesting for the including of the PM into the user operation scheme. For the mainly investigated 3 deg modulation it could be seen, that the stability criterion is fulfilled at the resonance for beam currents below 42 mA, which is significantly below the KARA user operation condition. The resulting borderline frequency

of the stable region has been defined as the optimal PM condition in dependence of the beam current.
At the end the phase modulation affect on the total and Touschek lifetime has been shown. In this it has been observed, that for huge modulation amplitudes a lengthening of the bunch does not extend the lifetime anymore, which can not be explained by the irrelevant Touschek lifetime. However, the modulation with 3 deg elongates the total lifetime effectively. Thereby it has been verified, that the bunch length is the only Touschek lifetime parameter, which is affected by the phase modulation.

This thesis has not only presented first systematic studies of PM at the KARA storage ring but has also shown unanswered questions and aspects which makes further experiments on this topic reasonable. The beam loading effect has been identified as a main reason for the shift of the resonance and the more effective lengthening at higher beam currents. For an independent investigation of other relevant parameters, experiments in single bunch operation should be done, where the beam loading effect inside the cavities is suppressed. To claim the ideas for different lengthening at different experiment days, additional measurements of the radio frequency (RF) tuning and the stability of the radio frequency must be done. For the measurements in this thesis only the RF acceleration voltage in one sector has been modulated. Because KARA has two acceleration section it would be possible to modulate both at the same time with different or identical amplitude and frequency. However, the phase shift between the sections must then be taken into account. Furthermore an additional look at the PM affect on the transversal plane might be interesting especially from the point of view of beam and radiation quality. For this it is also necessary to discuss and define a radiation quality criterion in cooperation with the radiation users to find the optimum PM condition. As it has been shown in this thesis, the Touschek lifetime is relevant for the normal user operation scheme at KARA, already. In the low and negative α_c scheme, the bunch length is much smaller, why the Touschek effect dominates the lifetime in there, so that the PM in this scheme might be of interest, too.

A. Appendix

A. Streak camera row images

The streak camera raw data show the longitudinal profile of the odd and even bunches separated into two bands and its change over a period of 200 µs. In here this is illustrated for different phase modulation amplitudes, beam currents and modulation frequencies. The frequencies correspond to either the $2f_s$ resonance or a deviation of about ± 500 Hz or ± 1000 Hz.

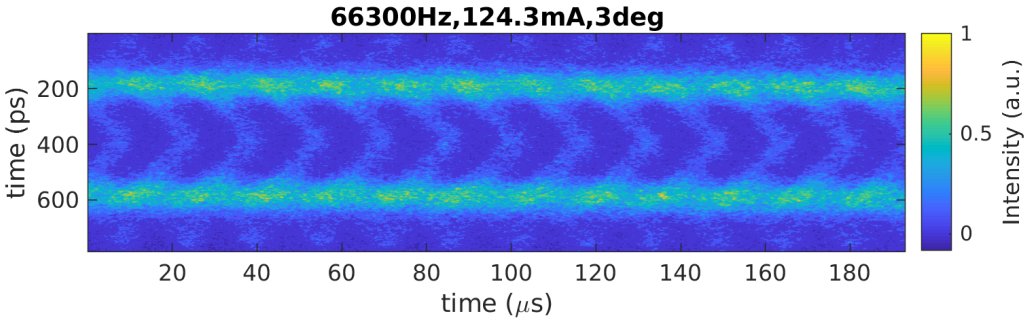

Figure A.1.: Off resonance -500 Hz PM excitation at (3°/124.3 mA)

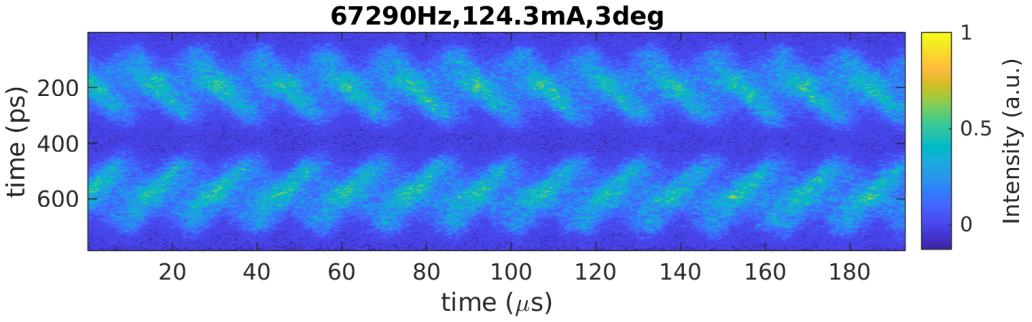

Figure A.2.: Off resonance +500 Hz PM excitation at (3°/124.3 mA)

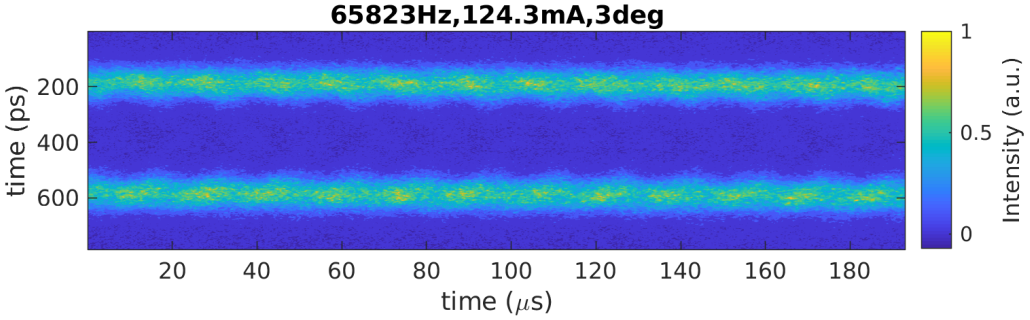

Figure A.3.: Off resonance -1000 Hz PM excitation at (3°/124.3 mA)

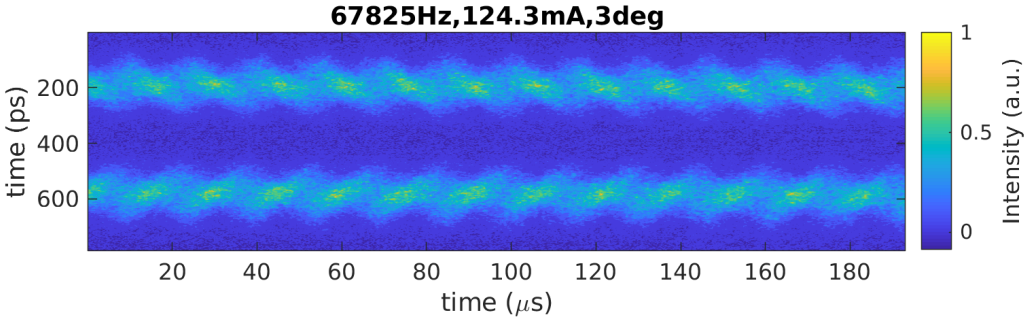

Figure A.4.: Off resonance +1000 Hz PM excitation at (3°/124.3 mA)

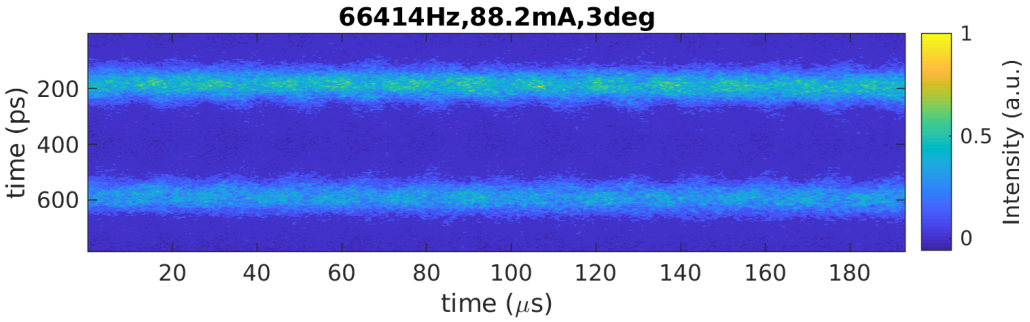

Figure A.5.: Off resonance -500 Hz PM excitation at (3°/88.2 mA)

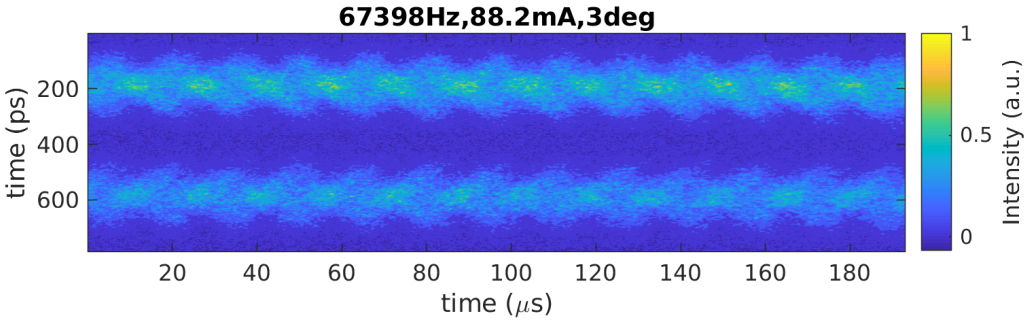

Figure A.6.: Off resonance +500 Hz PM excitation at (3°/88.8 mA)

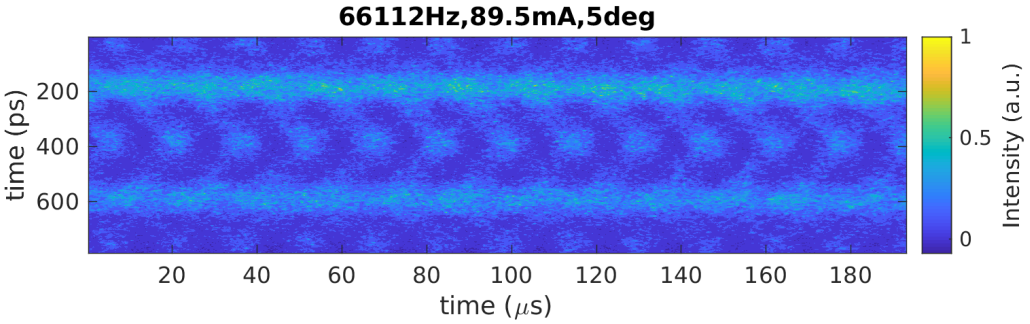

Figure A.7.: Off resonance -500 Hz PM excitation at (5°/89.5 mA)

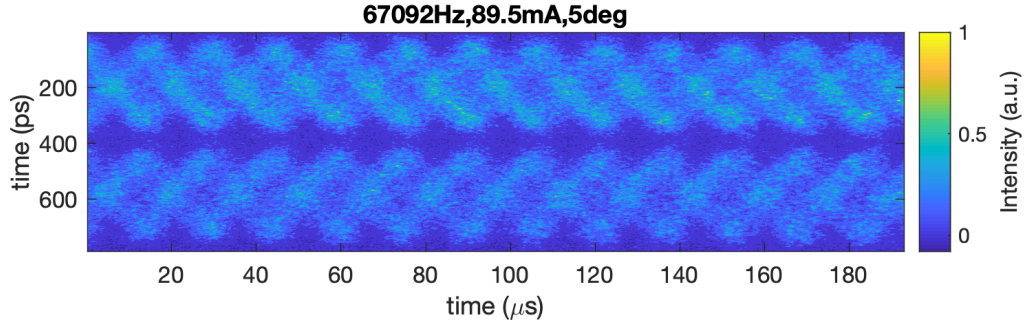

Figure A.8.: Off resonance +500 Hz PM excitation at (3°/89.5 mA)

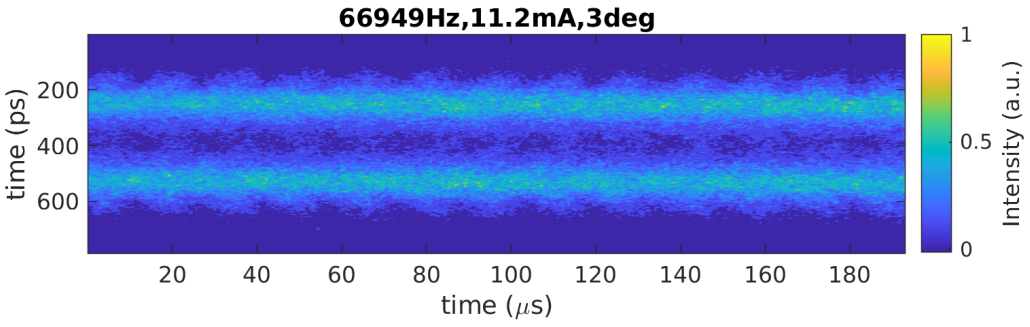

Figure A.9.: On resonance PM excitation at (3°/11.2 mA)

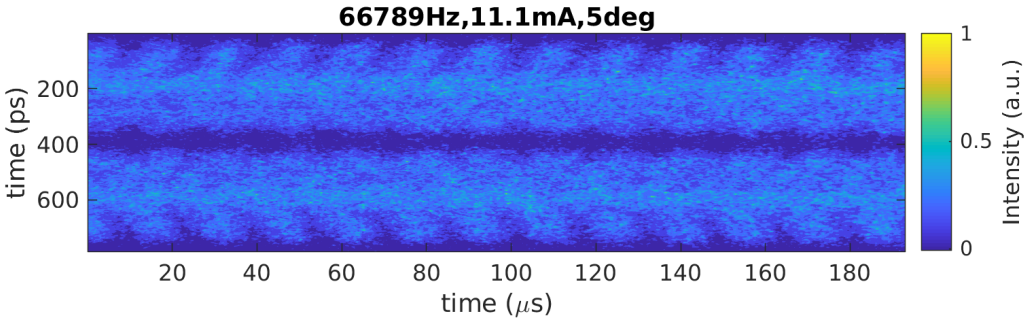

Figure A.10.: On resonance PM excitation at (5°/11.1 mA)

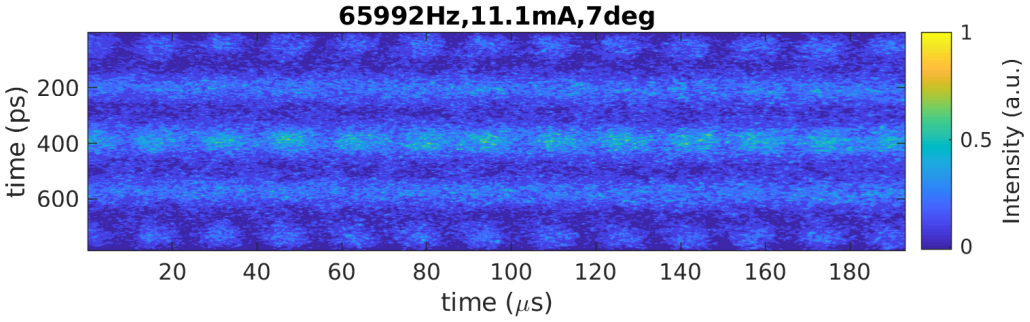

Figure A.11.: On resonance PM excitation at (7°/11.1 mA)

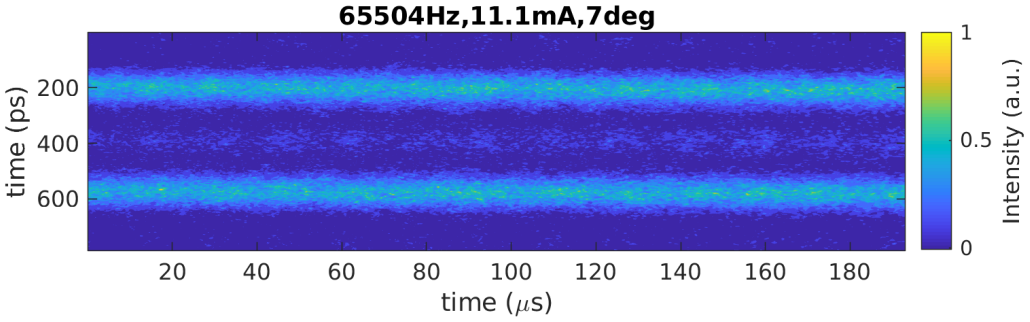

Figure A.12.: off resonance +500 Hz **PM excitation at** (7°/11.1 mA)

B. Longitudinal profile at specific time points

In the top panel the SC raw data the upper of the two bands is shown throughout roughly three periods of the $2f_s$ resonance oscillation and the averaged longitudinal bunch profile over the total 200 µs range. The bottom panel illustrates the longitudinal profile for three specific bunch length situations. From left to right the bunch shape for the minimal, maximal and average bunch length is displayed, which correspond to the grey marked spots in the SC image. Analogous to the previous section, this is shown for different PM amplitudes, beam currents and modulation frequencies. The frequencies correspond to either the $2f_s$ resonance or a deviation of about ± 500 Hz or ± 1000 Hz.

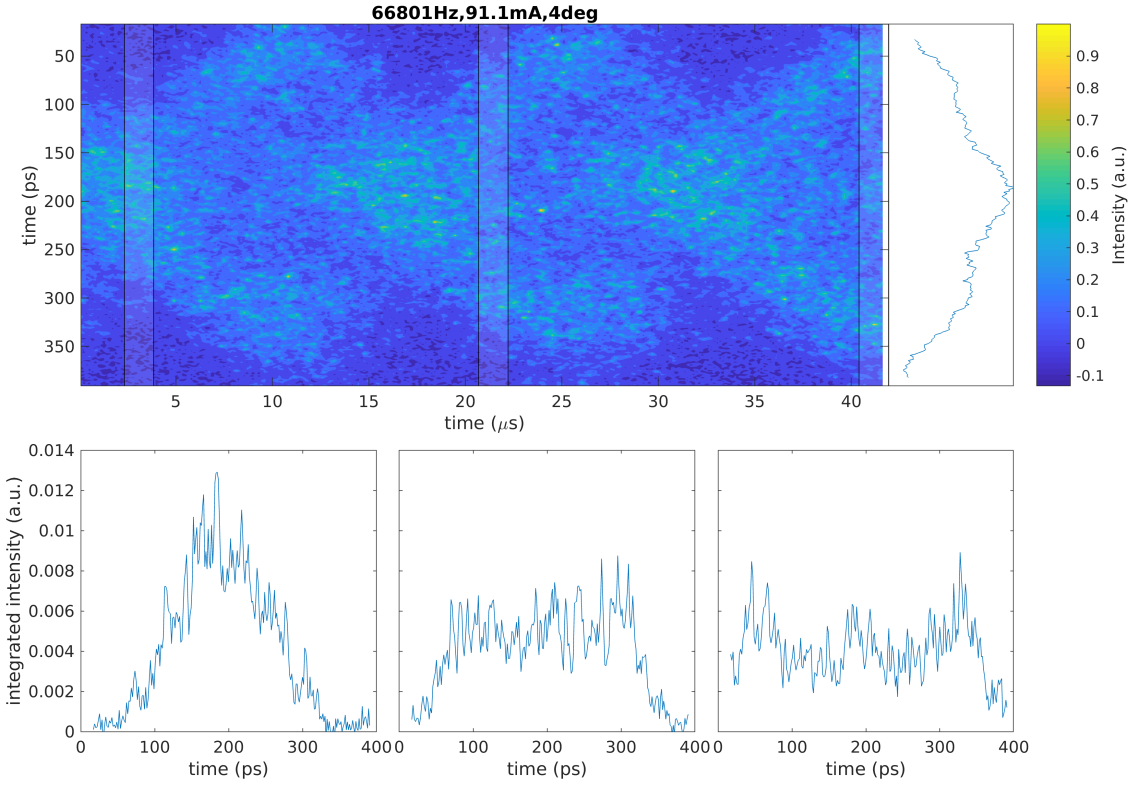

Figure B.1.: Off resonance +500 Hz PM excitation at (4°/91.1 mA)

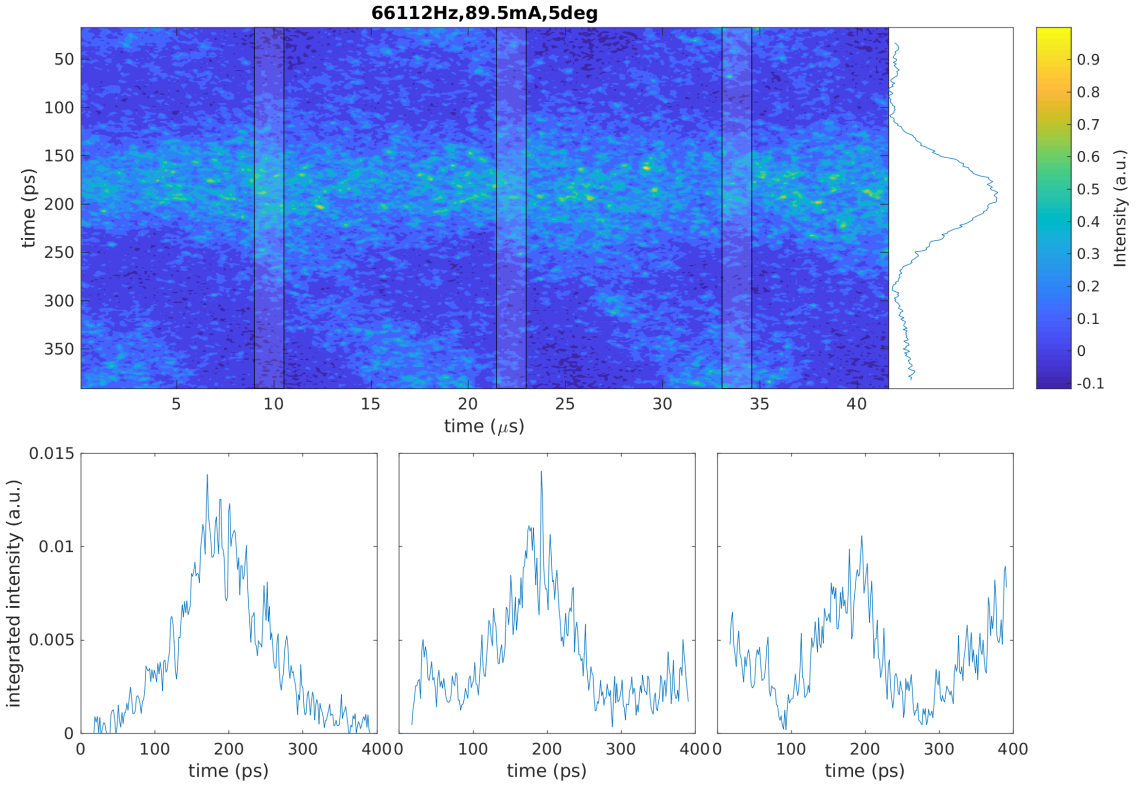

Figure B.2.: Off resonance -500 Hz PM excitation at (5°/89.5 mA)

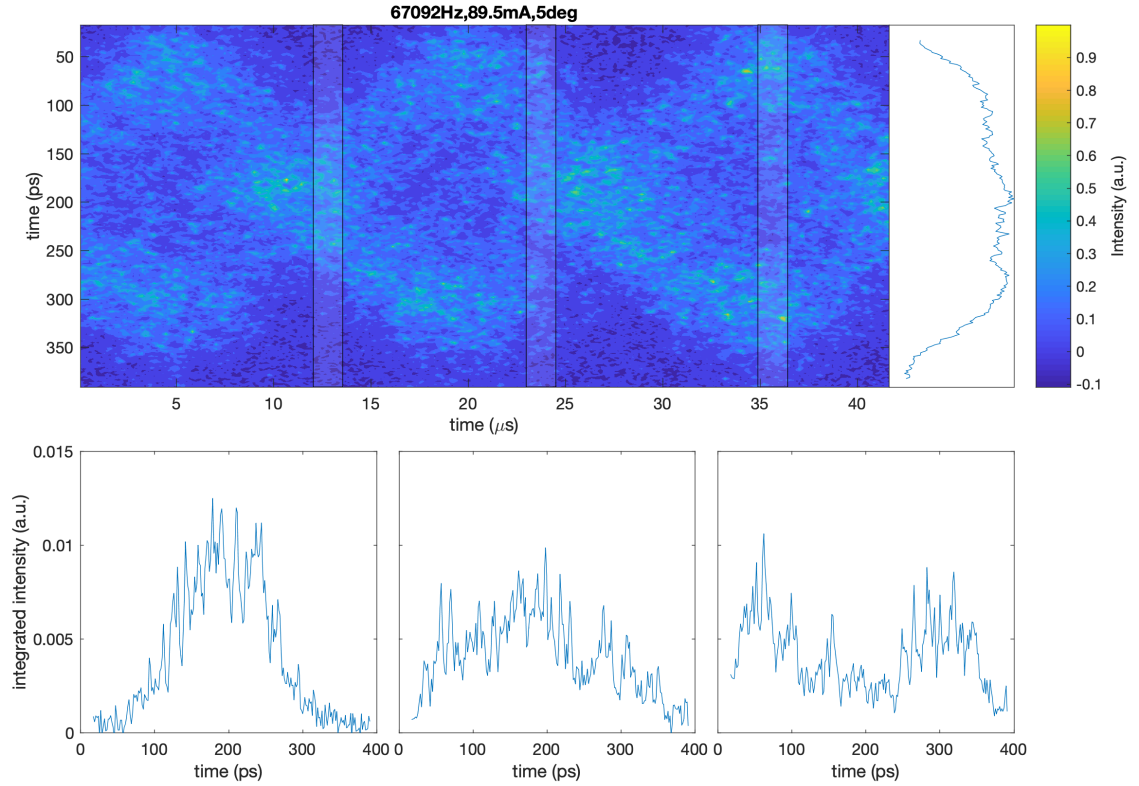

Figure B.3.: Off resonance +500 Hz PM excitation at (5°/89.5 mA)

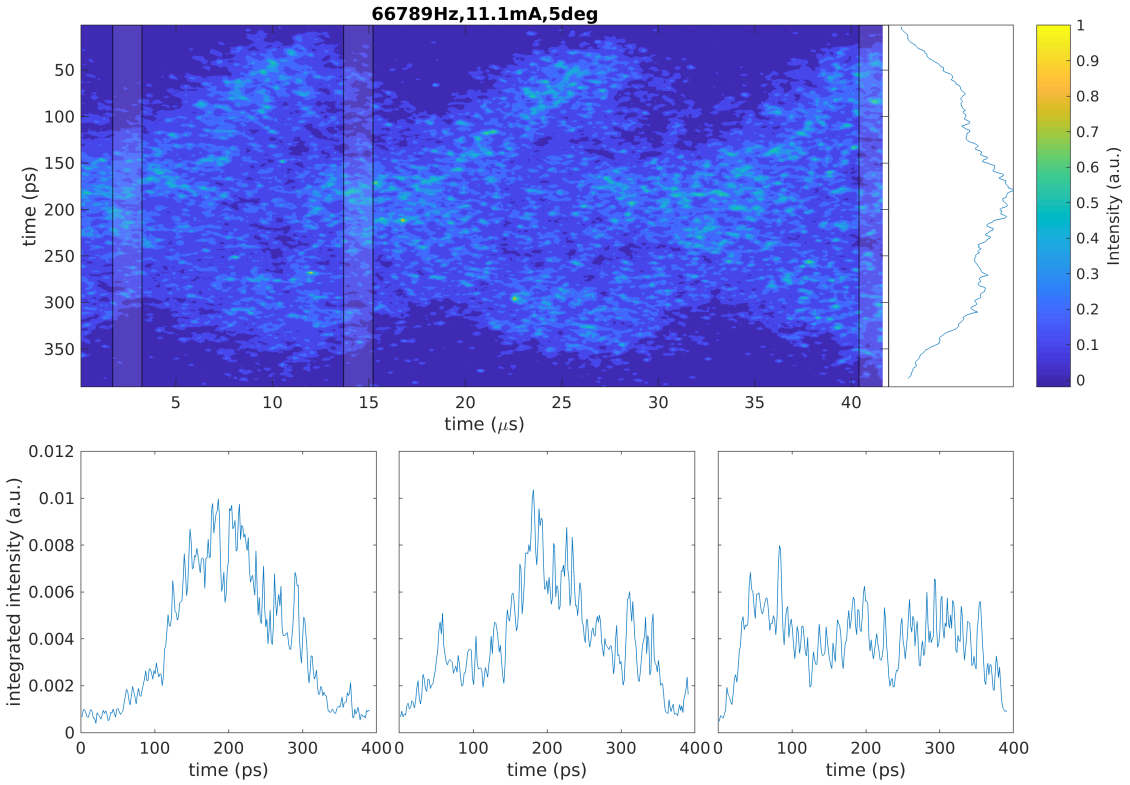

Figure B.4.: On resonance PM excitation at $(5°/11.1\,\mathrm{mA})$

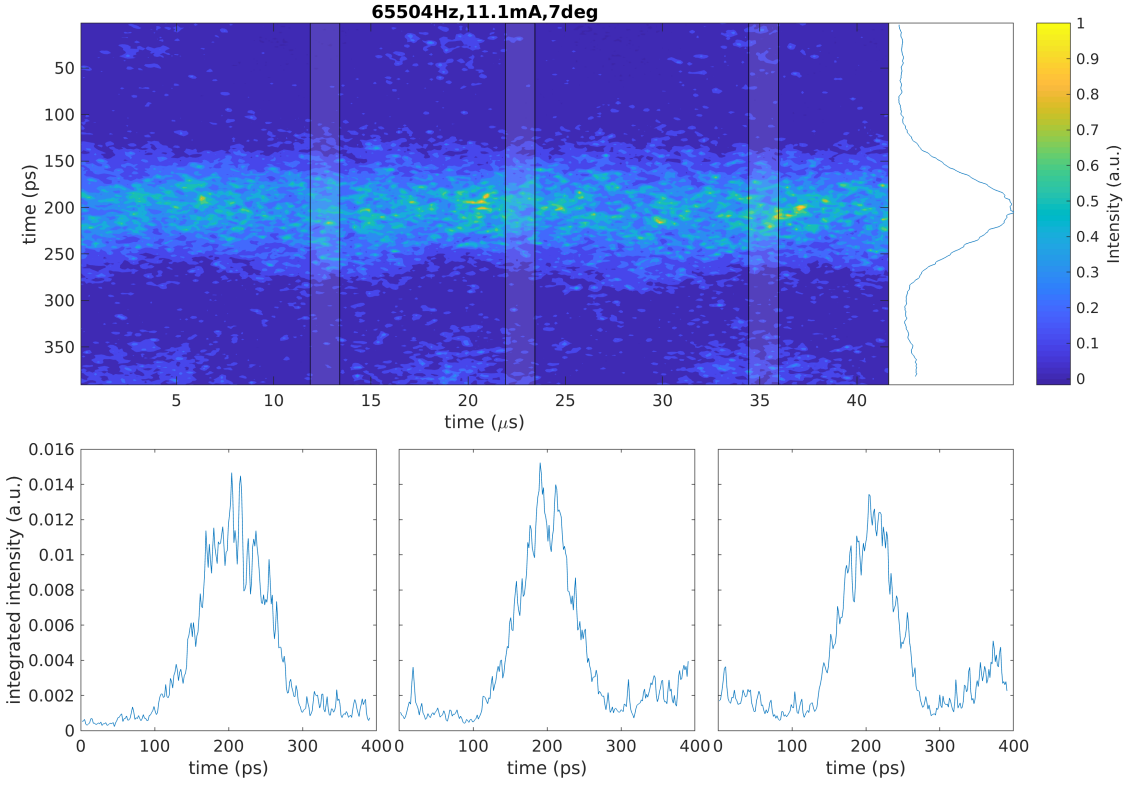

Figure B.5.: Off resonance -$500\,\mathrm{Hz}$ **PM excitation at** $(7°/11.1\,\mathrm{mA})$

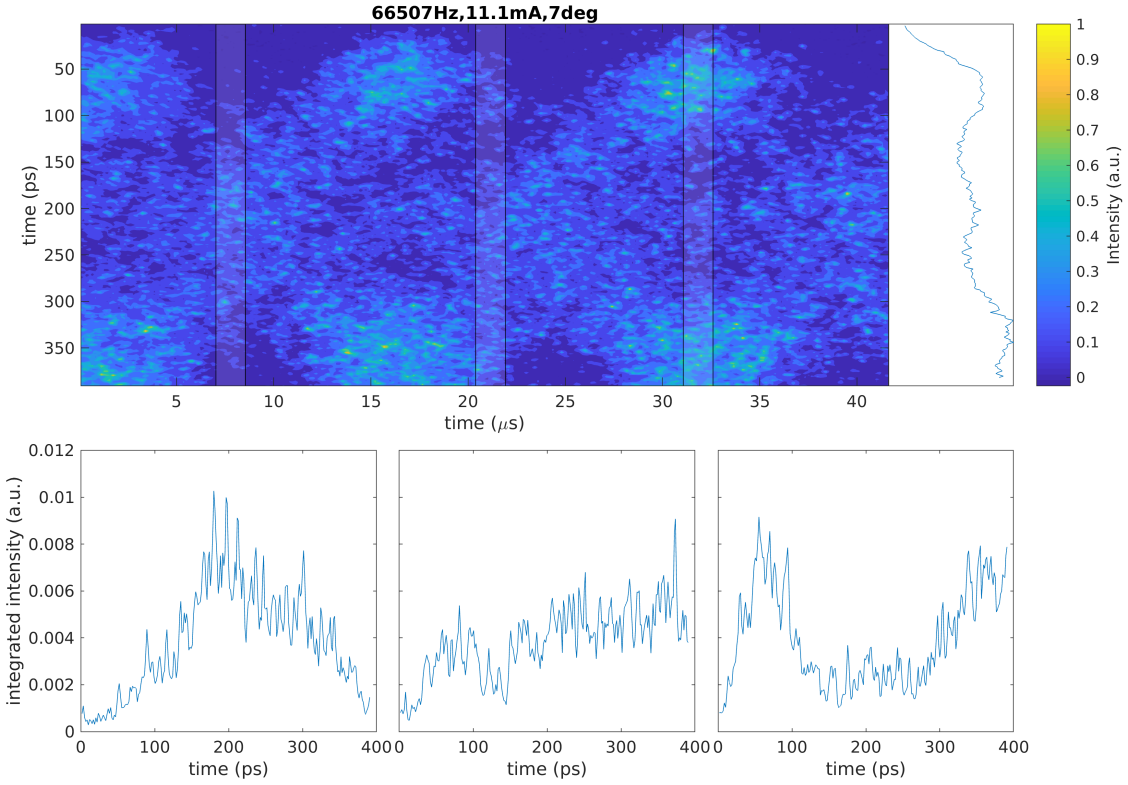

Figure B.6.: Off resonance +500 Hz PM excitation at (7°/11.1 mA)

list of abbreviations

AV	acceration voltage
BBB	Bunch-By-Bunch
BPM	beam position monitor
CCD	charge-coupled device
CoC	center of charge
CSR	coherent synchrotron radiation
CSS	Control System Studio
DBA	Double-Bend-Achromat
DCCT	Direct Current Current Transformer
E-Gun	electron gun
EMG	exponentially modified Gaussian
EPICS	Experimental Physics and Industrial Control System
FFT	fast Fourier transform
FGC	fast-gated intesified camera
FWHM	full width at half maximum
ISR	incoherent synchrotron radiation
KARA	Karlsruhe Research Accelerator
KIT	Karlsruhe Institute of Technology
Linac	linear accerator
LLRF	low-level RF
MA	momentum acceptance
MCP	micro channel plate
PM	phase modulation
PV	Process Variable
RF	radio frequency
RF-PM	radio frequency phase modulation
RMS	root mean square
SC	streak camera

SEM standard error of the mean

SR synchrotron radiation

TCSPC time-correlated single photo counting

VLDP visible light diagnostic port

Bibliography

[1] Cockcroft J.D. and Walton E.T. Experiments with high velocity positive ions. *Proceedings of the royal society of London. Series A, containing papers of a mathematical and physical character*, 129(811):477–489, 1930.

[2] Van De Graaff R.J., Compton K., and Van Atta L. The electrostatic production of high voltage for nuclear investigations. *Physical Review*, 43(3):149, 1933.

[3] Ising G. Prinzip einer methode zur herstellung von kanalstrahlen hoher voltzahl. *Ark. Mat. Astron. Fys.*, 18:1–4, 1924.

[4] Wideröe R. On a new principle for the attainment of high voltages. *Arch. Elektrotech*, 21:387, 1929.

[5] Lawrence E.O. and Livingston M.S. The production of high speed light ions without the use of high voltages. *Physical Review*, 40(1):19, 1932.

[6] McMillan E.M. The Synchrotron—A Proposed High Energy Particle Accelerator. *Phys. Rev.*, 68:143–144, Sep 1945. doi:10.1103/PhysRev.68.143.

[7] Lienard A. L'Eclairage elect. 16, 5, 53, 106 (1898); E. Wiechert. *Arch. Neerl*, 5:549, 1900.

[8] Elder F., et al. Radiation from electrons in a synchrotron. *Physical Review*, 71(11):829, 1947.

[9] Rowe E. and Mills F.E. Tantalus. 1. A Dedicated Storage Ring Synchrotron Radiation source. *Part. Accel.*, 4:211–227, 1973.

[10] Le Duff J. Current and current density limitations in existing electron storage rings. *Nuclear Instruments and Methods in Physics Research Section A: Accelerators, Spectrometers, Detectors and Associated Equipment*, 239(1):83–101, 1985.

[11] Touschek B.F. The Italian Storage Rings. *eConf*, C630610:171, 1963.

[12] Bernardini C., Touschek B., et al. Lifetime and Beam Size in a Storage Ring. *Phys. Rev. Lett.*, 10:407–409, May 1963. doi:10.1103/PhysRevLett.10.407.

[13] Sakanaka S., et al. Improvement in the beam lifetime by means of an rf phase modulation at the KEK Photon Factory storage ring. *Phys. Rev. ST Accel. Beams*, 3:050701, May 2000. doi:10.1103/PhysRevSTAB.3.050701.

[14] Sakanaka S. and Obina T. Observation of Longitudinal Quadrupole-mode Oscillations of a Bunch which were Induced by RF Phase Modulation in the Electron Storage Ring. *Japanese Journal of Applied Physics*, 40(Part 1, No. 4A):2465–2474, apr 2001. doi:10.1143/jjap.40.2465.

[15] Abreu N.P., Farias R.H.A., and Tavares P.F. Longitudinal dynamics with rf phase modulation in the Brazilian electron storage ring. *Phys. Rev. ST Accel. Beams*, 9:124401, Dec 2006. doi:10.1103/PhysRevSTAB.9.124401.

[16] Teytelman D. Phase modulation in storage-ring RF systems, 2019.

[17] Wiedemann H. *Particle Accelerator Physics*. Springer, 4th ed. 2015 edition, 2015. ISBN 978-331-91831-7-6.

[18] Wille K. *Physik der Teilchenbeschleuniger und Synchrotronstrahlungsquellen : eine Einführung*. Teubner-Studienbücher : Physik. Teubner, Stuttgart, 2., überarb. und erw. aufl. edition, 1996. ISBN 3-519-13087-4.

[19] Müller A.S. Accelerator Physics I: Particle Accelerators. Lectures at KIT, 2017.

[20] Liouville J. Note sur la Théorie de la Variation des constantes arbitraires. *Journal de mathématiques pures et appliquées*, pages 342–349, 1838.

[21] Schütze P. Transversale Strahldynamik bei der Erzeugung kohärenter Synchrotronstrahlung, 2018.

[22] Newton D. and Wolski A. Design of Electron Storage and Damping Rings Part 5: Coupling and Alignment. US Particle Accerator School, 2013.

[23] Jackson J.D. *Classical electrodynamics*. Wiley, New York [u.a.], 2. ed. edition, 1975. ISBN 047143132X. IMD-Felder maschinell generiert (GBV).

[24] Müller A.S. et al. Experimental Aspects of CSR in the ANKA Storage Ring. *In ICFA Beam Dynamics Newsletter No. 57*, pages 154–165, April 2012.

[25] Rosborg A. *Electron beam sizes and lifetimes at MAX II and MAX III*. Ph.D. thesis, Lund University, 2012.

[26] Streun A. Lattices for light sources. 2006. doi:10.5170/CERN-2006-002.217.

[27] Sands M. The Physics of Electron Storage Rings: An Introduction. *Conf. Proc.*, C6906161:257–411, 1969.

[28] Bruck H. *Circular particle accelerators*. 1974.

[29] Le Duff J. Single and multiple Touschek effects. In *Cas Cern Accelerator School*, pages 114–130. Cern, Berlin, Germany, September 1987.

[30] Bocchetta C.J. et al. Beam Density Manipulations in the Elettra storage ring. In *In Procceeding of Particle Acceleration Conference*, pages 829–831. 1997.

[31] Chao A.W. *Physics of collective beam instabilities in high-energy accelerators*. 1993. ISBN 9780471551843.

[32] Mochihashi A., et al. Longitudinal beam manipulation by RF phase modulation at the Karlsruhe Research Accelerator. In *IPAC WEPTS016*. 2019.

[33] Mathieu E. Mémoire sur le mouvement vibratoire d'une membrane de forme elliptique. *Journal de Mathématiques Pures et Appliquées*, 13:137–203, 1868.

[34] Mochihashi A., et al. Detuning Properties of RF phase modulation in KARA electron storage ring.

[35] Synchrotron-Radiation-facility. ANKA instrumentation book 2012. http://www.anka.kit.edu/downloads_anka/instrumentation_books//Instrumentationbook-2012.pdf. Online; accessed 2019-10-28.

[36] Dimtel. LLRF9 Controller. https://www.dimtel.com/products/llrf9. Online; accessed 2019-10-29.

[37] Teytelman D. iGp12-720F Signal Processor: Technical User Manual, June 2019.

[38] Kehrer B. *Time-resolved studies of the micro-bunching instability at KARA*. Ph.D. thesis, Karlsruher Institut für Technologie (KIT), 2019. doi:10.5445/IR/1000098584.

[39] Brosi M. *Untersuchung des Burstingverhaltens von Synchrotronstrahlung im THz-Bereich*. Master's thesis, Karlsruher Institut für Technologie (KIT), 2014.

[40] KIT-IBPT. construction department, 2015.

[41] Hiller N. *Electro-Optical Bunch Length Measurements at the ANKA Storage Ring*. Ph.D. thesis, Karlsruher Institut für Technologie (KIT), 2013.

[42] Max-Planck-Gesellschaft. The fastest stopwatch in the world. https://www.mpg.de/495195/pressRelease200402241, 2004. Online; accessed 25-Februrary-2020.

[43] Schönfeldt P. *Simulation and measurement of the dynamics of ultra-short electron bunch profiles for the generation of coherent THz radiation*. Ph.D. thesis, Karlsruher Institut für Technologie (KIT), 2018. doi:10.5445/IR/1000084466. 54.01.01; LK 01.

[44] Hamamatsu Photonics Deutschland GmbH. *High Performace Digital Tempral Analyzer (HPD-TA) user manual*.

[45] Forck P. Lecture Nores on Beam Instrumentation and Diagnostics. Joint University Accelerator School, 2016.